# 3D Printing of Light Trapping Structures for Dye-Sensitised Solar Cells

Andrew N. Knott, MSc.

*Thesis submitted to The University of Nottingham for the Degree of Doctor of Philosophy*

2017

# Abstract

Converting solar energy directly into electricity as a clean and renewable energy resource is immensely important to solve the energy crisis and environmental pollution problems induced by the consumption of fossil fuels. Dye-sensitised solar cells have attracted a great deal of attention following their development in 1991. They provide a technically and economically credible alternative that could challenge the dominance of conventional p-n junction photovoltaic devices in the solar energy market.

3D printing and other additive manufacturing techniques allow the fabrication of geometrically complex end-use products and components in a variety of materials by using technologies that deposit material layer-by-layer. The additive manufacturing of optoelectronic devices is still in its infancy but has the potential to completely revolutionise the industry. Two-photon polymerisation is a technique used to fabricate 3D structures with resolutions down to a few hundred nanometres. The technique shows the ability to fabricate highly complex 3D structures of arbitrary shape with unprecedented levels of control.

In this thesis the two-photon polymerisation 3D printing technique is used to fabricate $TiO_2$ thin films of optimised 3D micro-design for use in DSSCs. Our 3D printed films have a considerable advantage over the conventional (random assembly) films, as they allow the implementation of optimised light trapping designs directly into the cell. Cells are characterised with scanning photocurrent microscopy with results showing these light trapping structures are able to improve photocurrent generation by up to $\sim 9\%$ when compared to conventional random assembly $TiO_2$.

# Acknowledgements

First, I would like to express my gratitude to my supervisors Oleg Makarovskiy, James O'Shea, Chris Tuck and Yupeng Wu. Their time, expertise, support and encouragement were essential throughout the course of my PhD. My thanks also go the technical staff in both the physics department and the additive manufacturing group, especially to Mark East who is always willing to help, no matter how busy he seems to be.

I would also like to mention Amalia Patané and Lyudmila Turyanska who, as supervisors of my MSc project in the year preceding my PhD, were invaluable with their academic support but also with their personal support and encouragement in helping me to overcoming some health issues, which at times made it a challenging year.

My special thanks to all the colleagues I have worked with in both the physics and engineering departments for their friendship, advice, assistance with experiments and for helping to provide a fruitful and enjoyable three years of my life.

I would also like to thank my partner Daisy and my family and friends for their personal support and encouragement throughout this project.

# List of Publications

1. *Scanning photocurrent microscopy of 3D printed light trapping structures in dye-sensitized solar cells*, A. N. Knott, O. Makarovskiy, J. O'Shea, Y. Wu and C. Tuck, Solar Energy Materials and Solar Cells, Accepted - awaiting publication, (2018)
2. *3D printing of light trapping structures for dye sensitized solar cells*, A. N. Knott, O. Makarovskiy, J. O'Shea, Y. Wu and C. Tuck, UK Semiconductors, Poster Presentation (2016)
3. *Layer by layer fabrication of sub-micron light trapping structures for dye-sensitized solar cells*, A. N. Knott, O. Makarovskiy, J. O'Shea, Y. Wu and C. Tuck, 44th "Jaszowiec" 2015 International School & Conference on the physics of semiconductors, Presentation (2015)

# Contents

## 5 Research Methodologies 59

# List of Figures

# Abbreviations

**DSSC** Dye sensitised solar cell

**TPP** Two-photon polymerisation

**SPCM** Scanning photocurrent microscopy

**SEM** Scanning electron microscopy

**EDX** Energy dispersive X-ray spectroscopy

**UV** Ultra-violet

**TCO** Transparent conducting oxide

**HOMO** Highest occupied molecular orbital

**LUMO** Lowest unoccupied molecular orbital

**CB** Conduction band

**FTO** Fluorine doped tin oxide

**ITO** Indium doped tin oxide

**QDSC** Quantum dot solar cell

**STM** Scanning tunnelling microscopy

**AFM** Atomic force microscopy

**TPA** Two-photon absorption

**NIR** Near infra-red

**MAPD** Maximum achievable photocurrent density

**IPCE** Incident photon to current conversion efficiency

**SE** Standard error of the mean

**CI** Confidence interval

**PGMEA** Propylene glycol monomethyl ether acetate

**IPA** Isopropanol

# Chapter 1

# Introduction

The need for renewable energy sources is rising due the increased strain that the use of fossil fuels is placing on the planet. Solar energy has long been seen as the one of the renewable energy sources with the greatest potential to challenge fossil fuel's dominance over the energy market. Renewables are now the fastest growing energy sector with solar energy making one of the biggest contributions to this growth rate. P-n junction solar cells have long been the most attractive solar cell technology due to their high efficiencies, however there are a number of alternative solar cell technologies in which interest is growing. One of these technologies is the dye-sensitised solar cell (DSSC) which has great appeal due to its competitive performance, low material and fabrication costs and increased flexibility (such as being able to create semi-transparent cells for energy generating windows). Because of this technology's potential much research effort has been placed on improving this type of cell's efficiency, which is currently lower than conventional Si p-n junction solar cells. One way this can be done is by increasing light trapping in the cell, leading to greater absorption and consequently to higher efficiencies. This work will present a novel fabrication method, using the micron/sub-micron 3D printing technique two-photon polymerisation (TPP), for producing light trapping structures in DSSC. These structures are characterised using a scanning photocurrent microscopy technique (SPCM) which is able to show significantly increased photocurrent generation when compared to planar devices.

## Aims, objectives and scope of research

The aim of this work is to develop a method for the fabrication of a variety of structures which can increase the light trapping properties of solar cells, thereby increasing the amount of incident solar radiation absorbed and enhancing photocurrent generation and the overall efficiency of the cell. With the specific aim of the fabrication of these structures for implementation into DSSCs, a novel third generation device, which has significantly lower efficiencies than conventional photovoltaics and could benefit greatly from enhanced performance.

This will be achieved via the use of the two-photon polymerisation technique for the microfabrication of polymer stamps or templates. These are then used to pattern the light trapping structures into a planar $TiO_2$ nanoparticle thin film, which is used as the active layer of the cell. The development of this method and its optimisation will be charted and quality assured by characterisation with optical and scanning electron microscopy (SEM), alongside elemental analysis with energy-dispersive X-ray spectroscopy (EDX). Once a reliable method has been devised for the fabrication of reproducible devices of good quality the effectiveness of their performance enhancing effects is evaluated using a SPCM technique. This allows us to produce maps whereby the improvement in photocurrent generation from our light trapping structures can be seen over areas of planar $TiO_2$.

The scope of the review of the literature will encompass device architecture mechanisms of both conventional photovoltaics and DSSCs, it will also cover the current state of light trapping research across the whole field of photovoltaics, with a focus on the DSSC. This is important because many of the ideas or methods for the introduction of light trapping structures into conventional photovoltaics are also applicable when looking at DSSCs, much as how this work, while only studying the DSSC, could have implications across the wider field. In this pilot study, whilst many polymer structures are fabricated using TPP, further experimental work is limited to the study of only micro-pyramid arrays patterned into $TiO_2$ electrodes, since much of the work here was spent developing the method for structure fabrication and implementation. With the ground work for structure fabrication laid TPP allows for the fabrication of structures of almost arbitrary geometry, allowing the best light trapping designs to be realised and tested in future work.

### Structure of thesis

This work will first explore in detail the operating principles and architecture of DSSCs. It will give context to the thesis by showing both how this technology can fit into a future global energy infrastructure and areas of its performance/manufacture which must be changed or improved before it can do this. Light trapping in photovoltaics will be reviewed to give the reader a general understanding of the current state of the research in this area. Focusing on how light trapping structures have been realised in DSSCs and how these structures affect the overall performance of the cell. Background into the micro-fabrication technique TPP will follow, with a complete overview of the physical mechanisms in this process given and a detailed look at some of the novel applications this technology has been put to.

Next the research methodologies used during this work will be covered, ranging from the characterisation techniques used to analyse the fabrication process and the final light trapping solar cells to cell design and the fabrication process. Results will follow where the SPCM technique is predominately used to investigate the enhancement of photocurrent generation in the cells due to the implementation of light trapping structures. Future discussion of these results, future work which could be conducted to continue this research and the main conclusions that can be drawn from this work will finally be presented to complete the thesis.

# Chapter 2

# Dye-Sensitised Solar Cells

## 2.1 Introduction

Solar energy can be collected as both thermal and electrical energy, using solar thermal collectors and photovoltaics, respectively [1]. Photovoltaics is the name given to systems which exploit the photoelectric effect, whereby photons are converted to electrical current via the excitation of electrons into higher energy states allowing them to act as charge carriers. Traditionally photovoltaic devices are based on the concept of electron-hole separation in the high electric field region of a p-n junction at the interface of two semiconductor materials [2]. The field of photovoltaics has been largely dominated by inorganic solid-state junction devices, usually made from silicon [3]. This dominance is however being challenged by a new generation of devices based on nanocrystalline semiconductor films, organics and organic-inorganic perovskite materials [4]. Dye-sensitised solar cells (DSSCs) are devices based on nanocrystalline thin films of wide band-gap semiconductors such as $TiO_2$, sensitised with organic dye molecules which capture photons. DSSCs provide a technically and economically credible alternative to traditional silicon p-n junction solar cells due to their low material cost and easy and inexpensive fabrication methods [5]. However some challenges face the development of the DSSCs, with the improvement of overall cell efficiency being essential to the future success of the technology. This work will look to address this issue with a study of the fabrication, implementation and characterisation of 3D printed light trapping structures into the cell to increase efficiencies.

This chapter will give context to the work by conveying an overview of the current need for renewable energies to replace fossil fuels, before describing traditional photovoltaics and where they fit in this context. The rest of this chapter will then describe in detail the DSSC, its advantages, device architecture and operating principles before finally taking a look at the future prospects for DSSCs and similar devices.

## 2.2 Energy context and renewable energy

Technological advancements in the modern age have led to increased reliance on and consumption of energy. With population increases and the continued economic growth of developing nations these energy demands are only set to increase, with recent estimates suggesting that worldwide energy consumption may grow by up to 48% by 2040 [6]. The current and historical domination of the energy market by fossil fuels cannot continue since they come from limited stock and their combustion creates significant environmental problems. With worldwide governments increasingly committed to tackling climate change and attempting to limit global temperature increase to below 2°C the desire to find fossil fuel alternatives reaches new heights. More efficient and environmentally friendly methods for extracting and consuming fossil fuels, along with cleaner fossil fuels like natural gas can help bridge the gap to an economically viable renewable alternative. Nuclear fission can likewise help this transition, however this also comes with some environmental concerns. Disasters, such as at Fukushima, have eroded public trust in the technology, promoting governments worldwide to shy away from investing in building new nuclear reactors. We can see from figure 2.1, the worldwide domination of non-renewable energies, but also the growing share that renewables have. With photovoltaics showing the largest increase of all these new renewable energy sources.

It is clear that a commercially viable and sustainable energy conversion process needs to be discovered and developed. There are many possible renewable energy technologies which have potential to become the dominant force in the energy market, including solar energy, wind turbines, hydroelectric and geothermal. However more likely is that the future global energy infrastructure will include a complex mix of all these technologies complementing each other. The Sun alone is one

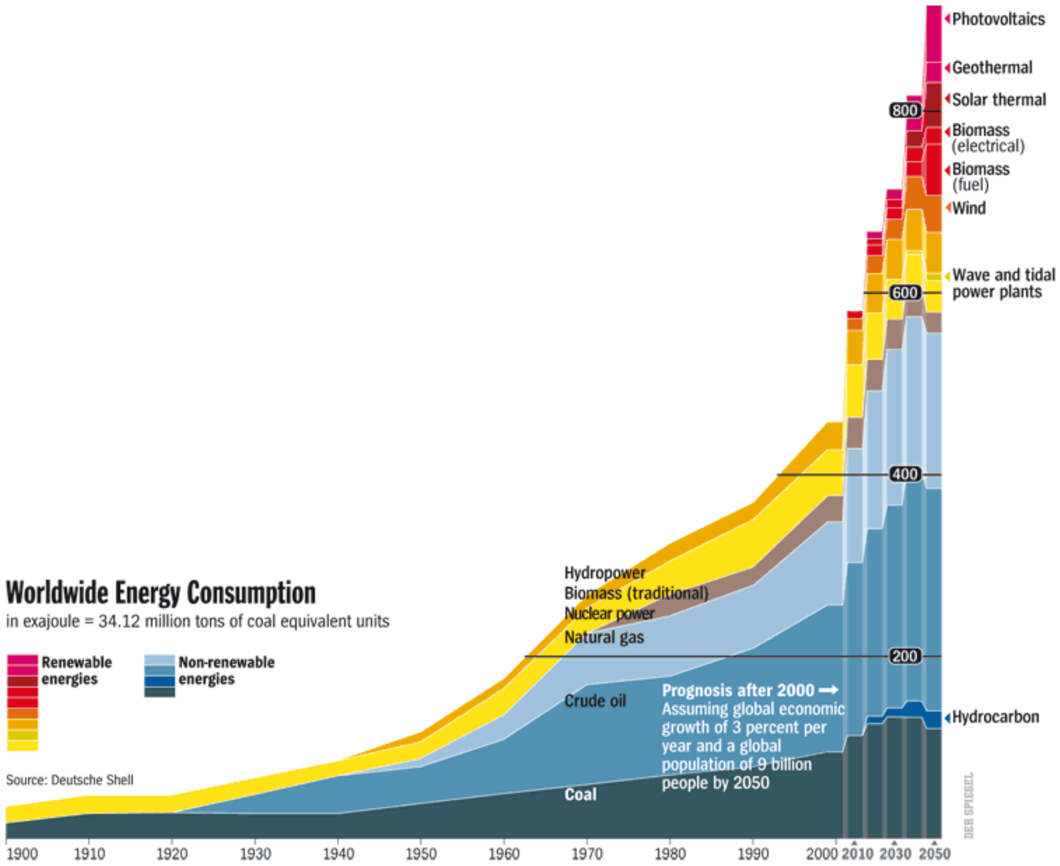

Figure 2.1: Worldwide Energy Consumption [7].

source that could supply the world's energy demands in a sustainable fashion; in fact the amount of solar energy reaching our planet in one day is enough to account for an entire year of humanity's energy usage [8].

## 2.3 Photovoltaics

All photovoltaic devices are based on the concept of charge separation at the interface of two materials, traditionally this is done at the interface of two doped semiconductors with band gap matching required photon energy. Doping refers to the intentional introduction of impurities into the semiconductor materials. Donor dopants have more valence electrons than the intrinsic semiconductor they are introduced to, giving an excess of electrons to the system. These electrons are free to move in the crystal lattice, this is known as an extrinsic n-type semiconductor.

Acceptor dopants have fewer valence electrons than the intrinsic semiconductor, this gives a deficiency of electrons, these positive charge regions are known as a holes, and are also free to move in the crystal lattice, this is known as an extrinsic p-type semiconductor. When a p-type and an n-type semiconductor come into contact a p-n junction is formed, here charge carriers diffuse across the interface, with diffused electrons combining with holes in the p- region and diffused holes combining with electrons in the n- region. This leads to a build up of charge on both sides and an internal built-in electric field across the junction known as a depletion region, as seen in figure 2.2. This electric field opposes the diffusion of carriers at the interface and equilibrium is reached. In a solar cell p- and n-type regions are connected in a circuit, photons incident at the junction excite electrons creating electron-hole pairs. These photogenerated carriers are then pulled by the electric field towards the contacts creating an electrical current in the device. The photogeneration and separation of charge carriers at the p-n junction in a solar cell can be seen in the band diagram in figure 2.2.

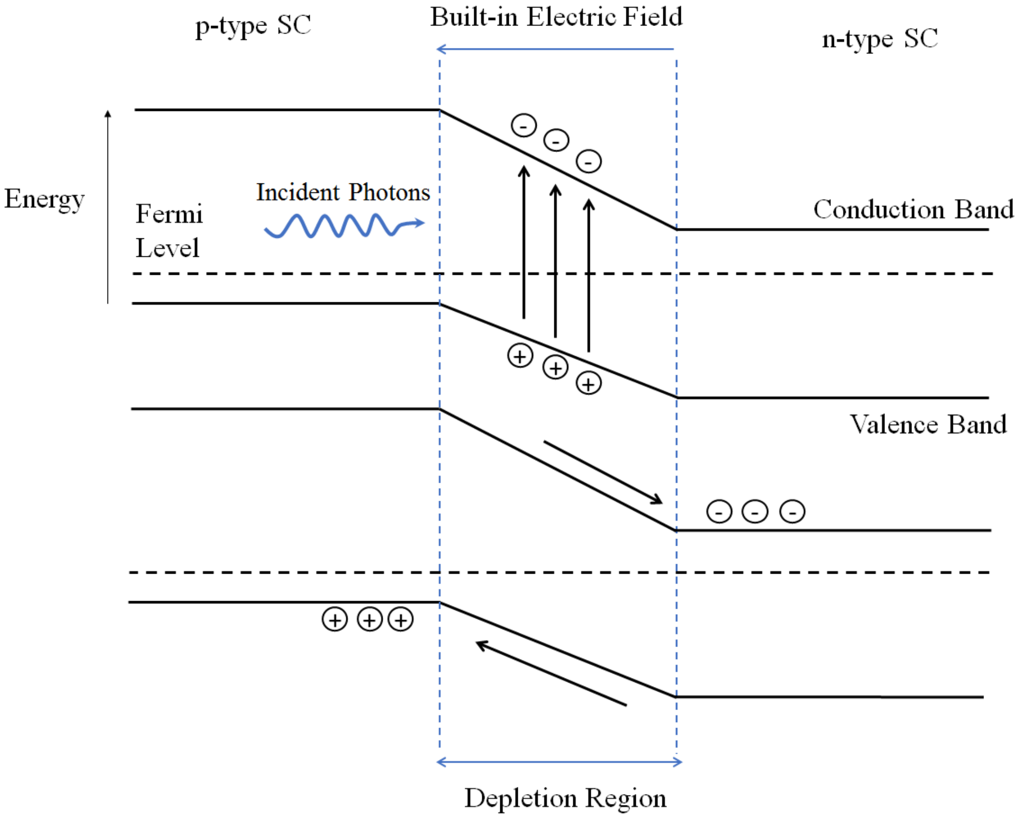

Figure 2.2: Semiconductor p-n junction in a solar cell showing photogenerated carriers.

P-n junction solar cells are limited by the Shockley-Queisser limit which states the maximum cell efficiency to be approximately 33.7% due to losses from processes such as recombination and the limited wavelengths of light that the semiconductor can absorb [9]. Best performing lab based single p-n junction Si cell efficiencies have reached as high as 27% with more common and less expensive methods producing Si cells being slightly lower at around 25% [10]. The history of the improvement in efficiencies can be seen in blue in figure 2.3. These limits can be overcome with the introduction of multi-junction cells, utilising two or more p-n junctions with different semiconductor materials which will absorb a different spectrum of light. Multi-junction cells have reached efficiencies as high as 46% [11]. However, these cells have a much higher cost than others in the market and are generally only used when their high cost becomes practical, and as such are preferred on spacecraft where the power to weight ratio is of great importance. Multi-junction solar cells can be seen represented in purple in figure 2.3. Alternative solar cell technologies include thin film solar cells which can challenge the dominance of the market by conventional Si PV technologies because of their lower materials and fabrication cost and their flexibility [12]. Interest in thin film solar cells has been around from the beginnings of solar cell research and these cells have seen excellent improvements in efficiencies over the years. However, they are currently still outperformed by crystalline Si solar cells. Their development history can been seen in green in figure 2.3. Newer emerging solar cell technologies have attracted a lot of attention since the development of DSSCs in the early 90's. These cells (and their derivatives such as perovskite and quantum dot solar cells) and other emerging technologies such as organic solar cells have also shown marked improvement in efficiencies over the years. However, they need to be improved further still to compete with more traditional solar cell technologies. The historical improvement of these cells are seen in red in figure 2.3.

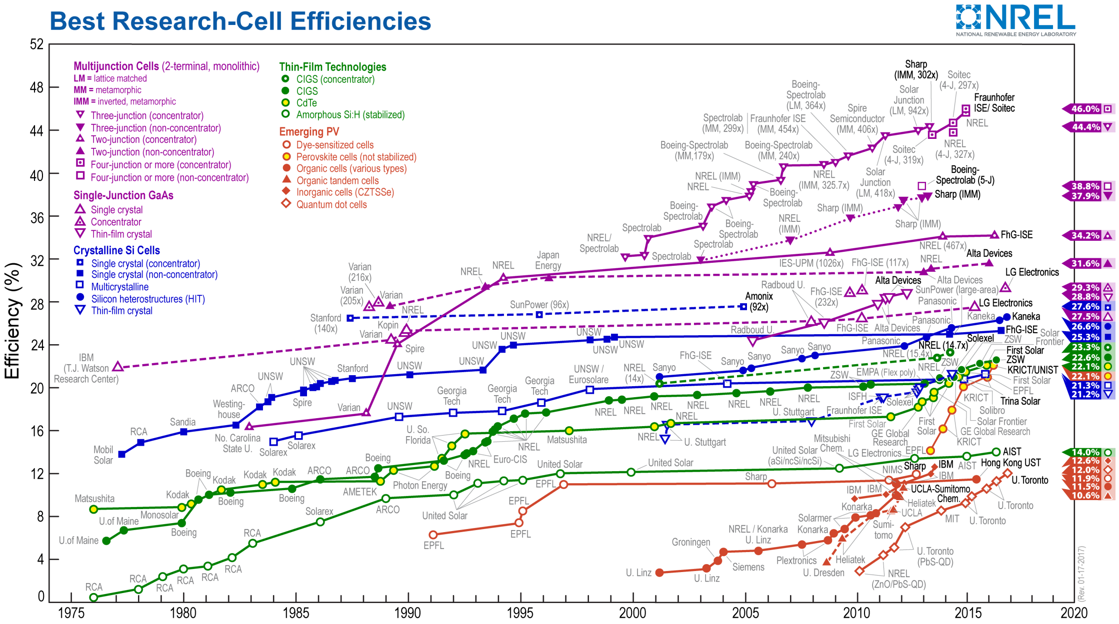

Figure 2.3: History of the power-conversion efficiency of Photovoltaic cells. Adapted from reference [13].

Solar energy enjoys only a 1.1% share of the total global energy market in 2017, however it is undergoing rapid growth and has more than doubled in the last two years [14]. One barrier that would see this share increase even more quickly is cost, which is why there is a great interest in lower cost emerging solar technologies, such as DSSCs, which now be will explored in more detail.

## 2.4 The dye-sensitised solar cell

DSSCs are a novel type of solar cell that use dye molecules adsorbed at the surface of nanocrystalline oxide semiconductors such as $TiO_2$ to collect sunlight. They have attracted a great deal of attention following their development in 1991 by Grätzel and O′Regan [15]. $TiO_2$ is a wide band-gap semiconductor and is white in appearance due to its reflection of visible light from the solar spectrum. $TiO_2$ does absorb ultraviolet light, but as can be seen in the solar spectrum in figure 2.4 UV light is only a small part of the light reaching the earth's surface. To enable this material to absorb more light at longer wavelengths it needs to be sensitised with dye molecules. In a DSSC these dye molecules are adsorbed onto the surface of $TiO_2$ nanoparticles, where they absorb light from the visible part of the solar spectrum exciting electrons in the molecule to higher energy states, where they are in turn injected into the $TiO_2$.

Although not as efficient as Si p-n junction solar cells DSSCs provide a technically and economically credible alternative, due to their low material cost, easy and inexpensive fabrication methods [5]. There are, however, many challenges facing the development of DSSCs, such as the improvement of cell life time, since solar panels need to remain effective in outdoor conditions for sustained periods. Also, and most importantly the overall efficiency of DSSCs needs to improve before it can seriously challenge the more traditional silicon solar cells [16]. The growing interest in this technology can be seen by the increase in relevant publications between 1990 and 2009 seen in figure 2.5.

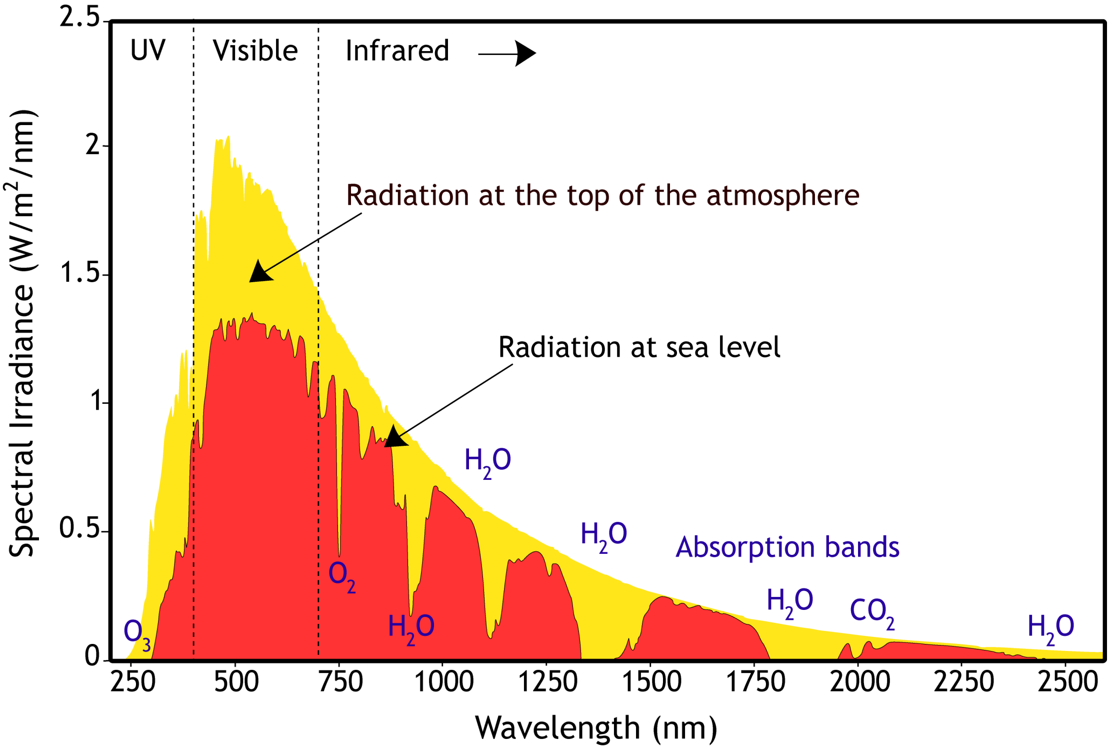

Figure 2.4: Solar spectrum at top of the earth's atmosphere and at sea level. Adapted from [17].

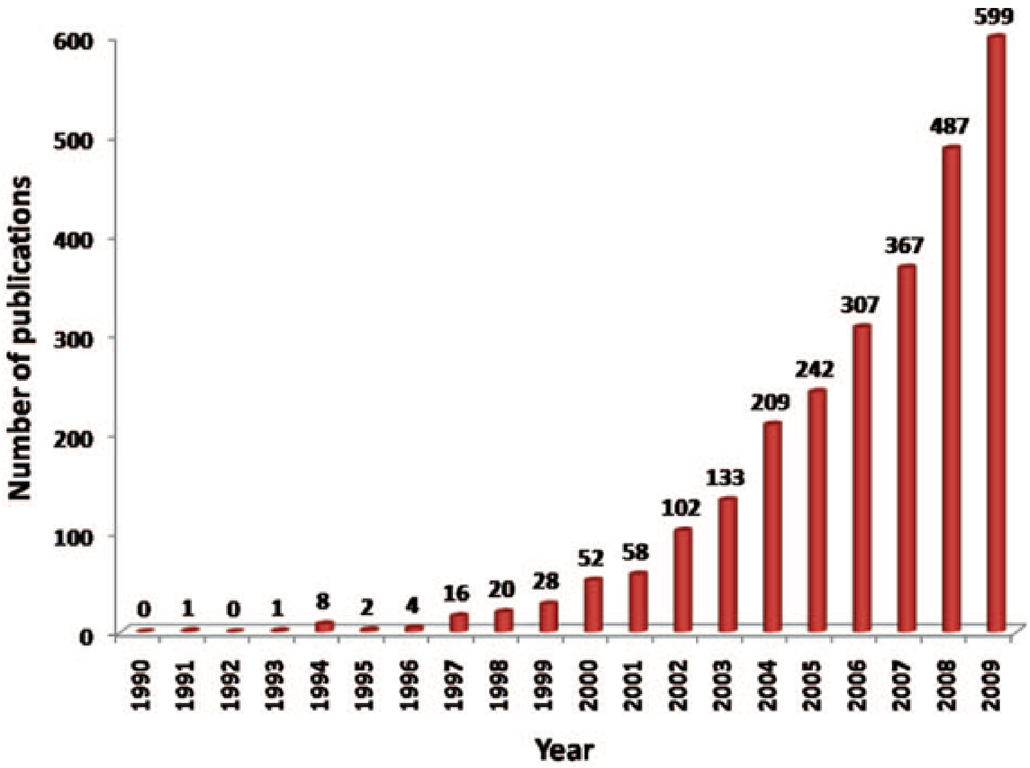

Figure 2.5: Number of papers published with DSSC in title or as keyword [18].

### 2.4.1 Device architecture and operating principles

A typical DSSC cell comprises of a transparent conducting oxide (TCO) electrode, a mesoporous nanocrystalline oxide semiconductor charge transport layer, dye molecules which absorb photons, a redox electrolyte (typically iodide tri-iodide) to regenerate oxidised dye molecules, and a transparent conducting counter electrode with a thin platinum layer which acts as a catalyst for the redox reaction. Figure 2.6 shows the components and configuration of a typical DSSC.

Molecular orbitals for large molecules such as the dyes used here, are incredibly complicated. However, we only deal with molecular orbitals related to the lowest electronic transitions that are possible is this system. These are known as the highest occupied molecular orbital (HOMO) and the lowest unoccupied molecular orbital (LUMO). The HOMO is the highest energy molecular orbital which are occupied with electrons when the molecule is in this lowest energy state i.e. when the system has not been given energy. The LUMO is the next highest energy state, that is the lowest energy state which an excited electron can transition to. The

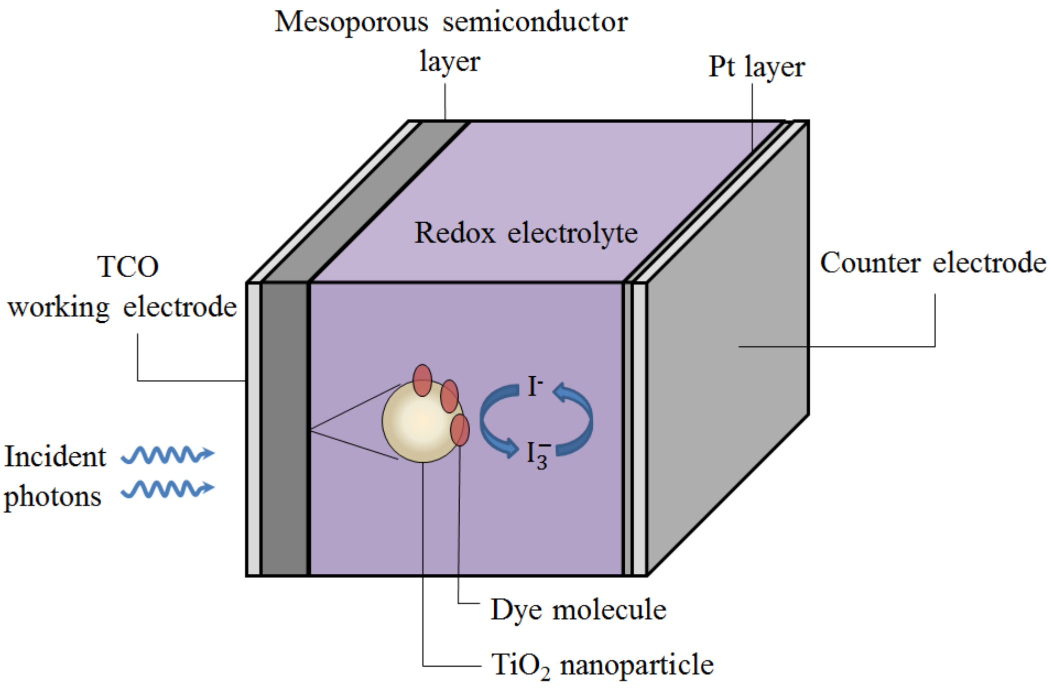

Figure 2.6: Schematic diagram of components and configuration of a DSSC.

difference between the two is known as the HOMO-LUMO gap and is the lowest electronic excitation which can occur in the system. The HOMO and LUMO can be thought of as analogous to the valence and conduction bands of crystalline semiconductors. However since these bands consist of a multitude of levels as opposed to the discrete energy levels of the HOMO and LUMO some properties present in these system cannot be understood by thinking in this manner. Figure 2.7 shows the electronic processes, shown by the solid back lines, in a DSSC:

1. Photon is absorbed by the dye molecule, and excites an electron in the dye from HOMO to LUMO.
2. The electron is injected into the conduction band (CB) of the SC charge transport layer.
3. The electron is transported through this thin film by diffusion to the electrode.
4. Work is done on an external load.
5. Reduction of electron acceptors in the electrolyte ($I_3$) at the TCO/Pt counter electrode.

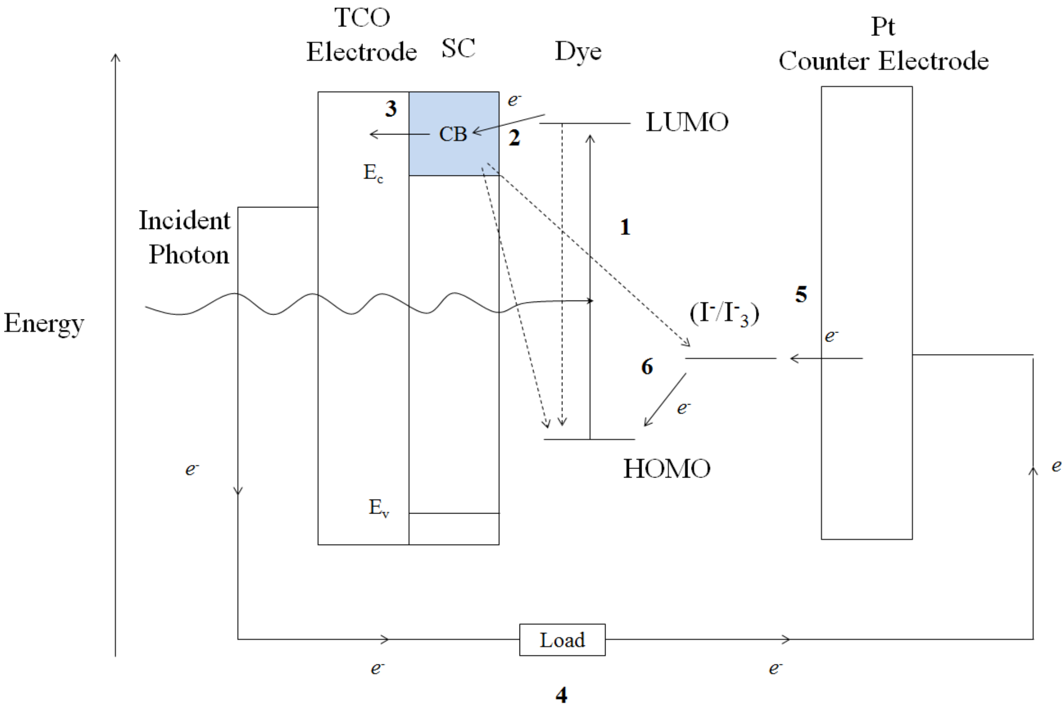

Figure 2.7: Diagram showing electronic processes in a DSSC.

6. Oxidized dye is regenerated by the electron donor ($I^-$).

The dashed lines in figure 2.7 represent unfavourable processes in a DSSC. These include recombination in the dye molecule, recombination from the conduction band of the semiconductor with holes in the HOMO of the dye and recombination from the conduction band of the semiconductor with acceptors in the electrolyte.

### Dye

Each component of the DSSC has specific requirements which need to be met for the cell to perform effectively. First the incident photon is absorbed by the dye, which must have an absorption spectrum which has good absorption of light in part of the solar spectrum which reaches the earth's surface. Excited electronic states in the dye must be above the conduction band in the semiconductor charge transport layer to allow for successful injection of electrons. The LUMO is usually located close to the semiconductor interface, this helps the molecules' stability as excited electrons can cause damage. Conversely the HOMO is best located

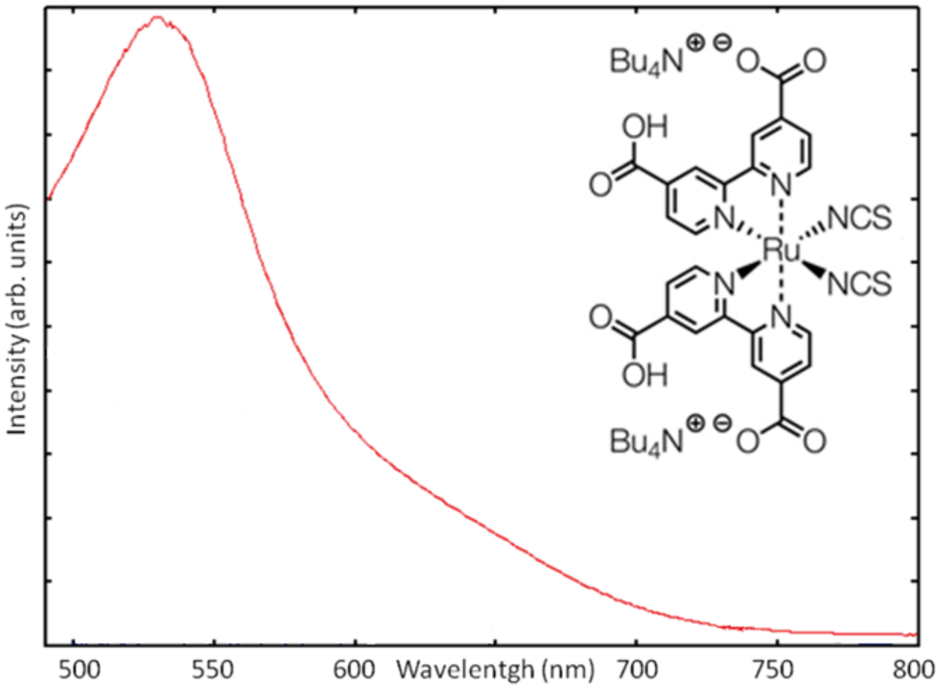

Figure 2.8: Absorption spectra of N719. Insert shows chemical structure of N719. Adapted from reference [21].

far from the interface where it can be easily regenerated by the electrolyte. For the cell to work effectively over a long lifetime the dye molecule must be able to sustain many repeated oxidisation and reduction cycles. Good anchoring to semiconductor surface is also an important requirement for the long term stability of the cell.

Because of these many requirements great efforts have been made in researching and synthesising molecules with optimal geometries as they can greatly affect the performance of the cell [19]. One popular dye which meets these requirements well is the dye known as N719 or N353. This dye has been used in some of the best performing standard DSSCs [20] as it meets many of these specific requirements. Figure 2.8 shows the molecular structure of the dye and the absorption spectrum. This dye is used predominantly in the experimental work presented in this thesis. There are many other dyes and types of dye which can be used as sensitisers in DSSCs. Some of these different dye types, along with some advantages and there efficiencies ranges, can be seen in table 2.1.

| Dye Type | Advantages | Efficiency range |
|---|---|---|
| Ru-complexes | High efficiencies | 7-14% |
| Metal-free organics | Cost | 5-10% |
| Quantum-dots | Tunable absorption | 4-7% |
| Perovskite-based | Low cost | 4-10% |
| Natural | Very low cost | 0.3-1.2% |

Table 2.1: Table showing various sensitiser and dye types. Adapted from [22]

### Semiconductor charge transport layer

The semiconductor charge transport layer also has some very specific requirements. This layer must provide a large surface area for greater dye adsorption, dyes adsorbed onto the surface of a flat semiconductor layer will absorb only a few % of incident light leading to poor performing cell [23]. The electrolyte needs to be able to penetrate into the pores of the semiconductor layer to regenerate oxidised dye molecules and complete the device's circuit. And of course a reasonably high conductivity must be maintained for good cell performance. The best way to meet all of these requirements is to use a network of randomly assembled interconnected nanoparticles, which contain mesoporous channels. DSSCs commonly use thin films of sintered $TiO_2$ nanoparticles for the semiconductor layer [24], with ZnO and NiO also being widely used in research. $TiO_2$ nanoparticles have the property of welding together during the sintering process making a network of well connected particles which is important for increased conductivity [24]. The optimal thickness of this layer for optical absorption, electronic transport and regeneration of the dye is approximately $10 - 15\mu m$ [25].

### Electrodes

Incident photons must pass through the electrode to reach the dye molecules, as shown in figure 2.6 and 2.7, therefore this electrode must be transparent and absorb as little light as possible. To achieve this transparent conducting oxide thin films such as fluorine doped tin oxide (FTO) and indium doped tin oxide (ITO) are coated onto glass or flexible transparent plastic substrates. The counter electrode is responsible for the reduction of the electrolyte solution so that it can regenerate the dye molecules, to help facilitate this reaction a catalyst such as Pt is coated onto a TCO.

**Electrolyte**

The electrolyte has the function of acting as a redox agent, with a reduction reaction occurring at the counter electrode to carry electrons and then an oxidation reaction occurring at the dye molecule. This reaction gives the required electron to the dye molecule to return it back to its ground state after the excited electron is injected into the semiconductor layer. Via this redox reaction depleted dye molecules are continually regenerated with electrons allowing the cycle to continue. Typically a liquid electrolyte such as iodide/triiodide is used in high performance DSSCs, although using a liquid can be problematic as leakages can lead to long term stability issues. The redox reactions for the iodide/triiodide redox couple are seen below with the oxidation reaction at the dye shown in equation 1.1 and the reduction reaction the counter electrode shown equation in 1.2.

$$I^{-} \longleftarrow e + I_{3^{-}} \tag{2.1}$$

$$I_{3^{-}} + e \longrightarrow I^{-} \tag{2.2}$$

## 2.5 Dye-sensitised solar cell research

DSSCs have several important advantages over conventional Si pn-junction solar cells. However as previously mentioned there are a number of areas that need to be improved upon before they can seriously challenge the conventional cells dominance over the energy market. DSSCs can find some niche areas in the energy market where their special properties can be exploited for commercial energy production. The ability to be fabricated onto flexible substrates allows for their use in places which would be impossible for tradition solar cell modules. Low-cost high volume production can also be attained via roll-to-roll manufacturing methods [26]. Another interesting property is their transparency, which could allow for their use as windows, creating a new level of solar cell building integration [27]. They have also shown to, unlike Si solar cells, have very little change in efficiencies at high temperature in hot sunny conditions [28]. The DSSC performance is also less dependent on the light's angle of incidence than Si solar cells [29] making their low-light performance much better. All of these factors make the DSSCs available to be used in places which would not be practical or cost effective for Si solar cells.

Improving cell stability, further reducing material cost and raising efficiency are the most important advancements that have to be made before their commercial use becomes widespread. The main contributing factor to cell stability is the liquid electrolyte, these electrolytes can degrade the sealant in the cells over time leading to leakage and cell break down [30]. Leakages can be mitigated with the careful selection of electrolyte materials [31] and cell sealant [32]. Both must be thermally stable over a wide range of temperatures and under differing environmental conditions, since solar cells are outside all year in many different regions. The sealant must also be resistant to chemical reactions with the selected electrolyte.

With most of the materials being of low cost ($TiO_2$) or of comparable or equal cost to conventional Si solar cells (transparent conducting oxide glass) the focus for further reducing the material cost of DSSCs goes to the dyes and catalyst at the counter electrode. Whist ruthenium based dyes have shown to be very effective in DSSCs, it is a precious metal which is a rare and limited resource, adding greatly to the material cost. Because of this a lot of efforts are being made to develop alternative dyes such as metal free, organic [33] and porphyrin dyes [34], which are now showing performances which are becoming competitive with ruthenium based dyes. Since platinum is of course also a rare and expensive metal a lot of work has been put into finding a suitable alternative. Even though only a small amount of Pt is needed in DSSC fabrication, when this is scaled up to a commercial scale the cost becomes significant. Many different candidates are under scrutiny as this is another crucial bottleneck which needs to be broken before the widespread commercial application of DSSCs. Materials here include different metals, conducting polymers, metal-organic hybrids and other carbon materials such as graphene or carbon nanotubes [35].

Perhaps the most obvious and important improvement that can be made is raising the efficiency of the cell. The current lab record for DSSCs stands at 14% [36] compared to 25% for monocrystalline silicon solar cells [37], highlighting the need for improvement. Every component of the cell contributes to the overall efficiency so improving it is a complex and difficult process. When developing dyes, electrolyte, charge transfer layer semiconductors and electrode materials efficiency must always be kept in mind as it is one of the most important considerations. This work will focus on improving the efficiency by looking at the semiconductor charge transport layer, specifically by looking to improve light trapping and thus light absorption in this layer. Increased light trapping is an issue which is not just important in DSSCs but across the fields of photovoltaics and solar thermal collectors. In the next chapter light trapping will be explored in greater detail, first in photovoltaics in generally before looking more closely at DSSCs.

With these improvements being made to the DSSC it is attractive as a potential cost effective alternative to the more expensive Si photovoltaics, however their dominance is not yet challenged and more improvements will be required before this is the case. Despite this, commercial interest in the technology is growing with companies such as GCell in Newport, South Wales being the leader in large-scale mass production DSSCs. And are capable of the production of 500,000m$^2$ of DSSC modules per year using a roll-to-roll manufacturing technique.

DSSCs research has spawned new and exciting areas in photovoltaics with the fabrication of quantum dot solar cells (QDSCs) and perovskite solar cells. Both of which have the advantage of being solid state cells, where a liquid electrolyte is not required. Quantum dots are semiconductor nanoparticles, such as PbS, Cd or CdSe [38, 39], which can be used to collect light in place of the dyes in DSSCs. The first QDSCs only recorded efficiencies a few % [40, 41] but have since shown some significant improvements [42]. Perovskite is an organic-inorganic compound with a high absorption co-efficient which can be used as the active light harvesting layer. Perovskite solar cells were first reported in 2009 with efficiencies of 3.1 % [43]. However their performance quickly grew and surpassed that of DSSCs with efficiencies today reaching as high as 21 % [44]. Unfortunately perovskite cells have significant instability issues, whereby cell stability is affected by moisture, oxygen, heat and even incident photons [45]. Their cost can also be high due to the use of precious metals as electrodes, and the heavy encapsulation of the cell required to prevent exposure to environmental conditions which can seriously deteriorate cell performance [46]. Toxicity is another problem since the perovskite contains Pb which can escape into the environment if the constituent materials break down in the cell [47]. These issues need to be addressed before perovskite cells could be seriously considered as a viable commercial product.

It is important to note that light trapping is still an effective and important way to improve the efficiency of these DSSC derivatives, and as such the work presented in this thesis is also relevant to these new and exciting photovoltaic technologies. In fact light trapping is an important factor across the whole field on photovoltaics, and as such the technique of utilising 3D printing for the fabrication of these structures has the potential for a much broader impact in photovoltaics than just the DSSC which this research is focused on.

## 2.6 Summary and conclusions

This chapter gives the reader a general introduction and background into photovoltaics, and gives context to why this technology and its development are important in helping to meet the rising demand in energy usage in a sustainable fashion.

It moves on to introduce DSSC technology, starting with a description of the device architecture, operating principles and the physical mechanisms involved, including the electronic processes. A detailed look all the major components such as the light absorbing dyes, semiconductor charge transport layer, the working and counter electrodes and their differences, and the electrolyte for dye regeneration follows. The current state of research in the field of DSSCs is explored where aspects such as the technologies advantages over conventional photovoltaics (as well as their disadvantages), and important improvements which can, and are, being made are discussed. New and innovative solar technologies which have been spawn by DSSC research are also briefly introduced and their respective advantages and disadvantages considered.

To conclude, the third generation solar cell technology, the DSSC, has great potential as a future cost effective alternative to conventional photovoltaics. However there are some important hurdles which need to be overcome if this potential is to be realised. One of these hurdles is lower overall efficiencies when compared to conventional photovoltaics. One aspect which can have great impact here is the improvement of the light trapping properties of these devices. This area is the focus of this research and the following chapter will introduce and discuss in detail light trapping in conventional photovoltaics before focusing on the DSSC.

# Chapter 3

# Light Trapping in Photovoltaics

## 3.1 Introduction

Efficient photon management is important for all types of optoelectronic devices including solar cells where light trapping can considerably affect the overall performance of the cell [48]. The best imaginable photon harvesting technology for photovoltaic devices would effectively trap and/or concentrate light in a broadband angle-independent, and polarisation-independent fashion. 3D micro and nanostructures have demonstrated highly promising capabilities for the harvesting of incoming photons from a wide angle over a broad wavelength range. A wide variety of structures have been studied in conventional p-n junction and thin film devices including, nanopillars [49], nanopyramids [50], nanowires [51], nanocones [52], nanowells [53] and spherical nanostructures [54].

This chapter will give an overview of some light trapping systems and designs in, first, p-n junction solar cells before looking at how these methods are changed or adapted for their utilisation in DSSCs. It is worth bearing in mind that the implementation of light trapping structures in DSSCs is more problematic than conventional devices, since the $TiO_2$ charge transfer layer must also maintain certain properties. A light trapping structure used by a DSSC must also have a large surface area for dye adsorption, mesoporous channels for dye regeneration and good conductivity for electronic transport. The chapter will also explore the moddeling of light trapping structures in DSSCs and their characterisation via scanning photocurrent microscopy.

## 3.2 Light trapping in p-n junction solar cells

The most common method for the introduction of light trapping into solar cells is to texture the silicon surface, since silicon has high surface reflection this simple method can significantly reduce reflections improving light absorption in the cell [55]. Reflections at this surface can also be reduced by the addition of an anti-reflective coating which is already widespread in the commercial solar cell industry [56].

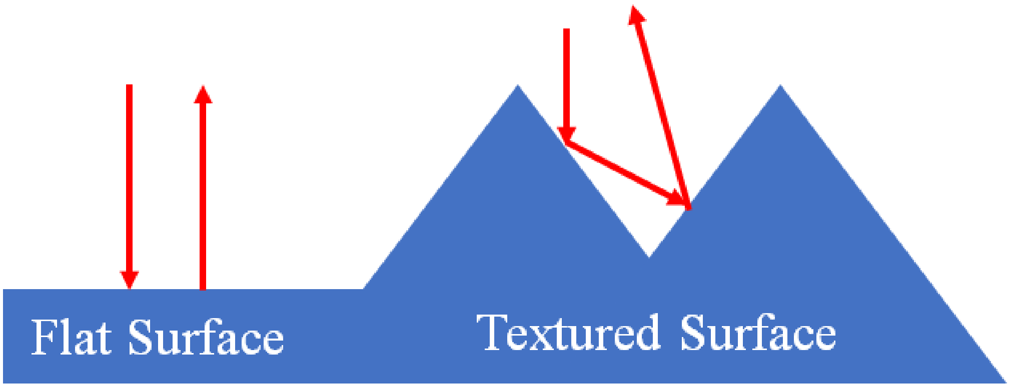

Figure 3.1: Planar silicon surface (left) and textured silicon surface (right).

These textured surfaces can also be applied to the transparent conduction oxide contacts in both Si solar cells and DSSCs, at the interface with the semiconductor. At the contact more thought has to be put in as to how light trapping textured surfaces are used since it is important that the contact remains highly conductive and highly transparent. The optimisation of the contact for its light scattering and electronic properties is essential for high cell efficiencies [57]. Highly reflective and textured back contacts are also widely deployed in commercial solar cells to scatter light that is not absorbed in the active layer of the cell. Thus increasing its path length way beyond that of the actual device thickness [58]. Although these techniques were first studied in conventional Si solar cells, with some modification they can be applied to a wide range of photovoltaic materials as well as to both thin-film solar cells [59] and DSSCs [60].

Alongside these approaches for light management thin-film solar cells also use the structure of the semiconductor material in the active layer to trap light and increase the efficiency of the cell. Thin-film solar cells have a much shorter optical path length so a higher absorption coefficient and/or excellent light trapping is of even greater importance. Focusing on this layer can also help to reduce materials cost as higher efficiencies can be achieved with less semiconductor material. Research has shown that a great variety of nanostructures can have unique photon harvesting capabilities [61], these include nanowires, nano and micropillars, nano and micropyramids, nanocones, nanodomes, nanoparticles and nanospheres. These structures can possess impressive photon trapping capabilities and have been shown to increase the overall efficiency of the cells by taking advantage of a smooth gradient of effective refractive index, confining light in the structures by waveguide modes and/or localising electromagnetic wave energy via plasmonic effects [62]. Research into these structures and their effects on solar cell performance are examined in more detail in the coming pages.

### 3.2.1 Nanowires and pillars

Nanowires have been investigated for their use in thin film solar cells with significant theoretical and experimental work being carried out on a variety of materials including Si, InAs, InP, ZnO and more [49]. They have been shown to have low reflective losses compared to planar thin films [63], and can increase the path length of light up to 73 times over planar devices [64]. With the careful optimisation of density and length Si nanowire arrays can halve the amount of semiconductor material whilst also boosting the absorption of solar radiation by up to 25% [65].

Another attractive prospect is the use of nanopillar arrays which have been extensively fabricated and studied for efficient photon management over a wide range of semiconductor materials [49]. Nanopillars are advantageous over nanowires for use in solar cells due to their smaller surface area which leads to reduced surface recombination, an unfavourable electronic process which is a major concern for nanostructures solar cells [66]. However it is worth noting that this smaller surface area would negatively affect DSSCs since a high surface area needs to be maintained for dye absorption.

Simulation studies have shown that a detailed relationship between the absorption of light for a nanopillar array, and the nanopillar pitch, length and diameter should be expected [49]. Experimental results that have presented detailed studies of a single crystalline Si, decorated with Si nanopillars thin film show this to be the case [67]. First decorating the planar Si with a nanopillar array was found to significantly increase light absorption in the layer. This absorption can be further increased by manipulating the pitch of the nanopillars, with light absorption around 2.5eV (the highest energy density region in the solar spectrum, as seen in figure 2.4) being enhanced with the array periodicity being increased from 100 to 500nm. Which can be attributed to suppressed reflection and transmission of incident light. Further increasing the pitch from 500 to 700nm serves to decrease the light absorbed at 2.5eV. It was also found that absorption is dependent on the thickness of the active layer with the optimal cell having an 800nm thick planar Si layer below a 1000nm high nanopillar array. Showing that careful optimisation of the physical dimensions of the active region must be carried out to determine the most effective way to implement light trapping designs into the cell.

To further enhance the broadband optical absorption capabilities multi-diameter nanopillars have been studied. With ordered arrays of dual diameter, small diameter tip and large diameter base, showing impressive absorption capabilities across the solar spectrum [68]. Scanning electron microscope (SEM) images of these dual diameter nanopillars are shown in figure 3.2b.

Larger crystalline Si radial p-n junction micropillar arrays with diameter 7.5µm and height 25µm have shown some of the most impressive enhancements. With a twofold increase in the solar conversion efficiency being measured over the corresponding planar devices [70] shown in figure 3.3. This large improvement is attributed to the much higher short circuit current, the primary factors for this increase being the increase in effective path length of the light due to scattering and multiple reflections within the pillar array structure.

Detailed theoretical and experimental studies of many material types and corresponding optimal physical dimensions demonstrate that the micro and nanopillar array architecture is an effective way to improve solar power conversion efficiencies by significantly improving the light trapping in the cell [71].

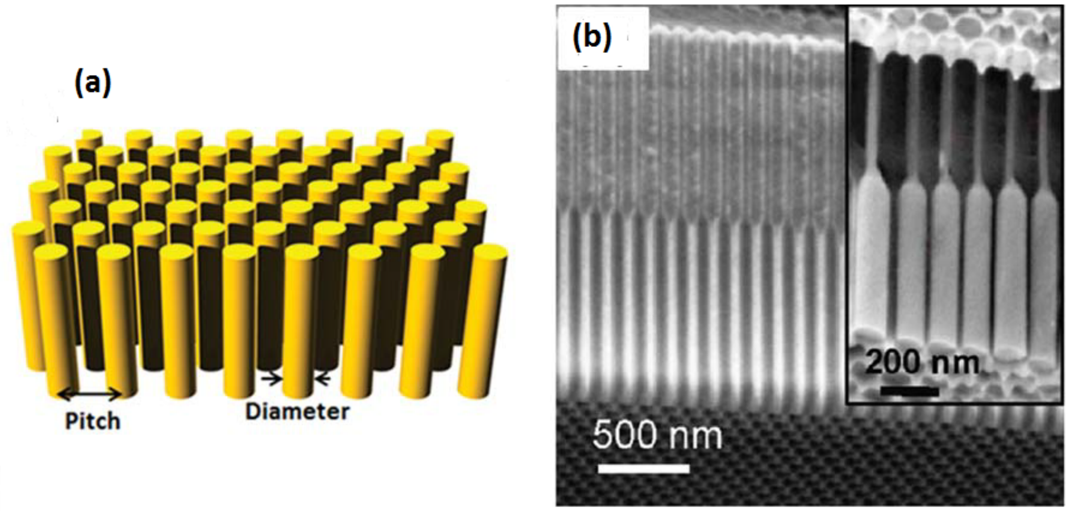

Figure 3.2: Schematic of single diameter array. (b) SEM of image single diameter nanopillar array adapted from [67] insert shows multi-diameter nanopillar array adapted from [69].

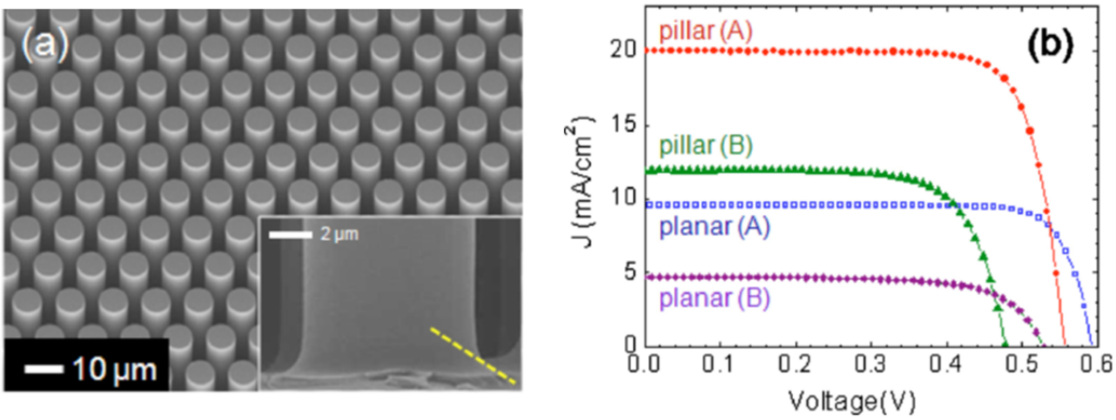

Figure 3.3: (a) SEM image of nanopillar array. (b) Light $J-V$ characteristics for planar and pillar array solar cells. Adapted from [70].

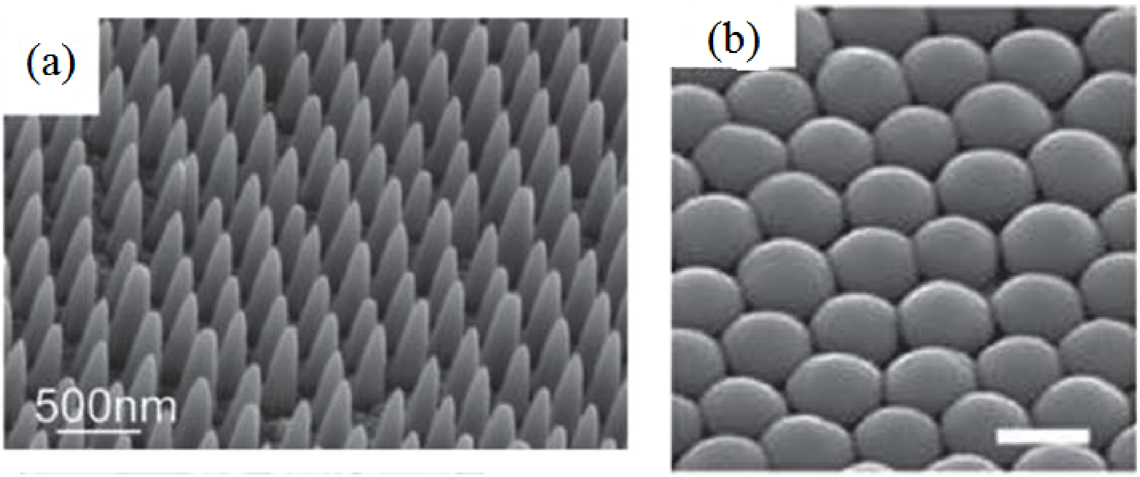

Figure 3.4: (a) SEM of Si-nanocone array. Adapted from [74]. (b) Ag-nanodome array at back contact. Scale bar 500nm. Adapted from [76].

### 3.2.2 Other positive light trapping structures

There are a variety of other 'positive' structures, that is, the structures protrude out from the substrates into free space, which have been extensively studied for their light trapping capabilities. These include nanocones, nanopyramids, nanodomes, nanospheres and nanoparticles.

Nanocones are widely considered to be excellent structures of light absorption for thin films solar cells due to their graded transition of the effective refractive index between the structure and the air [72, 73]. These structures have been widely fabricated and studied, crystalline-Si nanocones have been shown to extract photo-generated carriers efficiently, whilst also increasing the optical path length of the photons inside the material thus increasing the absorption [74]. Nanopyramids, much like nanocones also provide a gradual change of the refractive index and have demonstrated enhanced absorption over a broad range of wavelengths [75].

Nanodomes are considered less favourable structures for light trapping in the active layer when compared to nanocones and pyramids. However metal nanodomes have been used to scatter light back into cells at the back reflector or electrode, with the addition of this layer demonstrating an improvement of a 26% in the short circuit current when compared to a planar metal contact [76].

Nanospheres and nanoparticles are commonly utilised for light scattering in DSSCs and will be covered in more detail later. However they have also found uses in p-n junction solar cells where Si nanosphere surfaces have been shown to improve absorption when compared to planar Si surfaces [77].

The introduction of metal nanoparticles have shown to strongly localise incident light within their vicinity. These behaviours have been harnessed as unique light scattering schemes to improve absorption. Plasmon enhanced Si solar cells, which use silver particles to introduce surface plasmonic effects resulted in improvements in absorption and short circuit current [78].

### 3.2.3 Negative light trapping structures

Reports on ‘negative’ structures, that is, nanoholes and nanowells are less common in the literature. Structures with cylindrical cavities provide natural geometric confinement for incoming photons, thus the photon trapping process is expected to be different from positive structures [53].

Fan et al. have presented an approach to fabricate self-organized nanowell arrays with precisely controlled geometries. They go on to demonstrate a systematic investigation of the structures photon trapping properties combining experiment and simulation. It was found that a proper periodicity greatly facilitates the photon trapping process owing to optical diffraction and resonance in the wells. Their study has also showed that Si-nanohole arrays could outperform Si-nanorod arrays in cost performance, due to a further reduction in materials [79]. Examples of these structures can be seen in figure 3.5a and b.

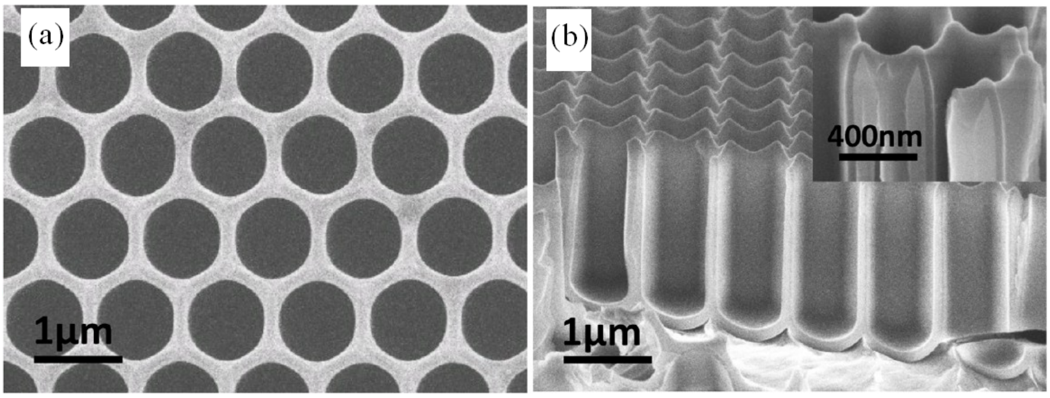

Figure 3.5: (a) SEM images of nanowells from top-view. (b) Cross-section. Adapted from [53]

## 3.3 Light Trapping in DSSCs

With respect to DSSCs there are a number of new considerations that need to be taken into account when fabricating light trapping structures. DSSCs require the nanocrystalline charge transport layer to maintain a high surface area for dye adsorption, the layer must also have favourable electrical contiguity with the conducting glass substrate, and have a mesoporous structure to allow the electrolyte to regenerate all dye molecules in the layer. Another important difference is the orientation of the structures in DSSCs, the incident light coming through the conducting glass substrate from which the $TiO_2$ structure protrudes, essentially upside-down when compared to most structures used to trap light in p-n junction solar cells. There are a number of novel and interesting methods that are used to create these complex light trapping structures. Some of these methods are parallel or similar to the methods used for p-n junction solar cells whilst others are unique and tailored to tackle the more specific requirements of the DSSC.

### 3.3.1 Hierarchical structures

One of the most effective ways for light trapping to be implemented into DSSCs is to use hierarchical structures, whereby there are two or more structures on different length scales. Most of the top performing cells utilise simple 'two level' hierarchical structures to enhance light trapping in the cell (seen in figure 3.6a), including cells that have made it to the commercial market [80]. The optimal size of $TiO_2$ nanoparticles for dye adsorption was found to be $\sim$ 20nm [81], after a layer of this size is applied to the substrate another layer of larger $\sim 350 - 400$nm nanoparticles is applied, this layer's function is to scatter light back into the active layer of the cell to increase absorption. The addition of a $\sim$ 400nm diameter scattering layer has been shown to improve the efficiency of cells by up to 11% [20], an impressive improvement for a very simple and easily applicable procedure. Figure 3.6a shows a diagram of the light scattering layer introduced to DSSCs.

More ambitious multilevel hierarchical structures have also been fabricated and investigated. An example is the fabrication of complex three-level hierarchical $TiO_2$ structures which have been synthesised using an ion-modified hydrothermal method and subsequent $TiCl_4$ treatment [82]. Here the highest order is one comprised of nanourchins, the second is an array of nanowires and the final is nanoparticles attached to the surface of these nanowires. Figure 3.6 b shows SEM image of nanourchins (structures with spiked nanoantenna) and figure 3.6c shows high resolution SEM image of the nanowires. These cells achieved solar power conversion efficiency of 3.24% which is a 103% improvement over their counterpart nanowire array cells.

### 3.3.2 The template method

One interesting and reliable method for producing a favourable hierarchical structure is by using a template. Here a polymer template is fabricated, the template is infiltrated by $TiO_2$ nanoparticles and subsequently removed leaving behind the desired hierarchical $TiO_2$ structure. This is an attractive method for creating more complex 3D structures and as such has attracted a lot of attention in the research community [83, 84, 85].

There are a number of ways template fabrication can be approached. Perhaps the most simple is the use of colloidal polymer spheres of various sizes, carefully selecting particle size can lead their self assembly by favourable packing. Whereby the inverse will have a complex 3D structure which could facilitate light trapping. Colloidal latex spheres of 1500, 400, 300 and 150nm diameter with proportions of 82: 12: 4: 2 respectively have been chosen to favour 'Apollony' packing, a

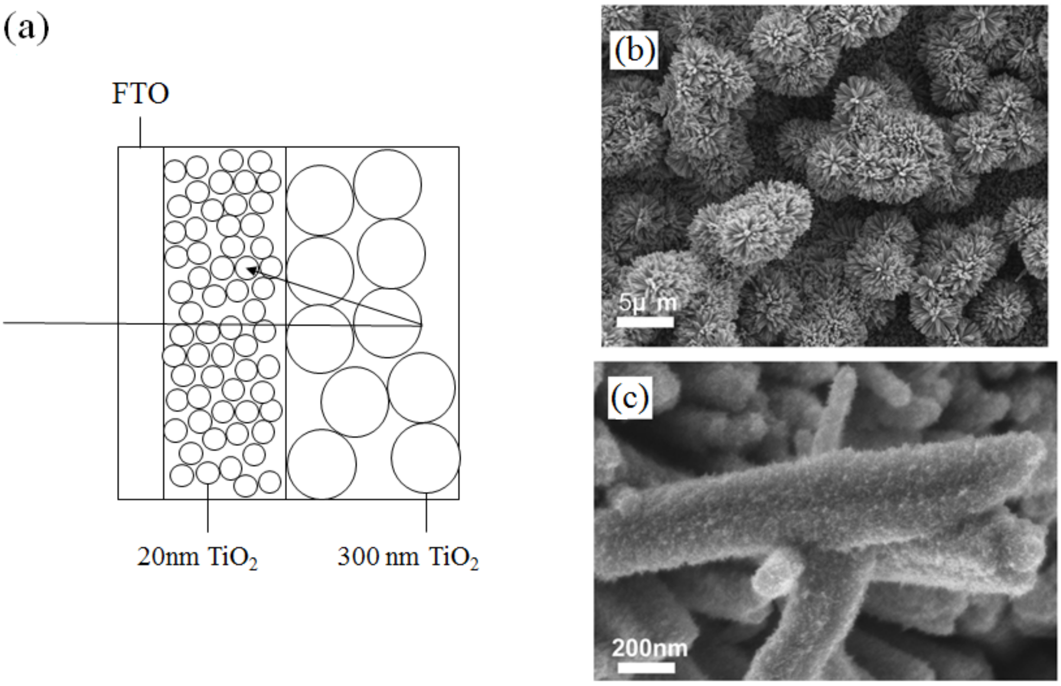

Figure 3.6: (a) Schematic of light scattering layer. (b) SEM images of nanourchins. (c) High resolution SEM image of nanowires protruding from nanourchins [81].

quasi fractal geometric structure [86]. $TiO_2$ particles were then synthesized within the inter-particle pores of the latex film. The polymer template was selectively removed at 450°C to obtain the inverse structure. This quasi fractal architecture was reported to improve the total efficiency value of the cell by a factor of 5. However overall efficiencies were low due to the method of $TiO_2$ synthesis. Figure 3.7 shows a geometric Apollonian gasket and SEM images of the resulting $TiO_2$ structure.

Another method is to use interference or multi-beam lithography, or even a dual templates method combining lithography and colloidal latex particles. For example Cho *et al.* present work where they first fabricated a microscale 3D structure using UV light to drive the polymerisation process in a photoresist [87]. The resulting microstructure is then filled with latex spheres on the nanoscale by spin coating. Sol-gel chemistry was then used for the coating of the $TiO_2$ layer. Again both polymers are then selectively removed by calcination. The resulting structure is a two level hierarchy porous $TiO_2$ electrode which was shown to have performance enhancing effects for the solar cell. Figure 3.8 shows SEM images during the electrode fabrication process. Note that here the template is coated in $TiO_2$

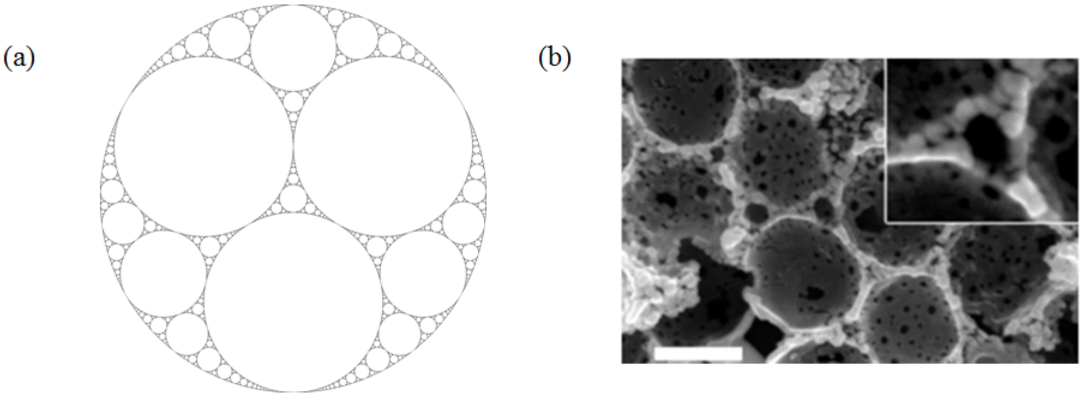

Figure 3.7: (a) Apollonian gasket. (b) SEM images of resulting $TiO_2$ structure. Adapted from [86].

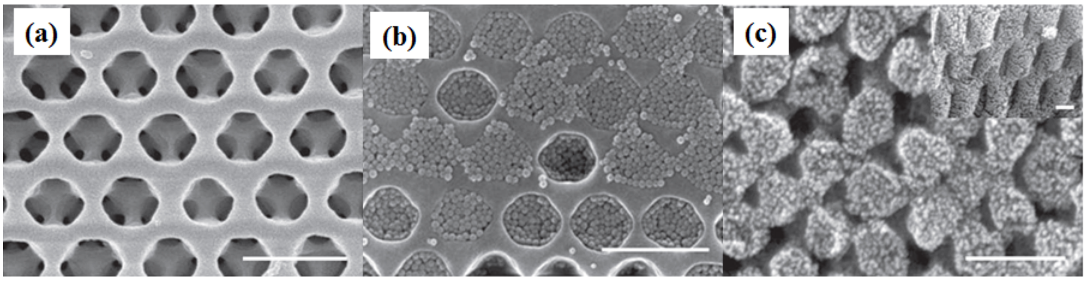

Figure 3.8: (a) Polymer structure fabricated via interference lithography. (b) Two-level hierarchical polymer structure. (c) Inverse $TiO_2$ structure [87].

and not in $TiO_2$ nanoparticles, therefore the surface area available for dye adsorption is reduced. Whilst these designs were able to show light trapping capabilities, the reduction in surface area was enough to reduce their performance below that of the randomly assembled nanoparticles control cells, showing that it is critical to maintain the other desired properties of the charge transport layer. Observe that these fabrication methods are limited to what 3D structures can be created, by either packing or interference lithography and does not allow for a high degree of design to be implemented.

Similar to the template methods is to use a simple stamping method. Here a negative polymer stamp (or other material) is fabricated, the pattern is then transferred to the $TiO_2$ electrode by mechanically stamping the pattern before the viscus nanoparticle/solvent paste had dried. Micropyramids designed specifically to make incident light undergo total internal reflection within the pyramids showed increases of up to 15% in the power conversion efficiency over the best performing

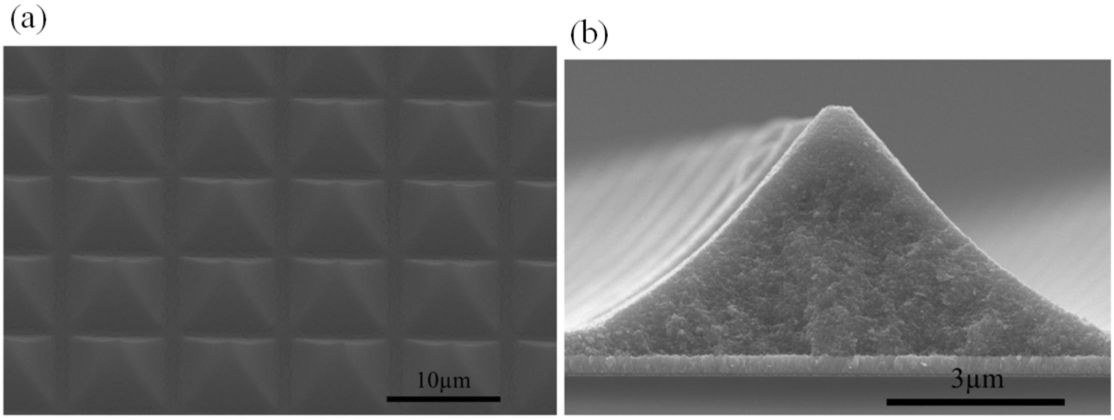

Figure 3.9: SEM images of titania hierarchical light trapping pyramids [88].

planar control solar cells [88]. SEM images of these microstructures comprised of $TiO_2$ nanoparticles are shown in figure 3.9.

Whilst this method cannot produce complex internal three 3D structures like the template method it does have an advantage in that high quality $TiO_2$ with its desired properties is much easier to maintain. Synthesising nanoparticles within the templates or infiltrating them is a complex and difficult procedure which can lead to reduction in the quality of the film.

### 3.3.3 Nanowire and nanotube arrays

One promising idea to facilitate light trapping is to replace the nanoparticle film with a dense array of single-crystalline nanowires or nanotubes which could be grown vertically from the substrate. Electron transport in crystalline nanowires and nanotubes is expected to be several orders of magnitude faster than percolation through a random polycrystalline network, with measurements showing significant improvements in electron transport to support this idea [89].

However efficiency is limited due to increased surface recombination and a reduction of the surface area when compared to nanoparticles [90]. This issue can be mitigated by having strands of nanoparticles forming nanowire-like chains, cells incorporating these structures have shown excellent performance with efficiencies above 10% [91]. Figure 3.10 shows a diagram of a dense nanowire array DSSCs

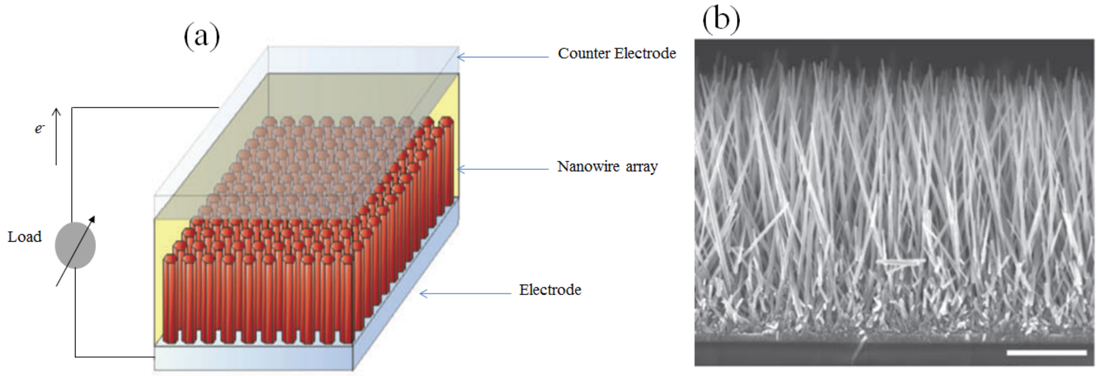

Figure 3.10: (a) Schematic of nanowire array DSSC. (b) SEM of nanowire array on FTO contact, scale bar, 5µm. Adapted from ref [89].

with corresponding SEM image. Another disadvantage when using nanowire and nanotubes is that fabrication techniques are complex and so inevitably more expensive.

### 3.3.4 Light trapping in nature and DSSCs

Over billions of years of evolution nature has created many interesting and novel materials, structures, methods, tools and systems from which scientists and engineers can, and do, take a great deal of inspiration. Water collection on wetted spider silk, fog collection systems in cactus, anti-fogging properties of mosquito compound eyes, water capture and wing-locking devices of the beetle, low drag shark skin, the highly adhesive geckos feet are all excellent examples of some of nature's novel solutions to the challenges these respective organisms face. There are also some interesting light trapping and scattering structures that have been developed by the evolutionary process: beetles and butterflies show characteristic colours due to light scattering [92], butterfly wings also act as solar collectors for heating purposes [93] and diatoms, microscopic marine organisms, trap light using silica exoskeletons known as frustules [94].

By utilizing ideas from nature, biomimetic designs, or using these structures directly can serve as the basis for many new innovations in science and technology, including creating highly efficiency light trapping structures for use in DSSCs [95].

### Butterfly wings

Butterflies extend their wings in order to absorb solar radiation to sustain their body temperature, the physical mechanisms of these optical structures are well documented [96]. Reports show that microstructures on the surface of the wings act as effective solar collectors, or solar blockers in different regions. Light is absorbed by the scales and the generated heat is quickly conducted away by the solar blocker ridges due to their lower temperature [97].

The exact light trapping microstructures differ slightly from species to species but their function remains the same. A good example is the species *Trogonoptera brookie*, which utilises a quasi-honeycomb structure to trap light [98]. Figure 3.11 shows the macroscopic wing structure and the microstructure ridges and light trapping quasi-honeycomb pattern. Light trapping silica structures have been fabricated using this wing as a bio-template. A silica inverse of the structure has been synthesised using a sol-gel technique and subsequent selective etching, with this structure showing some impressive light trapping capabilities [99].

This idea has been taken one step further with butterfly wing structure beings incorporated into the photoanode of a DSSC. The honeycomb like structure from two different butterfly species, *Papilio paris Linnaeus* and *Thaumantis diores*, are first soaked in a titanium sulphate. Then transferred to a preprepared $TiO_2$ film before the organic material is removed via calcination. This quasi-honeycomb light scattering layer was shown to improve light absorption in the $TiO_2$ layer [100].

### Diatoms

Diatoms are single celled algae that are ubiquitously present in almost every water habitat on earth [101]. Diatoms are responsible for approximately one fifth of the production of organic compounds from carbon dioxide on Earth and make up a quarter of all plant life by weight [102]. Apart from their ecological significance they are known for their porous silica exoskeletons which they produce called frustules. These frustules are intricately patterned hierarchical structures on the micro and nanoscale, they are specifically designed for light scattering and trapping [103, 104]. Diatoms began evolving at a time in the Earth's history when there was

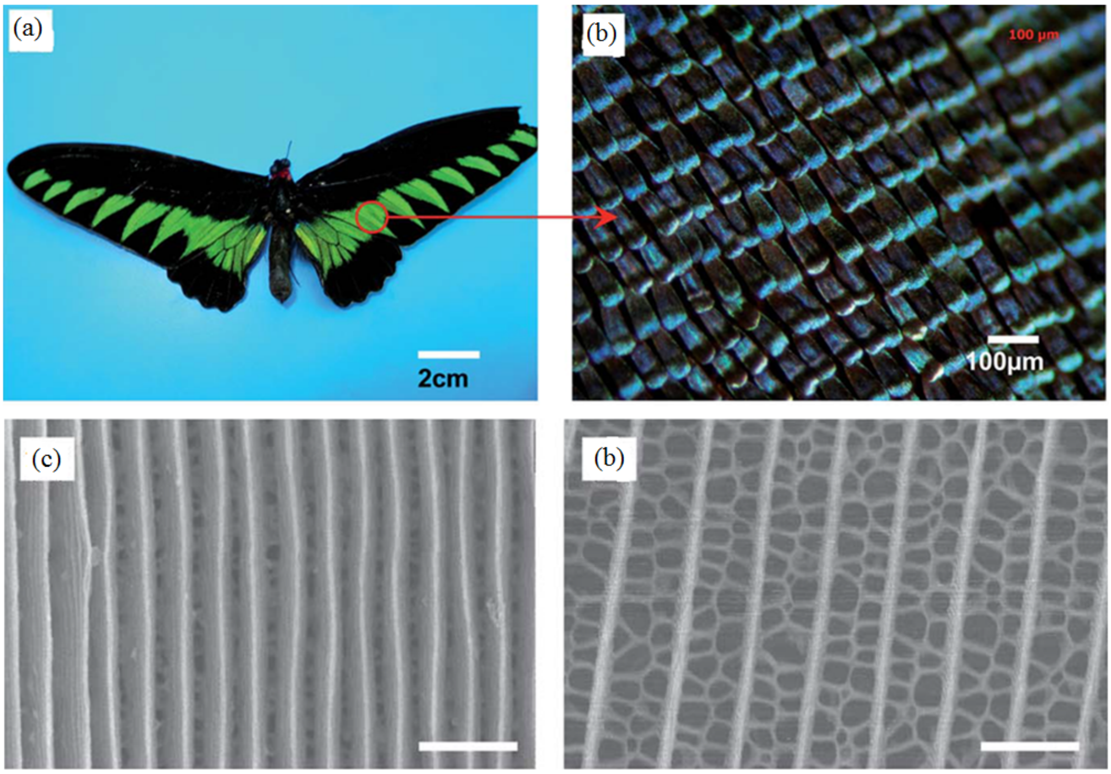

Figure 3.11: (a) Image of *trogonoptera brookia*. (b) Optical image of wing scales. (c) TEM images of Type-1 structure scale 5µm. (d) Type-2 structure scale 2µm. Adapted from ref [99].

little carbon dioxide in the atmosphere, so they developed silica frustules which help to concentrate carbon dioxide and efficiently absorb light into the organism increasing the rate of photosynthesis. The size and shape of the frustules differs from species to species; they can be circular, oval, stick shaped and many more, but their function remains to efficiently trap carbon dioxide and light. Figure 3.12 shows various examples of diatoms frustules. The remarkable optical properties of these frustules are well understood and their use in a number of applications has been suggested or applied. Solar cells, batteries, electroluminescent devices and their use as chemical sensors are all being considered as potential applications [105, 106].

Diatoms frustules have already been used in an attempt to increase the efficiency of DSSCs. After the removal of all other organic material the silica frustules have been used as a light scattering layer, significantly improving the efficiency of the cell when compared to a planar control, however they were not tested against a simple $400nm$ $TiO_2$ nanoparticle scattering layer [107]. In other studies frustules were coated directly with $TiO_2$, significant improvement of power conversation efficiency was observed with an increase of up to 30% after optimal coating cycles [95]. Figure 3.13 shows the schematic of a diatom frustule and corresponding $J-V$ characteristics.

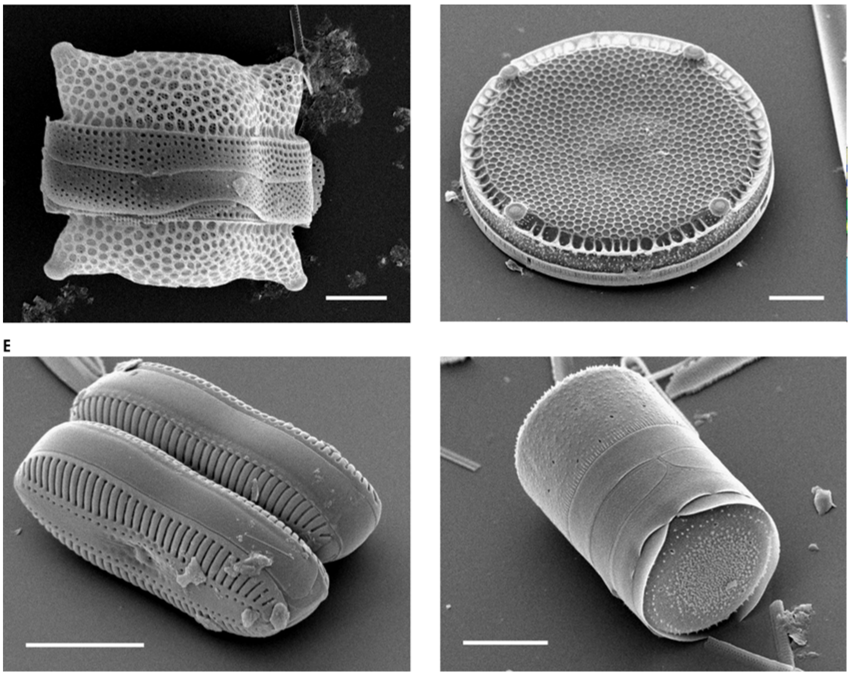

Figure 3.12: TEM images of frustules from four different diatom species. Scale bar $10\mu$m. Adapted from [103, 104].

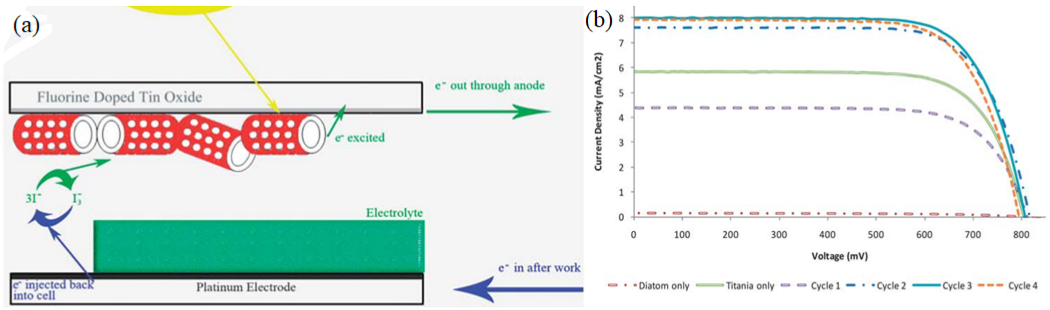

Figure 3.13: (a) Schematic of diatom frustule DSSCs. (b) $J-V$ characteristics. Reproduced from [95].

## 3.4 Modelling light trapping in DSSCs

Work on the modelling of DSSCs in the literature has predominately focused on the electronic processes in the device. This includes all aspects of electron transfer in the cell such as; transfer between the dye and $TiO_2$ [108], transfer from the counter electrode to the redox couple [109] and the regeneration of the dye molecules [110]. Also the modelling of electron transport through the $TiO_2$ film is widely reported in the literature [111, 112]. However theoretical and numerical studies of the optimisation of light trapping designs for DSSCs are less common [113, 114, 115], with most focusing on the use of scattering layers [113, 114] which have already been studied extensively experimentally. One reason for this is the complicated optical nature of 3D sub-micron nanoparticle light trapping structures [116], which can in turn affect dye loading and thus light absorption. Optical models of DSSCs in the past have mostly assumed simple Lambert-Beer absorption [117]. However some consider this approach inadequate for 2D and 3D light trapping structures where a different approach is required, with the use of 2D finite-difference time-domain (FDTD) [116, 88] and finite element methods (FEM) [118, 115] being used to solve Maxwell's equations.

Ray-tracing is a powerful tool for the examination of optical systems. Including solar cells devices where performance of a cell can be analysed using the comparison of metrics such as path-length enhancement, reflection of front and back contacts, absorption etc. In the simulation rays are tracked from a source until they meet a material interface, where the ray's direction changes due to reflection, refraction, diffraction or scattering. The change in direction is calculated using a Mote Carlo approach, at the interface the direction of the scattered rays is assigned randomly within a probability distribution determined by the material properties (refractive index, absorption).

Ray-tracing has been used for decades for optical models of conventional solar cells. Today it is widely used for examining many aspects of these solar cells, such as the use of solar collectors [119, 120], arbitrary textured surfaces [121] for anti-reflection and light trapping, entire solar cells modules [122], and importantly for light trapping [123] and light trapping in thin film in solar cells with designed micron and sub-micron structures [124], similar to light trapping thin films of $TiO_2$ used in DSSCs.

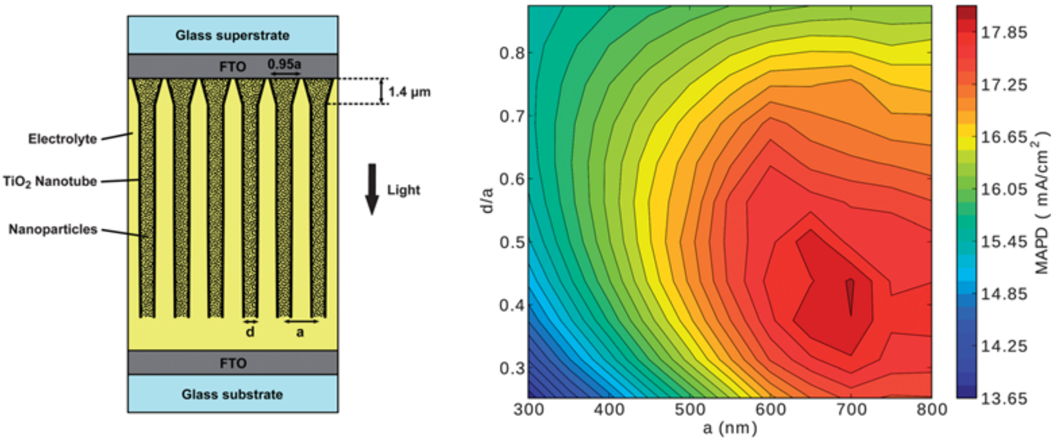

Figure 3.14: (a) Schematic of nanotube/nanoparticle design. (b) Graph showing simulation results for optimal dimensions of a and d/a for increased photocurrent.

Whilst ray-tracing is commonly used for analysing conventional solar cells its use in DSSCs research is less extensive. There are however a number of useful reports looking at planar $TiO_2$ DSSCs [125] and DSSCs using a scattering layer to improve light harvesting [114] and some investigating light trapping structures themselves [115]. And also utilising ray-tracing to investigate the effects of UV blocking layers, which must be used to avoid photo catalysis effects on the dye over longer time periods, have on DSSC performance[126].

Wenger *et al.* [125] present a detailed ray-tracing study coupled with electronic modelling to for a complete picture of The DSSCs. Their optical model allows for the correct computation of the dye absorption function under many different cell conditions. With the coupled model, the different optical and electric losses can be quantified. Their comprehensive loss analysis can help pave the way for a systematic, model-assisted, optimization of DSSC. Galves *et al.* [114] also use a coupled ray-tracing optical model and electrical model, however this time with the introduction of a 300nm $TiO_2$ nanoparticle scattering layer. Examining these larger particles mixed in the absorbing layer alongside a scattering layer on top of an smaller particle absorbing layer showed improved results when the scattering layers and absorbing layers are separated. Kennedy *et al.* [126] use ray-tracing simulations to show that the use of novel Eu films which can act as performance enhancing UV blocking layers for DSSCs.

The investigation of Light trapping structures is less common however Foster et al. present a coupled ray-tracing and electronic model study showing that their DSSC design can enhance the light absorption relative to a planar $TiO_2$ conventional design [115]. In this work the authors use a 2D formulation of the finite element method to solve Maxwell's equations for their arbitrary cell geometries. The fraction of light absorbed by the cell is calculated over a range of frequencies selected to reflect the solar spectrum. Their designs consists of periodic array of large-diameter TiO2 nanotubes filled with TiO2 nanoparticles. Regions between the nanotubes are filled with electrolyte. The array dimensions are then optimised to focus trapped light within the nanotubes interior. Figure 3.14 shows a schematic of their design 3.14a and their results from their numerical study showing the optimised dimensions 3.14b. For their optimised nanoparticle filled nanotube designs solar absorption was able to be improved by 33% due to enhanced anti-reflection, light confinement and back reflection. The optimal dimensions for these nanotube structures were found to have periodicities of approximately 500nm with nanotube diameters of half the periodicity.

Another example of a detailed numerical study aimed at optimising light trapping structures, as previously mentioned, is optimised micro-pyramid array designed to make incident light undergo total internal reflection within the structure [88], as depicted in figure 3.15. In a planar $TiO_2$ system any reflected light passes back through the cell only once as shown in figure 3.15a, in this pyramid system the light can undergo multiple reflections, figure 3.15b, significantly increasing the optical path length thus increasing the likelihood of an absorption event occurring. In this work the absorption enhancement was calculated for their $TiO_2$ micro-pyramid designs and a PbS quantum-dot sensitiser film. To determine the absorption enhancement two-dimensional finite difference time-domain simulations were performed on these layered structures. Pyramid wall angle was varied and absorption enhancement simulated to find the optimal dimensions. Figure 3.16 shows simulation results for absorption in the layered structures with various angles of pyramid walls and a planar control.

Although these results show that a pyramid angle of $80^o$ has the best absorption enhancement over the planer control, a pyramid angle of $54.7^o$ was selected for fabrication for practical reasons. The group used anisotropic etching of silicon to fabricate a template which is used to fabricate polymer stamps which in turn are used to pattern the $TiO_2$. Silicon's natural etch plane of $54.7^o$ directly facilitates implementation of pyramids with these side wall angles. When these

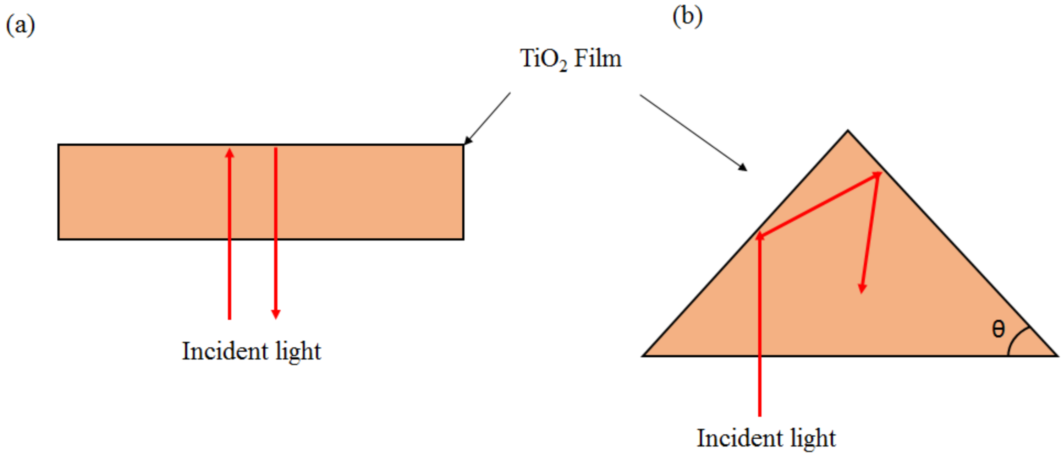

Figure 3.15: (a) Light reflections in planar TiO$_2$. (b) Increase in optical path length due to total internal reflection.

structures were incorporated into a solar cell device they were shown to enhance the photocurrent by up to 24% over planar controls.

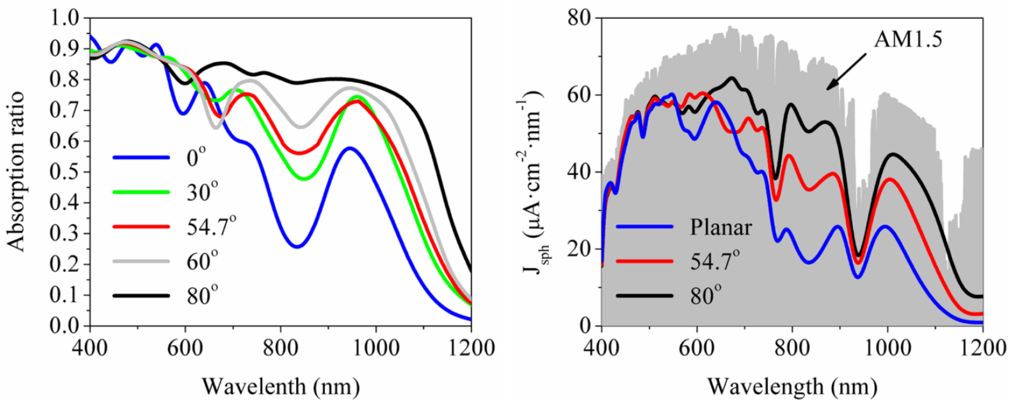

Figure 3.16: Absorption and spectral photocurrent enhancements from simulation results of various angles of pyramid walls [88].

Note that in the two reports discussed in detail these simulation studies are limited to what structures can be experimentally produced using established fabrication methods. They are not designed for their pure light trapping capabilities and the other semiconductor charge transport layers required properties. Showing there is room for new fabrication methods that can produce electrodes with more complex 3D light trapping structure. This work will focus on new and novel fabrication methods for light trapping structures in DSSCs, using the sub-micron 3D printing technique two-photon polymerisation that could introduce a high level of control using layer-by-layer fabrication.

## 3.5 Characterising light trapping structures with SPCM

SPCM is a powerful experimental technique for investigating local conditions in semiconductors and as such has been used extensively in the analysis of semiconductor micro and nanostructures such as nanowires, nanotubes, quantum dots and graphene [127]. This also it an excellent candidate for the characterisation of light trapping structures microstructures in solar cells and DSSCs. The technique is similar to other scanning probe techniques such as scanning tunnelling microscopy (STM) and atomic force microscopy (AFM), except in this technique the physical probe tip is replaced with a focused light beam for excitation. Another way to utilise this technique is to map local efficiency of structures inside solar cells, such as nanowires [128]. In this work we are able to map the photocurrent response from patterned light trapping areas of the cells and also planar areas of cell comparing the structures effectiveness at increasing photocurrent generation.

This section will first look at the general background of the technique and how its advantages have been exploited by the research community. It will then go on to discuss its relation to solar cell research and its usage in this area. Next our experimental set-up and methods will be detailed.

#### Background and applications

Interest in SPCM as a useful tool for the investigation and characterisation of local conditions in semiconductors has been growing ever since the beginning of scanning probe microscopy and semiconductor physics in the mid 20th century [129]. The influential 1984 paper by Marek [130], which provided a quantitative theory for the evaluation of light induced profiles at grain boundaries along with corresponding experimental data, gave even more weight to this growing interest. One important reason why this technique is attractive is its ability to gather a wide range of information on the structures under investigation. SPCM maps can be used to find and localise both photosensitive regions and defects in the sample. SPCM can also reveal information about thermoelectric effects, carrier diffusion lengths, doping distribution and the internal electric field [127]. The ability of this technique to characterise structures in a device and also look at fundamental material properties has, today, seen it become a common tool for the analysis of semiconductors.

With the rise of micro and nanostructures in semiconductor physics it is no surprise that SPCM, with its excellent ability to investigate local conditions, became a popular tool for the characterisation of these structures. Spearheading this work was the use of SPCM for the analysis of carbon nanotubes. 2004 work by Balasubramanian [131] on carbon nanotubes presented photocurrent maps showing increased response close to one of the two electrodes. This response was linear to laser power and was at a maximum for light polarised parallel to the axis of the nanotube. With the authors suggesting this localised photocurrent was originating from the built in electric field associated with the Schottky barrier. SPCM has been used to analyse nanowires in both field-effect tranistors, where is has been effective at showing devices function similarly to traditional metal-oxide semiconductor field-effect transistors [132], and solar cells [128]. SPCM has been utilised to image Schottky and ohmic contacts in PbS quantum dot devices [133]. Finally there are various studies of graphene and other two dimensional semiconductor devices using SPCM [134, 135]. These examples show the versatility of the technique in studying a wide range of properties in various semiconductor micro and nanostructures.

By using scanning near-field optical microscopy photocurrent maps with a resolution beyond the diffraction limit of the probing light can be achieved. In this powerful technique the laser is focused through an aperture with a diameter smaller than the excitation wavelength, illuminating only the area of the sample that lies directly under the tip aperture. Using this technique resolutions of 50 to 100nm can be achieved. Shear-force feedback modes can be used to keep the tip within 10nm of the surface giving topological data alongside photocurrent data. These combined high-resolution topological and photocurrent maps are an excellent tool for the analysis of semiconductor nanostructures and solar cells [136, 137].

### SPCM of solar cells

SPCM is also a valuable tool for the characterisation of solar cells, with the study of nanostructures and material properties being readily available, many different types and aspects of solar cells can be studied. For example material properties have been analysed by producing photocurrent maps via SPCM of nanostructured single-crystal methylammonium lead iodide perovskite materials, which is a common material used in perovskite solar cells [138]. These maps reveal carrier diffusion lengths much greater than the films themselves indicating greatly improved carrier lifetime and mobility in these nanostructures. They also showed increased photocurrent towards the edge of the nanostructures which was attributed to strong light coupling. Howell *et al.* have used SPCM for the spatial mapping of GaN/InGaN nanowire array solar cell [128]. Here SPCM helps to give understanding to spatial variations in carrier generation and collection over the cell, important for the development of heterogeneous nanowire array solar cells. Figure 3.17 shows an AFM map alongside a photocurrent map for these nanowire array solar cells. The AFM image in figure 3.17b shows nanowire arrays interrupted by defects. It can seen from the photocurrent map that these defects have an impact on the photocurrent that is over a larger area than their physical extent, which seen in the AFM image.

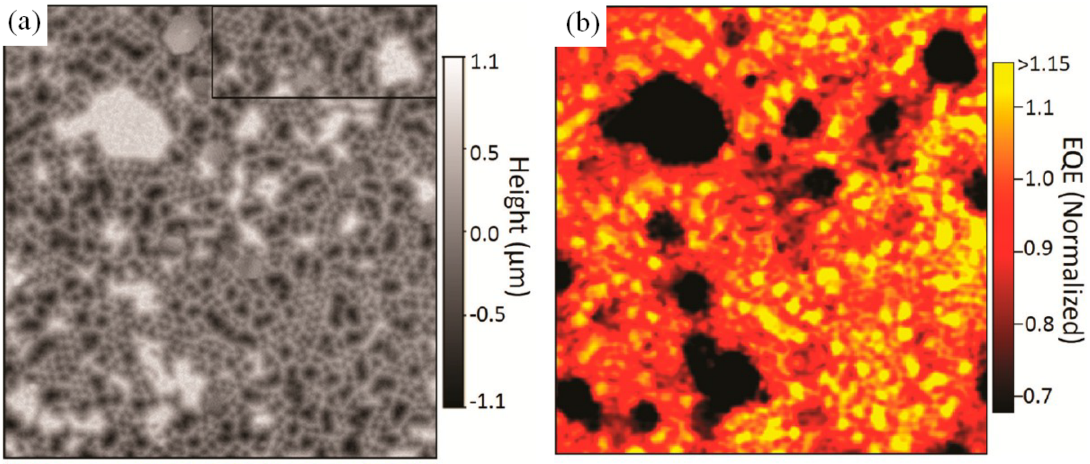

Figure 3.17: (a) AFM surface topography. (b) Corresponding photocurrent map. Adapted from [128].

SPCM has also been used for the characterisation of DSSCs. With spatial maps used to investigate non-uniform photocurrent generation in DSSCs, as well as looking at the effects of intentional damage to the electrode [139]. SPCM has also been used to measure the carrier diffusion length of $TiO_2$ nanoporous electrodes in conventional DSSCs, which were found to be 60-1000µm [140]. This diffusion length was also found to correlate well with cell efficiency showing that improvement in the diffusion length is important for the optimisation of DSSCs. More recently high resolution sub-micron SPCM, appropriately 10 times greater than previous SPCM reports, have been presented with simultaneous luminescence images [141]. Despite these applications of SPCM there are no reports on the study of micro or nanostructured DSSCs electrodes. This work presents the first application of the SPCM technique to the light trapping microstructured DSSCs.

#### Artefact and defect detection in solar cells

Another interesting use of the SPCM technique is the detection and spatial characterisation of defects and artefacts that are invisible for conventional microscopy techniques such as optical or electron microscopy. McNeill *et al.* were able to use SPCM to characterise defects that were deliberately introduced into organic solar cells [136]. They were also able to show that artefacts seen in optical and topological measurements did not necessarily lead to a local reduction in photocurrent generation around these artefacts. Defect introduction and subsequent characterisation of these defects using SPCM have also been shown in DSSCs [142]. The group also measured whole 4mm$^2$ cells for which photocurrent maps were obtained under different electrode conditions, such as partial film delamination and electrodes that were smoothed with ethanol vapour. The effects of these conditions, such as cracking in the partially delaminated films, were readily resolved and characterised with their SPCM technique. Figure 3.18 shows photocurrent maps of whole DSSCs with the control being shown in figure 3.18a and cracking due to delamination in 3.18b. What can be clearly seen is that this large scale millimetre scale cracking leads to significant reductions in local photocurrent.

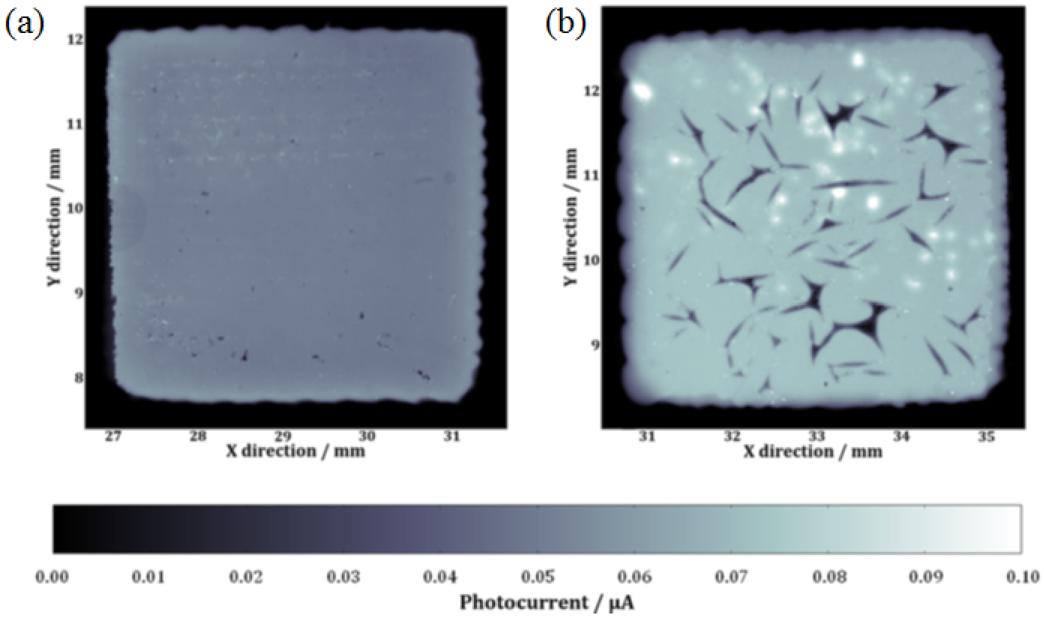

Figure 3.18: Photocurrent maps showing (a) Control and (b) Cracking due to delamination. Adapted from [142].

## 3.6 Summary and conclusions

This chapter highlights the positive impact light trapping structures can have on photocurrent generation in photovoltaics. Starting with the routinely used textured surfaces, back reflectors and anti-reflective coatings. The introduction of light trapping structures can have even greater impact in thin film photovoltaics, where the shorter optical path length makes light trapping an attractive tool for increasing efficiencies. A broad number of micro and nanostructures are used to realise light trapping in these devices, including arrays of pillars, cones and nanowires.

With the DSSC being another example of thin film solar cell technology light trapping is of course equally important here, albeit with some other important considerations which must be taken into account, such as maintaining a high surface area in the $TiO_2$ layer for dye loading. Because of this light trapping strategies in DSSCs usually employ a hierarchical structure with nanoparticles of diameter 20nm for dye absorption, and larger nanoparticles or microstructures built from the smaller nanoparticles for light trapping. Here the template method is a popular tool for creating intricate 3D hierarchical structures, whereby a template or scaffold of polymer is used onto which nanoparticle structures can be built before the selective removal of the template. Some researchers have taken even more novel approaches, such as the copying or directly implementing light trapping structures from the biological world, where light trapping or scattering is common. Such as in butterfly wings or the single celled algae known as diatoms which have both been used for the fabrication of DSSC devices. Modelling light trapping in DSSCs can help to give researchers direction when working to improve light trapping, however these reports are generally limited by the traditional fabrication methods they envisage being employed to realise their structures. This chapter as also shown the great ability of SPCM for the characterisation of light trapping structures in both Si p-n junction solar cells and DSSCs.

To conclude light trapping is a valuable tool for increasing efficiencies in DSSCs, however there is room for further investigation into both finding optimal light trapping structures as well for developing methods for their fabrication. One potential method for the fabrication of a wide range of structures is by utilising the novel 3D printing technology TPP, which will be further discussed in the next chapter.

# Chapter 4

# 3D Printing of Submicron Structures

## 4.1 Introduction

3D printing (often also referred to as additive manufacturing) refers to the technique, or techniques, of fabricating a three dimensional physical object from a digital model, typically by applying the material in a layer by layer process. The advantage of these techniques over conventional manufacturing processes is that any shape or geometry that can be designed using a computer can be fabricated. There are many different types of 3D printing techniques. Such as materials jetting, similar to 2D ink-jet printing but fabricating materials layer by layer to create 3D objects. Power bed fusion whereby a laser is used to fuse a powered material together. And most relevant to this work by using a photopolymerisation technique, where a liquid photopolymer resin is cured or hardened using a UV (or other) light source which drives polymerisation. Additive manufacturing is already widely used in the industry for the printing of electronics [143]. The 3D printing of optics and optoelectronics are both areas in which interest from the research community is growing rapidly [144]. However the use of these techniques for the fabrication of structures or devices on the micron or sub-micron scale is still relatively new.

There is a growing need for 3D micro and nano fabrication techniques for applications in numerous fields including photonics, optics, electronics and the life sciences [145]. There are a number of different techniques that are used for fabricating 3D microstructures, these include; modified lithographic processes such as grey-scale lithography and moving mask lithography, laser induced chemical deposition and focused ion beam processing.

The novel 3D printing technique two-photon polymerisation (TPP) also allows the fabrication of micron and sub micron structures. However unlike these other techniques TPP allows a high degree of control to be introduced to the fabrication process. With the manufacture of 3D structures of almost any arbitrary shape and complexity being possible. This technology exploits the two-photon absorption process whereby an electronic transition in a material is driven by the collective action of two photons in combination. Since two photons must be present simultaneously, the probability for TPP depends non-linearly on light intensity. Therefore by focusing a laser beam, it is possible to create a situation where there is sufficient intensity to drive the TPP process but only within the focal volume of the laser beam [146]. Now light driven chemical and physical transformations can be effected within this volume and fabrication can approach the nanoscale [147].

## 4.2 Background and operating principles of TPP

### 4.2.1 Optics

Optical imaging systems are limited by a fundamental maximum resolution due to diffraction. In optical instruments light is focused through a lens, this lens acts to focus light but it also acts as a circular aperture and diffracts light. A circular aperture produces a diffraction pattern with a bright central maximum surrounded by dimmer circular fringes. Thus focusing parallel light rays through a lens will not lead to a perfect point but, instead this circular diffraction pattern. The resolution of an instrument is proportional to the wavelength of light ($\lambda$) and inversely proportional of the diameter of the lens (D). In a circular diffraction pattern the angular radius of the first minimum is $\theta_1 = 1.22\lambda/D$. In imaging two adjacent points in the object lead to two diffraction patterns. If the separation angle of these two points is less than the angular radius of the first minimum then the two points cannot be resolved in the resulting image, and the instrument is diffraction limited.

The limits of focusing of a laser beam are very similar to the focusing of light from a distant object in a telescope or through a microscope. The only difference here is that laser light generally has a Gaussian distribution, seen in figure 4.2. This non-uniformity leads to a coefficient slightly different from 1.22 value above. A Gaussian beam is a light beam which has an intensity profile which is given by the Gaussian function. The shape of the Gaussian beam is given by its beam-waist, this is the location along a focused laser beam where the beam radius is at a minimum and can be seen in figure 4.1. When a laser beam is focused to a spot by a microscope objective, the radius of the spot at the focus (at distance z) is given by

$$W(z) = \lambda f / \pi W_E \tag{4.1}$$

where $\lambda$ is the wavelength of the laser beam, $f$ is the focal length of the objective lens and $W_E$ is the beam waist radius at the laser exit aperture. Other properties of the Gaussian beam such as the Rayleigh range and the beam divergence can be determined from the beam waist. The Rayleigh range ($Z_R$) refers to the distance from the beam waist where the width of the beam is $\sqrt{2}$ larger than the beam waist.

### 4.2.2 Two-photon absorption

Two-photon absorption (TPA) was first predicated by Maria Göppert-Mayer in 1931 [148]. However, due to the high intensities required it was not demonstrated experimentally until 1961, after the invention of the laser [149]. The basic requirement for multi photon absorption is that an absorption event is caused by the collective action of two or more photons (figure 4.3a). These photons must be present simultaneously to impart enough energy to drive an electronic transition. It can be seen intuitively that this transition will be a non-linear process and proportional to the square of the intensity on incident light, since it requires two

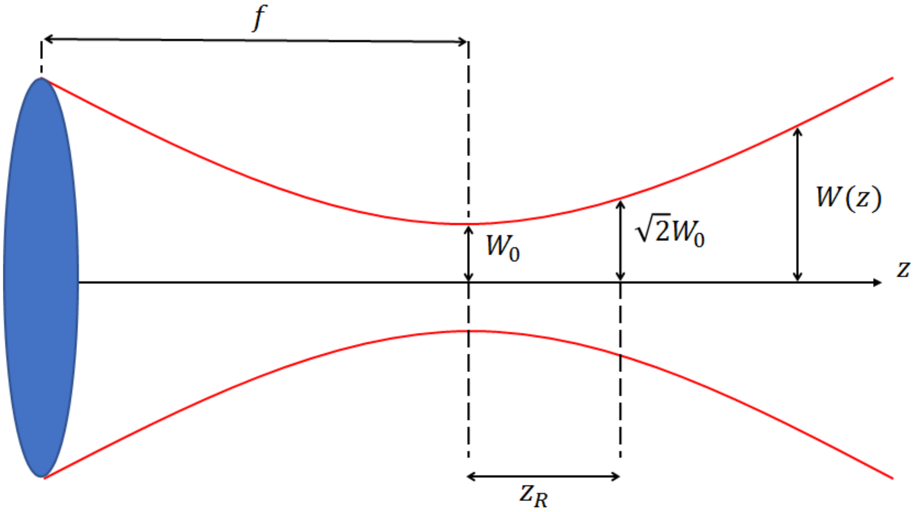

Figure 4.1: Diagram showing propagation of a Gaussian beam from a focusing lens. Where $W_0$ is the beam waist radius, $W(z)$ is the beam radius and $Z_R$ is the Rayleigh range.

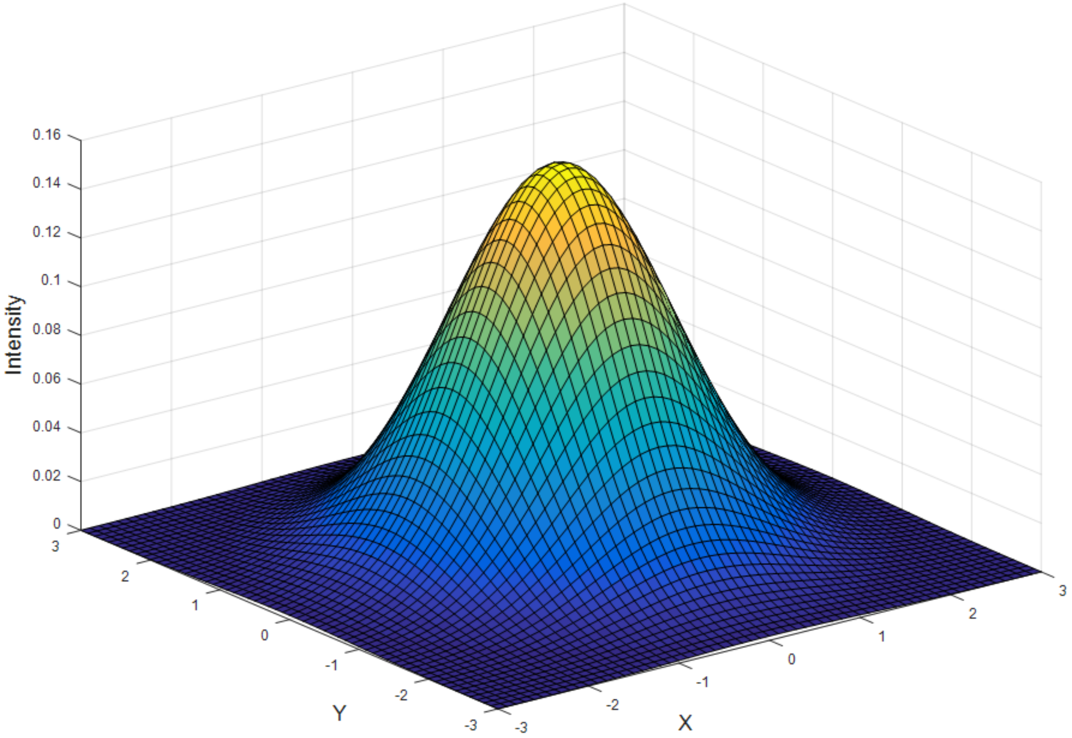

Figure 4.2: Intensity distribution of a Gaussian beam.

photons to arrive at exactly the same time and place, with higher intensities the likelihood of this event taking place increases.

The high intensity requirements and the non-linearity of the absorption process allows the excitation to be localised within the volume of a focal point of a laser. Due to the non-linear Gaussian distribution of the beam the laser power can adjusted so the absorption process only occurs at the centre of this intensity profile, in a focal volume that is smaller than the beam waist of the laser and thus smaller than the diffraction limit, depicted in figure 4.3b. The rate of absorption in a transverse cross-section of laser beam is proportional to the intensity squared times the number of molecules in the cross section. Therefore the greatest density of excited molecules will be in the region where the laser is focused most tightly. This localisation was first utilised in 1990 by Denk *et al.* in two-photon florescence microscopy [150]. Since this work, TPA has been studied intensively due to its potential application in a wide range of technologies such as florescence imaging, data storage and microfabrication [151]. Most commonly applications use high-peak power pulsed strongly focused sub-micron laser spot approaching the diffraction limit to achieve the required photon density for absorption. Typically femtosecond lasers are used to drive TPA. A common ultrafast laser used is a Ti:sapphire laser, which produces pulses that are a few tens of femtoseconds in duration with an inter pulse separation of about 12ns (corresponding to approximately 80MHz). Because of this the instantaneous energy during a pulse is high, which is favourable for TPA, however the average power remains low allowing for an efficient process. How this absorption process is manipulated for the polymerisation of photoresist materials and the spatial resolutions that can be achieved will be discussed in more detail below.

### 4.2.3 Two-photon polymerisation

In TPP the laser excitation drives absorption in the sample material which in turn drives a photochemical or photophysical transformation allowing polymerisation of a photoresist liquid resin to occur within the focal volume of the laser [145]. The laser is scanned to expose a material one volume element at a time allowing for an unprecedented level of 3D control. Once the prescribed pattern has been scanned, any unhardened material is removed by a development process (generally

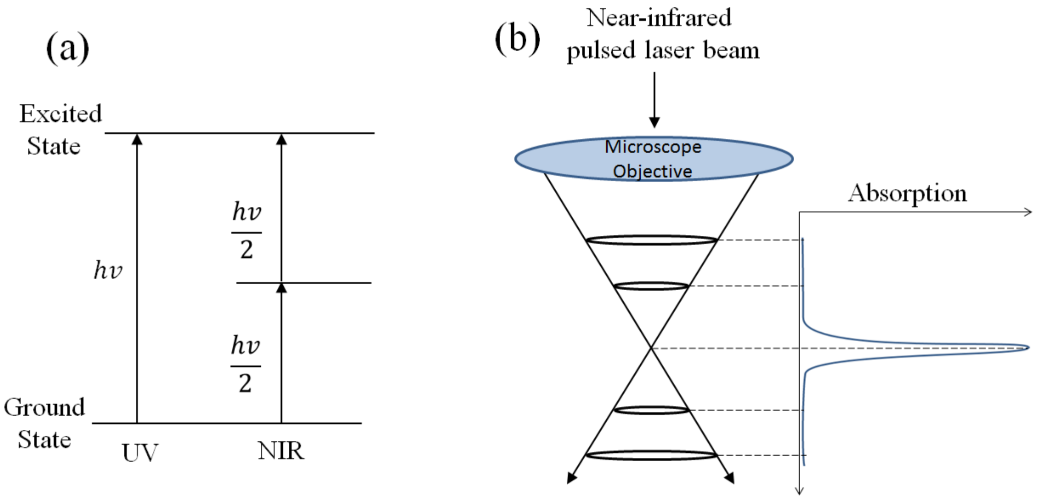

Figure 4.3: (a) Single and two photon absorption process. (b) Fundamentals of two-polymerisation by a focused laser beam.

washing or baking) revealing the desired three-dimensional structure.

Photoresists are light sensitive materials that undergo a polymerisation process when light of a particular wavelength is absorbed. Ultra-violet (UV) sensitive photoresists are widely used in conventional photolithography, many of these materials undergo the same or similar reactions under TPA with light of approximately half the energy in the near infra-red (NIR). Photoresists are multifunctional molecules which contain a photoinitiator, and monomers which are polymerised by a chain reaction following absorption. Incident light is absorbed by the photoinitiator which creates highly reactive free radicals or cations. When two of these molecules meet, they form a new covalent bond linking the two monomers.

### 4.2.4 Resolution

3D printing resolution describes the layer thickness in $Z$ and the $X-Y$ resolutions, the $X-Y$ resolution is generally slightly bigger than the thickness. Typical layer thickness for traditional 3D printing methods is around 100µm with the best commercial systems reaching $\sim$ 20µm. $X-Y$ resolution is typically around $50-100$µm with the best reaching $\sim$ 10µm [152]. For realisation of light trapping designs (and many other applications) microfabrication needs to go well beyond this limit as 3D light trapping structures could contain elements $\sim$ 1µm or less, approaching, or even going beyond the diffraction limit.

Resolution in TPP is defined as the smallest achievable feature size of the voxel, that is a 3D pixel, or one element volume which is polymerised. Since polymerisation is dependent on both laser power these parameters need to be well optimised to achieve the best resolution. The optical and chemical non-linearity of the TPP process means that by using this technique a resolution beyond that of the diffraction limit can be achieved, with structures being fabricated with a resolution of as small as 100nm [151]. The non-uniform Gaussian intensity distribution combined with the absorption processes dependence on the intensity squared mean that the laser intensity can be tuned so only the centre of the focused beam reaches the intensity required for continued chemical polymerisation to occur. Thus the voxel size can break the diffraction limit of the focused laser beam. Another parameter which can reduce the voxel size further is shrinkage that can occur in some photopolymer materials during post processing or development [153].

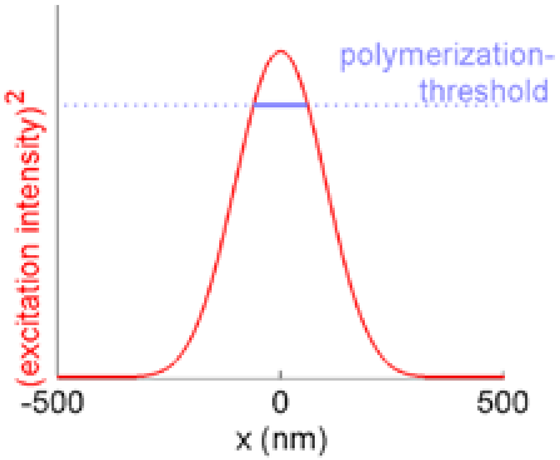

Figure 4.4: Graph showing laser intensity squared and polymerisation threshold.

## 4.3 Applications of TPP

### 4.3.1 Photonics and micro-optics

There are many current and potential applications enabled by the freedom and control of microfabrication given by the TPP technique. Among the most interesting, and certainly the most relevant here, is the manipulation of light in photonics and micro-optics.

Photonic crystals refer to periodic optical nanostructures which are able to affect electromagnetic wave propagation, similar to the way in which atomic lattices affect electrons in solids. These materials have been fabricated both directly and indirectly using a template method similar to that discussed for light trapping in DSSCs. Direct polymer photonic crystals with a spiral structure are easily fabricated using this method, whilst being immensely difficult to reproduce using traditional lithography techniques. These polymer photonic crystals exhibit photonic stop-gaps in the infra-red range and can be further modified and manipulated by the easy addition of controlled defects in the design [154]. Inverse silica photonic wood-pile have been fabricated by using a TPP technique to fabricate polymer templates which are subsequently filled with silica using chemical vapour deposition before the template is removed via calcination [155]. Figure 4.5a shows the resulting silica crystal and 4.5b shows the corresponding polymer template. Further work using this technique has also allowed the fabrication of gold helix broadband circular polarises [156], again this used template and infiltration technique with subsequent template removal, the resulting gold helix structures can be seen in figure 4.5c. TPP is also ideal for creating waveguide structures or components, many of which have already been realised, some examples are suspended waveguide structures in optical fibers, individual micro-lenses, linear couplers and Frensnel lenses [157, 158].

### Optical metamaterials

Optical metamaterials refer to a group of artificial materials with some remarkable optical properties that are not found in the nature [159]. Some of the fascinating optical properties these materials can exhibit are artificial magnetism, negative refractive index, negative refraction, and the materials can also be used to create superlenses (lenses which can go beyond the diffraction limit) [160]. These properties, unlike in nature, are dependent on the metamaterials carefully controlled internal structure and not solely the constituent chemical elements that make up the lattices of natural materials. The importance of the internal geometries of the material in producing these materials makes TPP an excellent tool for their fabrication [161]. An interesting example of a metamaterial fabricated using TPP is a microstructured metal surface which can switch from being a perfect reflector to a perfect absorber by changing the polarisation of the incident light [162]. This textured metamaterial surface can be seen in figure 4.6a.

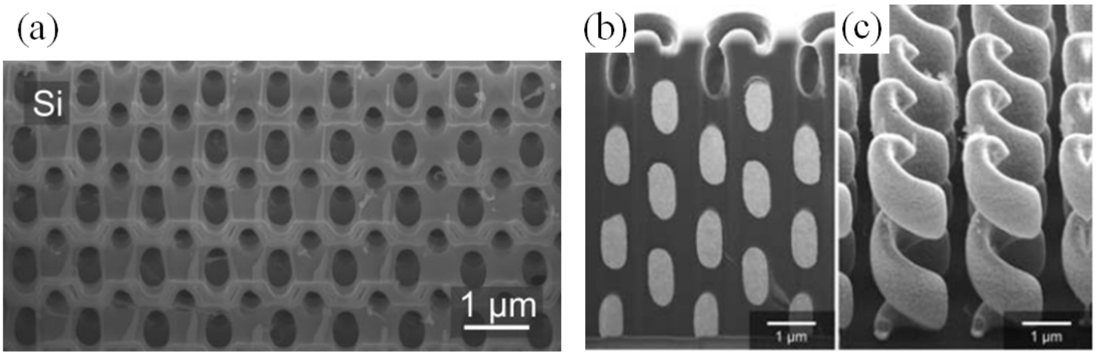

Figure 4.5: (a) SEM images showing inverse wood pile silica photonic crystal. (b) Corresponding polymer template. (c) Gold helix circular polariser structure. Adapted from [155, 156].

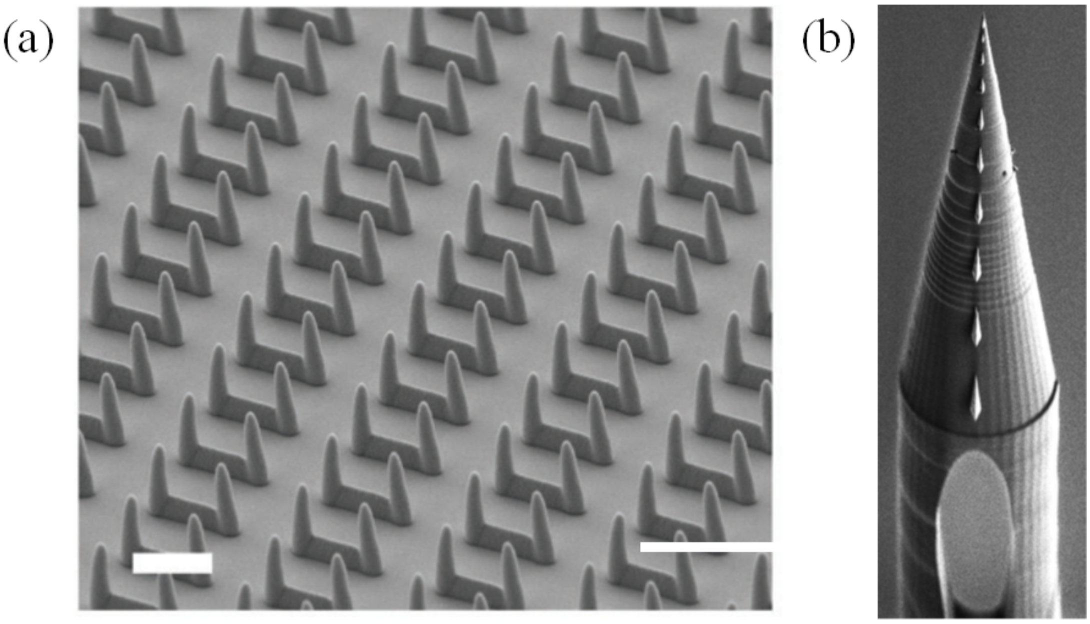

Figure 4.6: (a) Metamaterial surface that can switch between perfect reflector and absorber [162]. (b) Microneedle based on mosquito proboscis [163].

### 4.3.2 Other applications

#### Micron and nanoscale rapid prototyping

Rapid prototyping is a common application of 3D printing and other additive manufacturing techniques and refers to the quick fabrication of a working scale model or component part allowing for quick testing before large scale production. However as we have seen traditional 3D printing methods are limited in resolution, by using TPP fabrication methods rapid prototyping can be brought to a scale which was previously thought impossible. In relation to this work, many different types of light trapping structures using various designs can be made easily using TPP. These structures can then be integrated into solar cells tested experimentally and comparisons can be made to see which structures perform best. This is advantageous as there are many competing structural requirements in a DSSCs charge transfer layer which make it a very difficult and complex task to theoretically predict the ideal structure which will satisfy all of these requirements.

#### Mechanical microstructures

TPP can be used to fabricate a number of interesting mechanical microstructures. Mechanical metamaterials are structures where their mechanical properties are related to the structure and not just the composition of the material. TPP has been used to fabricate pentamode metamaterials, which are solids but still can have fluid like behaviour, that is to say they can be very difficult to compress yet still easy to deform giving them dynamic elastic properties [164]. Other mechanical metamaterial structures demonstrated with TPP are those which have negative Possions's ratio, meaning when stretched or compressed they become thicker perpendicular to the applied force [165] and could have applications as packing materials or for use in body armour. Other promising mechanically advantageous structures are ultralight microlattices, which have potential applications in thermal insulation, battery electrodes and as acoustic or shock damping and are easily fabricated using TPP [166].

### Microfluidics

Having such high control and resolution during fabrication, TPP is an obvious candidate for use in microfluidics, the field dealing with the precise control and manipulation of liquids at the sub-millimetre scale. The near arbitrary structures that can be fabricated using TPP give this technology a great advantage in this area. For example TPP has been used for the fabrication of microneedles which imitate the mosquito's proboscis and could have biomedical applications as this needle was shown to draw human blood by capillary action [163], this needle is shown in figure 4.6b. Another application is the fabrication of micro-nozzles for the precise control of liquid droplets, sprays or jets [167].

### Life sciences

There are a number of applications in the life science where TPP can have an impact. Some examples include swimming helical magnetic micromachines which spin and propel themselves forward under a rotating magnetic field, and are capable of performing micro-manipulation in 3D and could be used for targeted drug delivery [168]. Microneedles are another structure easily achieved with TPP and could also be used for drug delivery [169]. The fabrication of cell scaffolds allowing a significant amount of control in cell growth [170]. Finally TPP can be used in biomimetics for the accurate reproduction of useful structures found in nature such as highly adhesive materials based on gecko's feet [171], and low drag surfaces based on floating ferns [172] which have both been fabricated using TPP. Figure 4.7 shows some of the structures fabricated using TPP for some of the various applications mentioned.

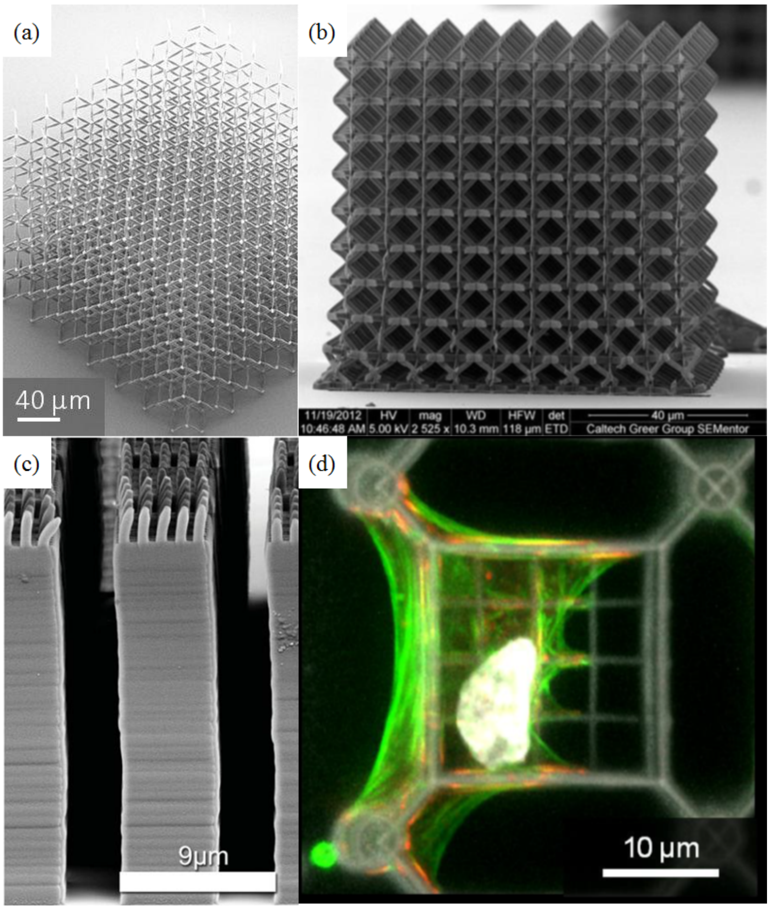

Figure 4.7: (a) Pentamode mechanical metamaterial. (b) Ultralight microlattice. (c) Biomimetic 'gecko' feet adhesive surface. (d) Cell and scaffold.

## 4.4 Summary and conclusions

This chapter introduces the microfabrication of polymers via TPP. This novel technique allows unprecedented control over fabrication approaching the nanoscale. The background of the technique and the physical mechanisms involved in the two-photon absorption and two-photon polymerisation processes are presented and discussed in detail to give the reader an overview its workings and development. Some time is spent considering the limitations of the resolution of the technique, which can go beyond the diffraction limit with feature sizes as small as 100nm, and how this is achieved.

The many and various applications of such fabrication methods are wide-ranging with it finding uses in areas such as photonics, optical metamaterials, rapid prototyping at the micro and nanoscale, mechanical microstructures and the life sciences. To conclude we propose the use of the TPP technique for the fabrication of polymer stamps and templates for patterning DSSC $TiO_2$ electrodes with light trapping structures to enhance photocurrent generation. Our experimental set-up for this system will be described, alongside the other research methods used in this work, in the following chapter.

# Chapter 5

# Research Methodologies

## 5.1 Introduction

This chapter will present a complete overview of the research methods used in this work. Starting with the methodology of the ray-tracing simulation used to investigate our light trapping structures performance across the solar spectrum. Next our characterisation techniques will be discussed, as some of these are used alongside the fabrication of our 3D printed light trapping $TiO_2$ electrodes it is natural that these techniques should be explored before our microfabrication methods.

Following this our structure fabrication will be described and discussed, where some of the characterisation techniques previously outlined will be used to chart the development of these processes and used to check final structure quality. First the design and microfabrication of the polymer stamps and templates used to patterned electrodes will be looked at, with a complete explanation of our experimental set-ups and the fabrication process from the software stage to the completed polymer structures. Next the patterning of the electrodes with these polymer structures will be explored again using some of these characterisation methods to chart the improvement and optimisation of this process. Finally DSSC assembly will be introduced, following the process from counter electrode preparation, to final cell assembly.

## 5.2 Ray-tracing simulations

We utilise ray tracing software (Tracepro Lambda Research Corporation) to determine the effectiveness of our light trapping designs at enhancing the performance of DSSCs. Using these methods we hope to evaluate their performance at increasing absorption at a single wavelength, over the AM 1.5 solar spectrum (seen in figure 2.4 and obtained from [173]), and their dependence on incident angle. We will also take a look at the how the structures design was adapted for practical reasons during fabrication and how these changes affect performance. Ray tracing is a powerful tool and widely used for the examination of optical systems. Including solar cells and DSSC devices where performance of a cell can be analysed using the comparison of metrics such as path-length enhancement, absorption, etc.

Ray-tracing generally uses a Monte-Carlo approach to simulation, where this method is used to characterise the scattering and diffraction of light upon striking a surface. Here a computer algorithm relies on repeated random sampling to obtain the result for a deterministic process, when this process is repeated a large number of times and the results are aggregated an accurate picture of the optical model can be simulated. The light ray incident on a given surface is distributed to random rays according to a probability distribution determined by the material properties (absorbance, reflectance, transmittance, refractive index), before moving onto to the next surface/interface. The larger the number of incident rays the more accurate the calculation will become, however it is a trade off between accuracy and computational time. Because of this it is necessary to perform a ray independence test, whereby the total number of rays is increased until the errors in the result of the simulation become insignificant.

### 5.2.1 DSSC Model description

A 3D ray-tracing model is developed for our light trapping designs which have been incorporated into a DSSC device. The device consists of a glass substrate with a transparent conducting FTO coating, $TiO_2$ active layer, electrolyte and finally another FTO coated conducting glass back contact. The glass substrate is 3mm (Pilkington, TEC15) the thickness of which has been found by previous work [115] to not affect absorption in the active layer and as such is set to $1\mu$m in the model to save computational time. The FTO coating is 500$\mu$m. The active layer of dyed $TiO_2$ follows which is 10$\mu$m thick (5$\mu$m pyramid structure on 5$\mu$m base). The areas in-between structures are considered to be pure electrolyte. The electrolyte layer is also set to 1$\mu$m in the interests of saving computational time [115]. All of these layers in are in contact i.e. no air gap between. Although in reality the glass, substrate, FTO and electrolyte all absorb some light for the purposes of this study we ignore these effects in all the simulations as we are only focused on the enhancement of absorption in the active later layer [174]. A schematic of the DSSC model can be seen in figure 5.1. The patterned array for side wall angle of 54.7$^o$ is 90$\mu$mx90$\mu$m with 10x10 pyramids the geometry and dimensions of which can be seen in figure 5.2. The structures also have a 1$\mu$m plateau at the pyramid apex and a 1$\mu$m gap between pyramids in the array. With this structure having the same geometry as those fabricated and implemented into our light trapping DSSCs. The choice of this light trapping design and its modifications will be discussed further later in the chapter.

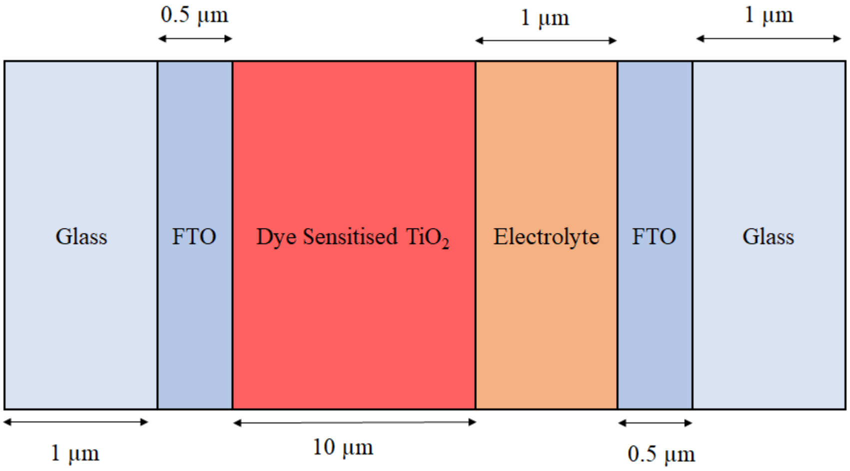

Figure 5.1: Schematic of DSSC device stack used as model.

In the control sample the thickness is calculated to reflect the same volume as the pyramid array, when this volume is redistributed into a planar geometry the thickness is 8.5$\mu$m for pyramid angle side walls of 54.7$^o$ and height 5$\mu$m. This ensures that absorption enhancement is due to light trapping rather than differences in the amount of active material. This approach is also taken when looking at pyramid arrays of differing geometries.

Materials properties are all obtained from experimental data in the literature, with

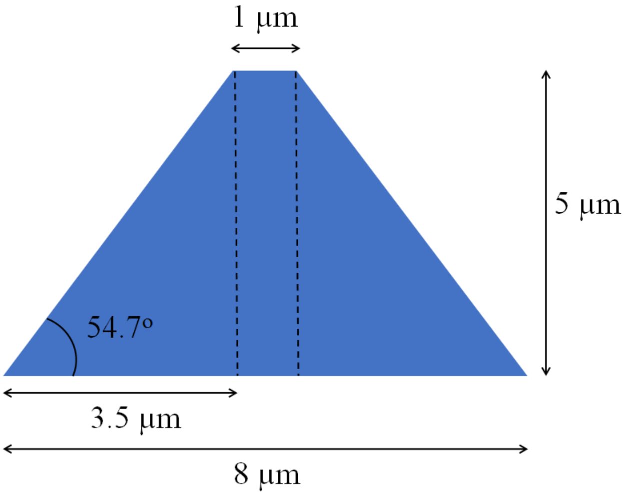

Figure 5.2: Geometry of pyramid with side wall angles of 54.7°

the values for the refractive index of the glass, FTO and $TiO_2$ provide by Ball et al. [175], the values for the refractive index of the electrolyte solvent by Kozma, *et al.* and Moutzouris, *et al.* [176, 177]. Absorption data for $TiO_2$ dyed with N719 (Ruthenizer 535-bisTBA, Solaronix) is provided by Ito *et al.* [178]. Incident rays with intensity of 1000W/m$^2$ at the average wavelength of solar radiation (540nm) are used for single wavelength studies. All light is incident at 0° except in angle dependence tests. The table below shows the properties of the materials used in the model at 540nm. Further simulations look at the absorption over the AM 1.5 solar spectrum (seen in figure 2.4) from 380-800nm. This is the region of high absorption for the dye N719 and the range with absorption data available in the literature. Next a number of variations on the structure used experimentally are studied, alongside further pyramid structures of differing side wall angles, for these studies the height of all the pyramids is keep constant at 5 $\mu$m.

| Material | Refractive index $n$ | Absorption Coefficient, $\alpha$ ($\mu$m$^-1$) |
|---|---|---|
| $TiO_2$ + N719 | 2.13 | 0.11 |
| FTO | 1.90 | 0 |
| Glass | 1.51 | 0 |
| Electrolyte | 1.34 | 0 |

For this model ray simulations are conducted using the commercial ray-tracing software Tracepro (Lambda Research Corporation), where rays that enter a material with no zero absorption transmit light according to the Beer-Lambert law,

$$\Phi_T = \Phi_0 e^{-\alpha t} \tag{5.1}$$

where $\Phi_T$ and $\Phi_0$ are the transmitted and incidence flux, $\alpha$ is the absorption coefficient and $t$ is the material thickness through which the ray has travelled. The flux absorbed by the material is then,

$$\Phi_A = \Phi_0(1 - e^{-\alpha t}) \tag{5.2}$$

From this, absorption in our DSSC light trapping devices can be simulated. Then the spectral photocurrent density and the maximum achievable photocurrent density (MAPD) can be calculated for over the AM 1.5 solar spectrum. The spectral photocurrent density is given by

$$J(\lambda, \theta) = \frac{e\lambda}{hc} I(\lambda) A(\lambda, \theta) \tag{5.3}$$

And the maximum achievable photocurrent density (MAPD) is is given by,

$$J_{\lambda_{min}}^{\lambda_{max}}(\theta) = \int_{\lambda_{min}}^{\lambda_{max}} \frac{e\lambda}{hc} I(\lambda) A(\lambda, \theta) d\lambda \tag{5.4}$$

Where $e$ is the electron charge, $h$ is planck's constant, and $c$ is the speed of light in a vacuum. $I(\lambda)$ is the AM 1.5 solar light intensity incident on the cell per unit wavelength of incident angle $\theta$. $A$ is the normalised absorption of the device, the relation $I(\lambda)A(\lambda, \theta)$ is divided by the photon energy to give $hc/\lambda$ to give the number of photons absorbed per second per unit area per unit wavelength. The MAPD assumes perfect charge collection whereby one absorbed photon results in one electric charge contributing to current (no losses through recombinations), and is obtained by multiplying by $e$ and integrating over relevant wavelengths. Because unfavourable electronic process are not considered here the actual short circuit current density will be less than the calculated MAPD.

Ray independence tests were conducted at 540nm for both the control and the pyramid patterned array. Figure 5.3 shows the ray independence test for the pyramid array at 540nm, with errors becoming negligible from 100,000 rays. Since simulations using 1000,000 rays did not result in excessive computation times this number was selected for further studies to ensure any computational errors were completely removed. The errors for the control become negligible at only 10,000 rays however further simulations were also conducted at 1000,000 for consistency.

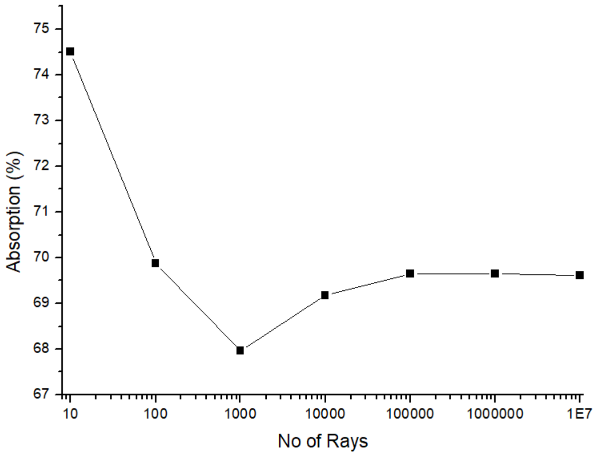

Figure 5.3: Ray-independence tests for pyramid array patterned $TiO_2$ electrode at 540nm.

## 5.3 Characterisation techniques

### 5.3.1 Optical and scanning electron microscopy

Stamps, patterned electrodes, and DSSC devices are characterised with both optical and scanning electron microscope (SEM) imaging. A SEM operates using the same basic principles as a visible light microscope, but uses electrons instead of photons. The resolution of a visible light microscope is limited by the wavelength of the photons being used to probe the sample (visible light 400-700nm). Since the de Broglie wavelength of electrons can be much smaller than that of visible light, electrons can be used to obtain resolution approximately one thousand times better. This vast difference in resolution makes the SEM a valuable tool.

Unlike photons electrons are charged particles so there are inevitably a few differences in a SEM to an optical microscope. A SEM system must be in vacuum or electrons will interact with charged molecules in the air. Also, as electrons cannot pass through glass, conventional lenses cannot be used in SEM. Therefore magnets are used as lenses and, by changing the strength of the magnetic field, the electron beam can be manipulated and the image can be magnified. Since electrons cannot be seen by the naked eye as in a visible light microscope, the image is magnified and focused onto an imaging device such as a CCD camera. Sometimes contrast must be provided by using electron-absorbing heavy metals to stain the samples.

In this work SEM images were taken using the Hitachi, Tabletop TM3030, with polymer stamps being sputter coated with a layer of platinum or gold. Sputter coating refers to the deposition of a thin layer of conducting material onto a non-conducting sample, such as the polymers used here in stamp fabrication via TPP. This layer is employed to prevent the charging of the sample by the electron beam which leads to a distortion of the image. It is worth noting that these metals cannot be easily selectively removed from the $TiO_2$ electrode after patterning. Therefore stamps that had been selected for characterisation with SEM are not used for electrode patterning. The TM3030 can also help to overcome this problem with charge-up reduction mode. This mode uses low-vacuum functionality to dissipate the charge build up on the sample. Stamps that are used for electrode patterning are checked for quality with an optical microscope which still has sufficient resolution for quality assurance purposes.

### 5.3.2 Energy-dispersive X-ray spectroscopy

Patterned $TiO_2$ electrodes are characterised with SEM and optical microscopy, further elemental analysis is also carried out with energy dispersive X-ray spectroscopy (EDX). This is utilised to ensure that all organic material and other contaminates are removed from the electrode after patterning is complete. EDX is a powerful non-destructive technique used to identify the elemental composition of a material. The technique makes use of the X-ray spectrum emitted by individual atoms, which are being bombarded by an electron beam [179].

EDX uses a high energy electron beam to stimulate emission of characteristic X-rays from different atoms present in the exposed (usually very small) area of the sample. The incident beam excites an electron from an inner shell to an outer shell creating a hole in the process. Now an electron from the outer shell fills this hole and an X-ray is emitted from the atom with energy equal to that of the transition between the two shells [179]. Each element has a unique atomic structure leading to a characteristic X-ray spectrum. Thereby detailed analysis of the elemental composition of a solid material is made possible if one can identify X-ray energy peaks created by different elements. Figure 5.4 shows an example of a EDX spectra of a $TiO_2$ surface, where the two elemental components peaks of titanium and oxygen are highlighted. In this work EDX analysis was conducted with the Hitachi, Tabletop TM3030.

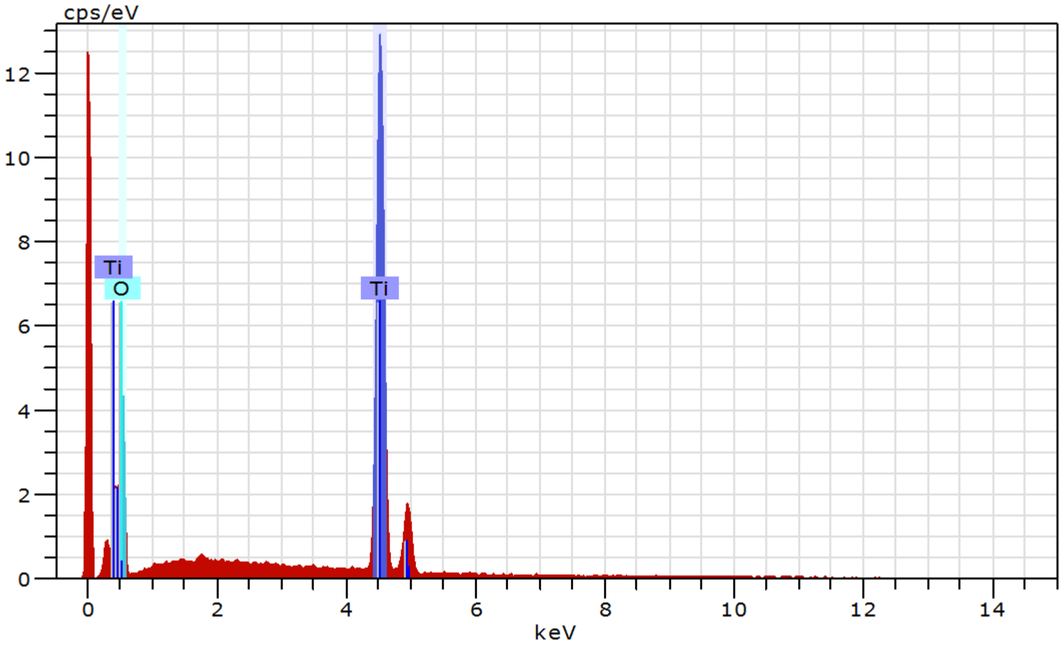

Figure 5.4: EDX Spectra taken from $TiO_2$ surface, with titanium and oxygen peaks highlighted.

### 5.3.3 Traditional characterisation of solar cells

Solar cells, including DSSCs, are typically tested for performance by looking at the current voltage ($J - V$) characteristics of the entire cell. Two fundamental measurements are the overall solar-to-electrical conversion efficiency, $\eta$, and the incident photon to current conversion efficiency (IPCE). This can give us an overview of how the cell performs over the solar spectrum and how the cells perform at specific wavelengths. For these tests cells are illuminated with a solar simulator where $P = 1000\,\mathrm{W/m^2}$. Whilst this type of analysis is excellent for exploring the characteristics of a whole cell, it is not necessarily the best for analysing the light trapping structures fabricated in this work. This section will briefly explain these traditional characterisation methods in some more detail.

$J - V$ characteristics are obtained by sweeping from the open circuit voltage to $V = 0$ under simulated solar irradiation. The overall solar-to-electrical conversion efficiency, $\eta$, for a solar cell is given by the photocurrent density measured at short-circuit ($J_{sc}$), the open-circuit photovoltage ($V_{oc}$), the fill factor of the cell (FF) and the intensity of the incident light ($P_{in}$) according to

$$\eta = \frac{J_{sc}V_{oc}\mathrm{FF}}{P_{in}} \tag{5.5}$$

The fill factor can assume values between 0 and 1 and is defined by the ratio of the maximum power available ($P_{max}$) to the solar cell per unit area divided by the $V_{oc}$ and $J_{sc}$ according to

$$\mathrm{FF} = \frac{P_{max}}{J_{sc}V_{oc}} \tag{5.6}$$

The maximum power is obtained as the product of the photocurrent and photovoltage at the voltage where the power output of the cell is maximal. Another important measurement of the performance of a solar cell is the incident photon to current conversion efficiency (IPCE). The IPCE value corresponds to the photocurrent density produced in the external circuit under monochromatic illumination of the cell divided by the photon flux that strikes the cell. From such an experiment the IPCE as a function of wavelength can be calculated from

$$\mathrm{IPCE} = \frac{J_{sc}(\lambda)}{e\Phi(\lambda)} = 1240\frac{J_{sc}(\lambda)[\mathrm{Acm^{-2}}]}{\lambda[\mathrm{nm}]P_{in}(\lambda)[\mathrm{Wcm^{-2}}]} \tag{5.7}$$

where $e$ is the elementary charge, $\Phi$ is the photon flux and $\lambda$ is the photon wavelength. IPCE values provide practical information about the monochromatic quantum efficiencies of solar cells.

Whilst these methods are excellent for the characterisation of whole cells they are not appropriate for the smaller scale characterisation of the light trapping patterned areas of DSSC electrodes presented in this work. A more suitable characterisation method for our purposes will be described next.

### 5.3.4 Scanning photocurrent microscopy

#### Early photocurrent mapping experiments

Early current mapping experiments were conducted on a Horiba Jobin Yuon Ltd.(HR800) Lab. Ram. This is an integrated system designed for Raman spectroscopy and micro-photoluminescence studies. The system comes equipped with a He-Ne laser ($\lambda = 633\,\text{nm}$) with a power at the source of up to 14mW. In addition, the system has been modified to include a diode-pumped solid state laser ($\lambda = 532\,\text{nm}$) with power at the source of up to 300mW. The laser beams reach the sample through a microscope fitted with 3 objectives, x10, x50 and x100, corresponding to a spot diameter ranging from $\sim 0.5 - 5$µm. The system also comes equipped with a computer controlled XYZ stage with $\sim$ 100nm resolution. Figure 5.5 shows a schematic diagram of the experimental set up used in this experiment.

Figure 5.6 shows some preliminary photocurrent mapping results, here the current was measured under short circuit conditions with a 532nm solid state laser used to excite a conventional planar DSSC sample. The laser intensity was adjusted to give the best resolution through the conducting glass substrate, this was $\sim$ 3µm in diameter. In these, and all following, results the glass of the solar cells is 3mm. The thickness of this glass leads to significant degradation of the focusing potential of the objective due to aberration which leads to this $\sim$ 3µm laser spot size. The map was produced of an area of 20µm$^2$ with measurements taken every $\sim$ 2µm so there is some overlap of the laser spot with individual measurements. The sample was tested to find the area with the best response, this was then selected for the experiment. The map shown in Figure 5.6 gives a good visual representation of the changes in response across a specific area of the cell. These results show that in a cell where the $TiO_2$ nanoparticles are orientated in a random fashion, there can still be significant changes in local efficiencies.

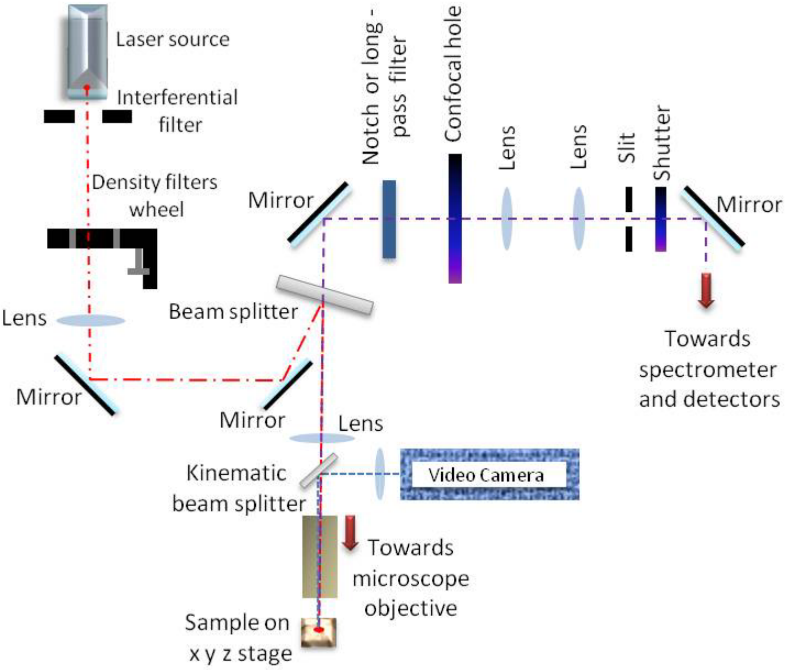

Figure 5.5: Schematic of experimental set up used for micro-PL studies and early SPCM measurements.

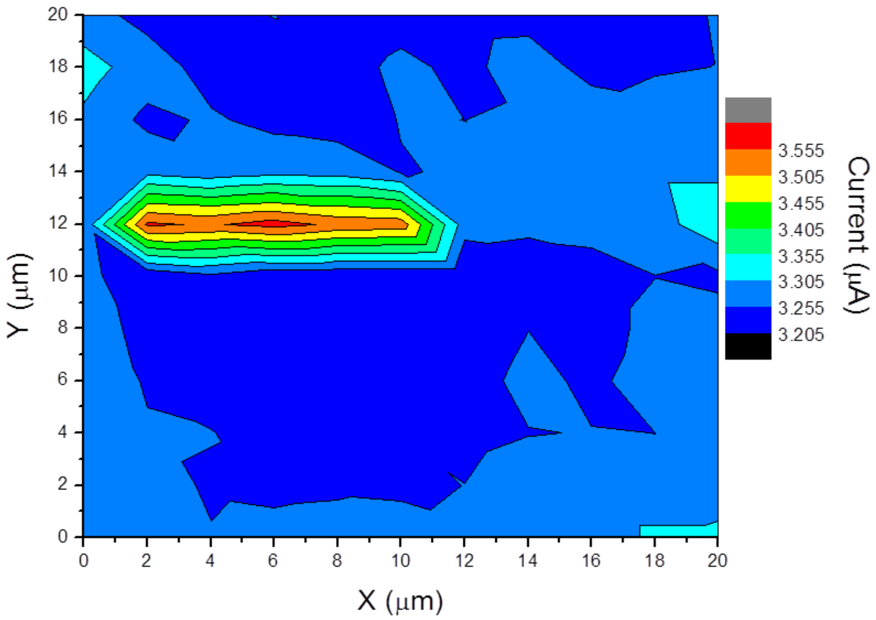

Figure 5.6: Photocurrent map of preselected area of cell.

### Purpose built SPCM

Our custom built system was developed to improve upon the SPCM technique. Unless otherwise stated in the text results in this work were obtained using this custom built system. In this system measurements were performed using a focused laser beam ($\lambda = 405$nm) onto a sample mounted on an XY-combination of two hybrid piezo-motorised XY-translation stages M-511. HD (PI Instruments) providing XY-translation up to 10cm with precision < 10nm. Electrical current was recorded as a function of the position of the laser spot on the sample. Spatial resolution of our SPCM set-up can be adjusted between < 1μm and 1mm by the diameter of the focussed laser spot using x5, x10, x20, x50 and x100 microscope objectives, a 1mm spot diameter is possible if you use an empty hole instead of an objective. Figure 3.18a shows a schematic of the SPCM, the system is also equipped with a visible light source and microscope. This optical imaging of the same areas as the SPCM measurements allows the overlay of images and direct comparison of the two characterisation techniques. Samples are fixed in place with a sample holder, designed to the purpose of holding our DSSCs, the holder is then fixed to the stage. Figure 5.7b shows a corresponding optical image of the SPCM experimental set-up.

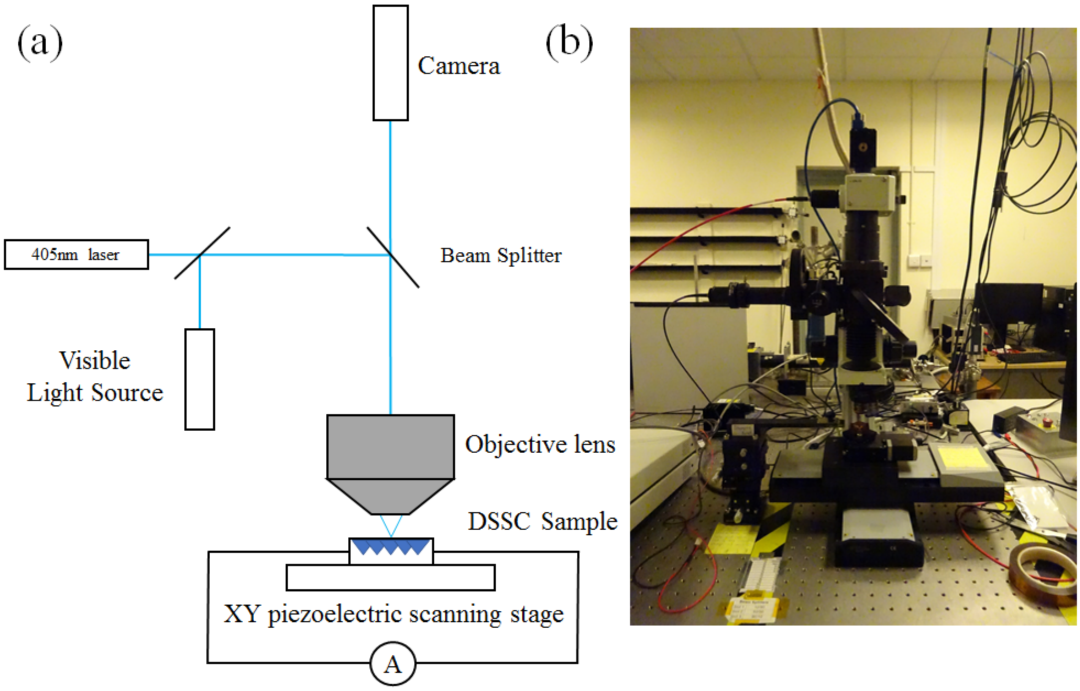

Figure 5.7: (a) Schematic of SPCM set-up. (b) Corresponding optical image.

### Data Analysis

Our scanning photocurrent microscopy technique generates photocurrent contour maps as seen in figure 5.6. When our planar and light trapping DSSC are characterised using this technique we use a number of statistical methods to analyse the data collected in these maps. First we will use the standard deviation ($s$) of the mean to quantify the variability or scatter in our data over a selected area or over the whole photocurrent map. This quantity is given by

$$s = \sqrt{\frac{1}{N-1}\sum_{i=1}^{N}(x_i - \bar{x})^2} \tag{5.8}$$

where $\bar{x}$ is the mean and $N$ is the number of data points. Another useful quantity is the standard error of the mean (SE) which quantifies the precision of the mean of our data. This value is a measure of how far our mean value deviates from the population mean. It is an important value as it enables us determine the 95% confidence interval (CI) of the mean. The SE is given by

$$SE = \frac{s}{\sqrt{N}} \tag{5.9}$$

The CI is another measure of how precisely the mean has been determined or put another way is the range that we expect, with some level of confidence, in our case 95%, to include the actual value of mean. CI can be calcualted for any degree of confidence, however 95% CIs are most commonly used and will also be used here. the 95% of the mean is given by

$$95\%\text{CI} = \bar{x} \pm Z \cdot SE \tag{5.10}$$

Where $Z$ (standardized score) is the value of the standard normal distribution with the specific level of confidence. For a 95% CI Z = 1.96. CIs are a general concept and the 95% CI of the difference of two group means can also be calcualted. The CI for the difference of two means specifies a range of values within which the difference between the means may lie. And is useful when determining whether this difference is significant. When comparing two means the basic null hypothesis is that the means of the two groups are equal, that is to say, if the 95% CI of the difference contains zero. If the 95% CI does not contain zero then the null hypotheses can be rejected. Since the CI in the results analysed in the following chapter only use a 95% CI it will be shortened and referred to as only CI. The 95% CI of the difference between two means $(\bar{x_1} - \bar{x_2})$ is given by

$$(\bar{x_1} - \bar{x_2}) \pm Z\sqrt{\frac{s_1^2}{N_1} + \frac{s_2^2}{N_2}} \tag{5.11}$$

In the SPCM results presented in the following chapter means will be presented with the descriptive statistics of standard deviation and number of data points in the format, Mean ($s$ = standard deviation, N=number of data points) i.e. 50nA ($s$ =5nA, $N = 100$). When light trapping and planar background regions are being compared to quantify photocurrent enhancement the 95% CI will be presented in the format, Difference in mean (CI = lower limit, upper limit) i.e. 5nA (CI = 2.5nA, 7.5nA).

## 5.4 Microfabrication of Polymer Stamps and Templates for DSSCs

This section will describe the fabrication processes of the 3D polymer stamps and templates using the TPP. First it will present the our TPP system set ups, then structure design at the software stage (including our final light trapping design used) will be tackled before moving on to lay out the physical fabrication processes, including structure post processing, with all the associated technical details. Whilst the description of this fabrication process will focus of the photoresist IP-L it will also describe the changes in the fabrication process when using the other materials such as, SU-8 and Omocers. Finally characterisation of the fabricated stamps and templates will be presented, compared and their development and optimisation discussed. This section aims to showcase the versatility of the TPP system in the fabrication of a large range of differing 3D designs on the micron scale, perfect for our requirements, but also applicable in many other fields and applications which require this high degree of control during microfabrication.

### 5.4.1 Two-Photon Polymerisation System Set-up

Microstructure fabrication was conducted on two different systems, both a custom build, in house system and the commercial Nanoscribe Photonic Professional system [180]. With the bulk of the work being done on the Nanoscribe system due to the faster fabrication rates which can be achieved. Since both systems are similar and most of the work in this report was done with the Nanoscribe system, this section will focus on the description of the experimental set-up of the Nanoscribe system with some additional comment on the custom system. Both systems are installed on optical tables to reduce vibrations. All fabrication experiments are conducted in the absence of UV light which would act to polymerise the photoresist materials used and are also conducted in ambient pressure conditions at room temperature.

#### Nanoscribe Photonic Professional

The Nanoscribe system uses a 780nm Ti-Sapphire femtosecond laser with a pulse length of 150fs at 100MHz with a pulse power of 100mW, which translates to approximately 20mW at the surface of the sample. The laser light passes through an acousto-optic modulator, a polariser to control power and a beam expander before reaching an inverted microscope, see figure 5.8. The system is installed with an inverted Carl Zeiss Axio Observer microscope which, for the purposes of these experiments was fitted with a 100x 1.4NA oil immersion objective and also contains a live camera, auto-focusing system and transmission and reflection illumination LEDs. In these experiments the system was operated in transmission mode whereby the laser light is focused through the objective into the oil, then passes through the substrate and into the photoresist material. In other words the structure is fabricated bottom up with the laser light passing though the substrate via an inverted optical set-up. Figure 5.9 shows the schematic of both this transmission set up and the alternative 'dip-in' set up where the objective is immersed into the photoresist directly, this mode allows for taller structures

(> 300µm) to be fabricated but is limited in materials that can be used. ’Tall’ structures were not required for these experiments where the optimal size for the charge transfer layer in DSSCs is approximately 10 – 15µm. All experiments presented in this work were conducted in transmission mode.

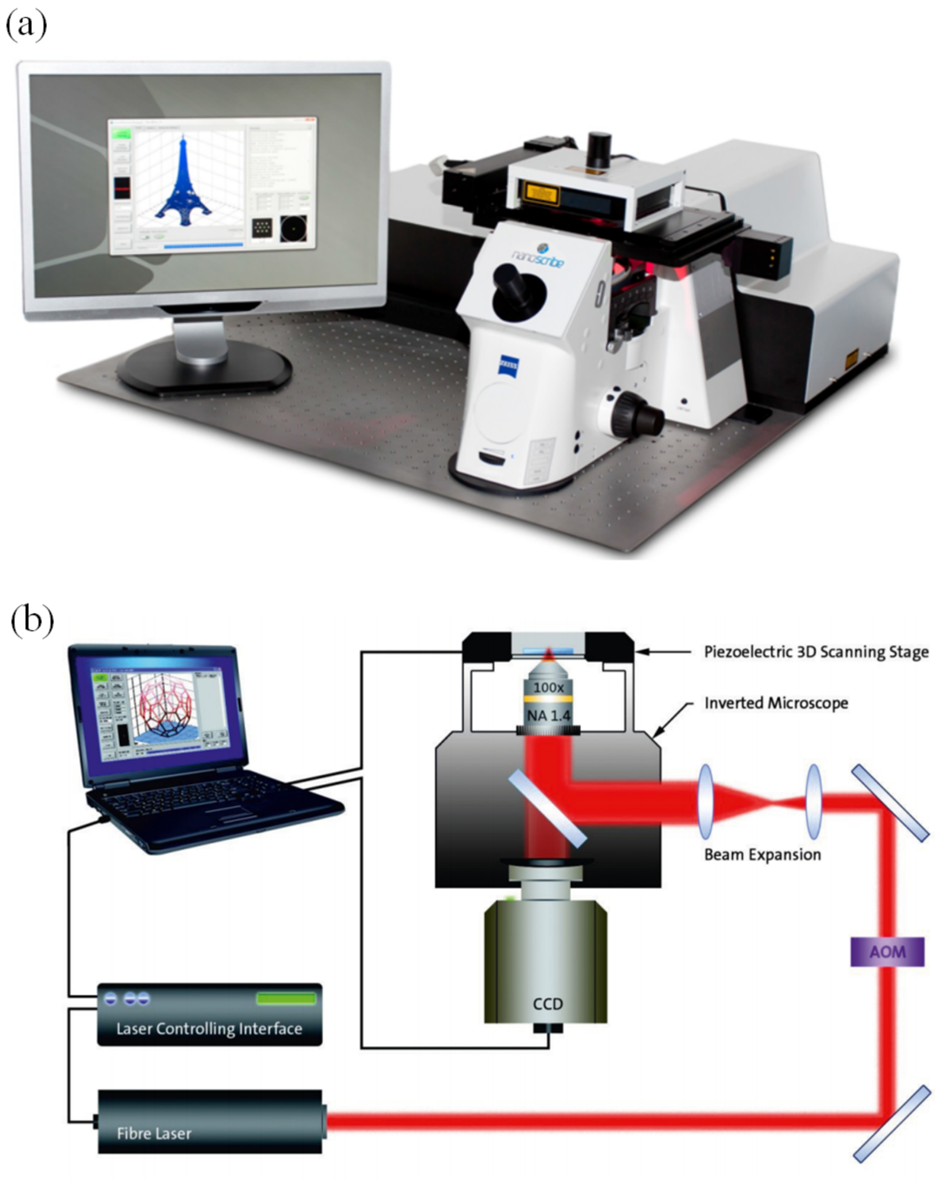

Figure 5.8: (a) Optical image of Nanoscribe Photonic Professional system. (b) Schematic diagram of Nanoscribe Photonic Professional set-up [180].

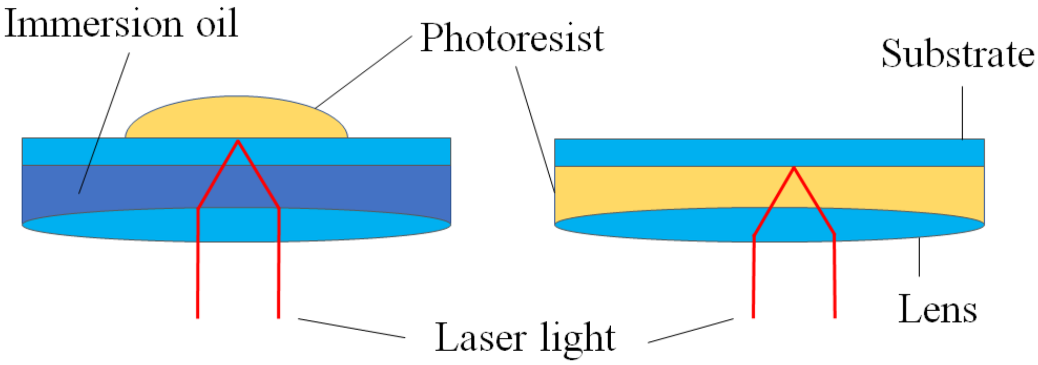

Figure 5.9: Diagram showing writing modes in Nanoscribe TPP system.

### Focusing to interface

The Carl Zeiss Axio Observer microscope system comes with an autofocus system which allow easy focusing to the oil/substrate interface. This works via the projection of a grid pattern using an infrared LED, this pattern is reflected back onto a camera chip which is positioned an angle. Due to the angle of the chip only a small area of this grid is well focused when the objective is focused onto the interface. If the objective focus is moved away then the relative position of the grid projection to the camera chip changes. The auto focus system controls the microscope's z-drive and corrects the position until the grid area is again sharply detected on the camera chip. A schematic of this autofocus system can be seen in figure 5.10.

### Stages and scanning methods

The system contains both a motorised coarse positioning stage and a piezoelectric stage for fine positioning and scanning. The piezoelectric stage has a range of $300\mu m^2$ and an accuracy of $< 10nm$, since this is beyond the fabrication resolution of the system due to optical reasons it is more than sufficient. Fabrication can be done using two laser writing or scanning modes, piezo-scanning and galvo-scanning. Galvanometer scanners use precise positioning of two mirrors to deflect the laser beam quickly and accurately. Using this mode for scanning in two photon polymerisation allows the rapid fabrication of structures with writing speeds in the

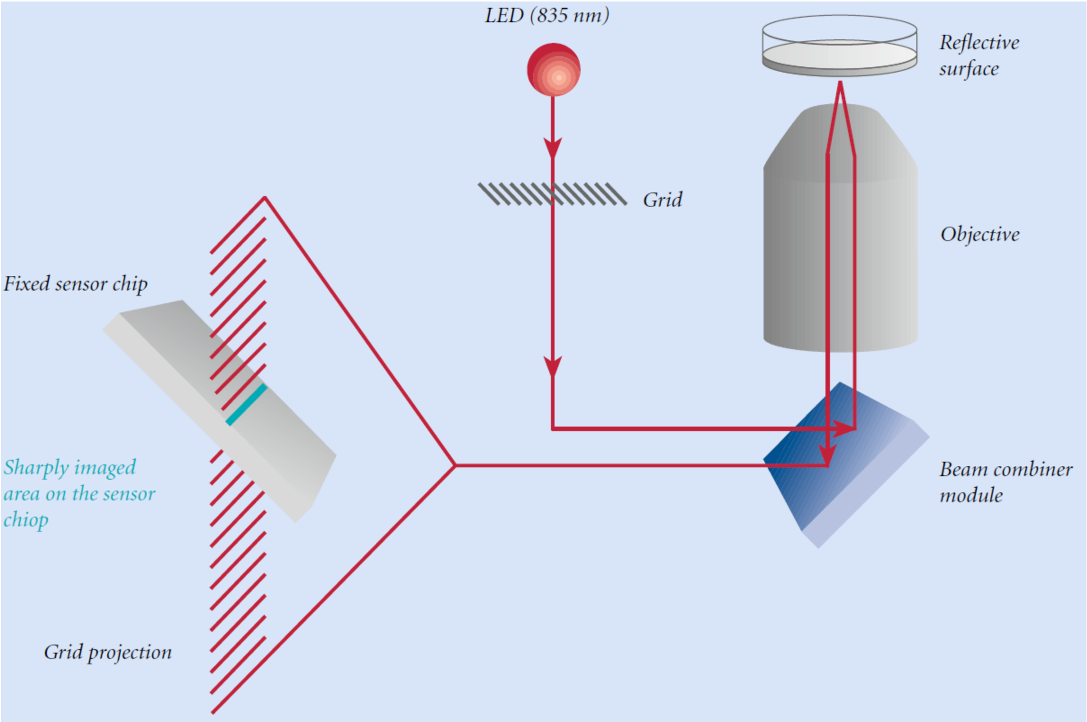

Figure 5.10: Zeiss Axio Observer microscope autofocus system [181].

range of mm/s, however these scanners only have an accuracy of approximately 10µm. The galvo system used here cannot write in Z, the laser is scanned across an x-y 'slice' of the desired structure before being moved in z by the piezoelectric stage and the next slice is scanned. For the precise control needed to fabricate light trapping structures piezo-scanning is required, which has writing speeds in the range of µm/s, however much greater control and resolution (x-y∼ 150nm and z∼ 1µm) is possible. This slow fabrication speed is one of the limitations of two-photon polymerisation technique and means that scaling up this technology is challenging, but it does allow for the rapid prototyping and testing of structures with unprecedented control and resolution. For this work the piezo-scanning mode is predominantly used throughout although galvo-scanning was sometimes used for calibration and materials testing.

### Custom TPP system

The custom TPP system operates in essentially the same manner as the Nanoscribe system, however the light is incident from above into the photoresist resin. Like the

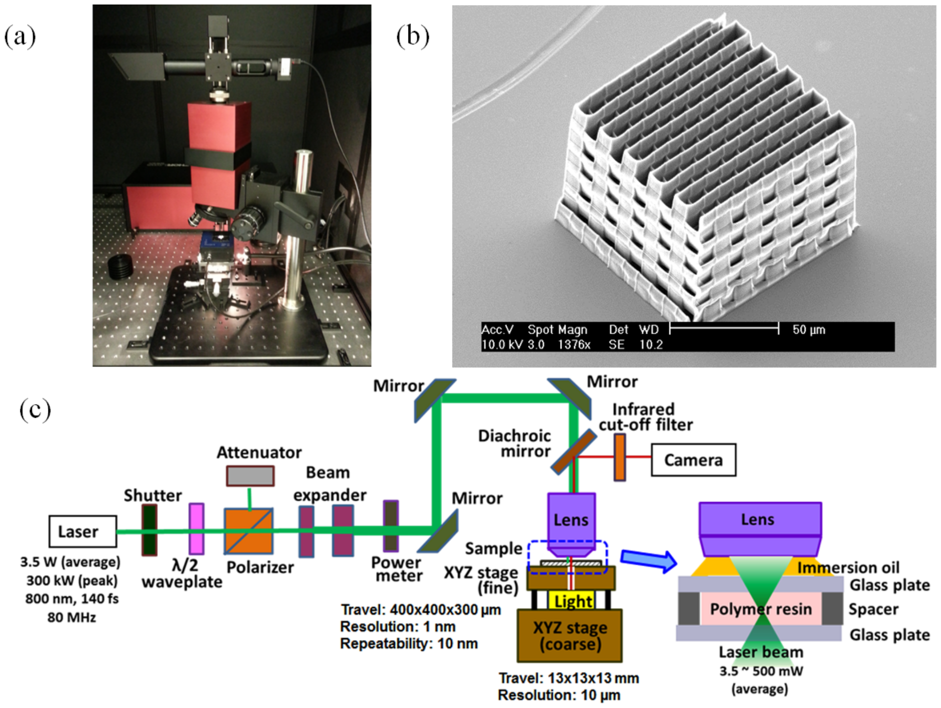

Figure 5.11: (a) Image of custom TPP system. (b) SEM image of woodpile structure fabricated with Ormocers photoresist. (c) Schematic diagram of custom system.

Nanoscribe system, the structures are fabricated from the bottom up but here the light does not pass through the substrate but through the immersion oil and glass cover slip before entering the photoresist. The inverse configuration is considered slightly preferable since the light has to pass through less material before reaching the surface of the substrate. The advantage of this custom system is that it can be modified and/or coupled to other systems. This system is in fact combined with an optical trapping system which allows for precise movement of metal nanoparticles and their introduction into specific areas of a structure fabricated using TPP. Figure 5.11 shows optical images 5.11a and schematic diagram of the custom TPP system 5.11c and an SEM image of simple woodpile structures fabricated using the custom system 5.11b.

### 5.4.2 Photoresist

Unless stated otherwise structures in this work are fabricated with the commercial liquid acrylate based photoresist resin IP-L [182] which is specifically designed for two-photon polymerisation by the Nanoscribe system, and shows excellent resolution and mechanical stability. Using this material feature sizes down to 150nm can be achieved, structures show little shrinkage during post processing and good adhesive properties with glass substrates. The material is also designed for ease of use, it can be drop cast onto the substrate and no pre or post-bake is required. The material also has a simple development process of repeated rinsing cycles of propylene glycol monomethyl ether acetate (PGMEA) and isopropanol (IPA). The material is designed to undergo polymerisation under exposure of light with a wavelength of 390nm or 780nm for two-photon polymerisation. IP-L has a refractive index of 1.48 at 780nm similar to that of the glass substrate therefore there is little refraction at the substrate/IP-L interface. IP-L has the added advantage, unlike most photoresists, of being fluorescent under exposure allowing for visual monitoring of fabrication via the live camera.

### 5.4.3 Our light trapping designs

Since there are no theory/simulations of the optimal "free-form" light trapping structures which can be manufactured using two photon polymerisation sub-micron 3D-printing, the designs used predominantly in this work were adapted from the pyramid microstructure arrays fabricated by Labelle *et al.* [88] and described in chapter 3, and investigated with our ray tracing simulations. This was done for a number of reasons, first there is as already theoretical modelling and experimental data to show that this structure has impressive light trapping capabilities in the $TiO_2$ active layer [88, 183]. Secondly, so our results could be compared directly with previously published work by Labbelle at al and other work also using pyramids of this geometry [184]. And finally, similar to this work we use a stamping procedure to pattern our $TiO_2$ electrodes using 3D printed polymer stamps, the gradient of the pyramid wall makes this structure excellent for patterning electrodes in this manner. Ray tracing simulation results in chapter 6 also show pyramid arrays of this geometry to have impressive absorption enhancing effects.

In simulations conducted by Labbelle at al pyramids side wall angles of 80° had the best performance enhancing effects, however for practical fabrication reasons side wall angels of 54.7° were chosen. The group used anisotropic etching of silicon to fabricate a template which is used to fabricate polymer stamps which in turn are used to pattern the $TiO_2$. Silicon's natural etch plane of 54.7° directly facilitates implementation of pyramids with these side wall angles. However, in our simulation results to follow in chapter 6 pyramid side wall angles of 54.7° were one of the best performing pyramid geometries. This difference in performance for differing geometries can be attributed to the different systems being studied, in their case using PbS quantum dots for $TiO_2$ sensitisation.

There are two small differences between our final designs and the designs fabricated by Labelle *et al.* which need to be noted as they could slightly affect the structures optical properties. First the tops of our pyramid structures were flattened, with the apex of the pyramid becoming a 1×1µm square. This was also due to practical reasons, with this modification being made to help maintain high quality structures during stamping. Without this change pyramids tips are more prone to snapping off during the stamping procedure, if the tips break off it can lead to significant damage to the rest of the structure. Another change is that the gap between pyramids was slightly increased to 1µm to help reduce cracking in the array. This will be discussed in more detail below where the stamping procedure and the resulting patterned electrodes are be presented and explored. The effects of these changes are evaluated via ray-tracing simulations, the results of which are presented in chapter 6. Figure 5.12a shows the dimensions for our final design of the pyramid structures predominantly studied in this work. With the periodic pyramid array being depicted in 5.12b, the 3D printed polymer stamps are simply the inverse of this structure. The stamp structures can be made in any CAD software and exported as a stereolithography (stl.) file, which is format a that can be used by the Describe software described below.

### 5.4.4 Software

The commercial Nanoscribe TPP system runs a script language called GWL [185] containing a list of stage coordinates in X, Y, and Z, and a fourth column which sets the laser power. By programming commands using this language directly simple structures can be designed and built, such as the woodpile structure seen in figure 5.11b. For more complex structures their Describe software converts CAD stereolithography (stl.) files (commonly used in 3D printing) into GWL

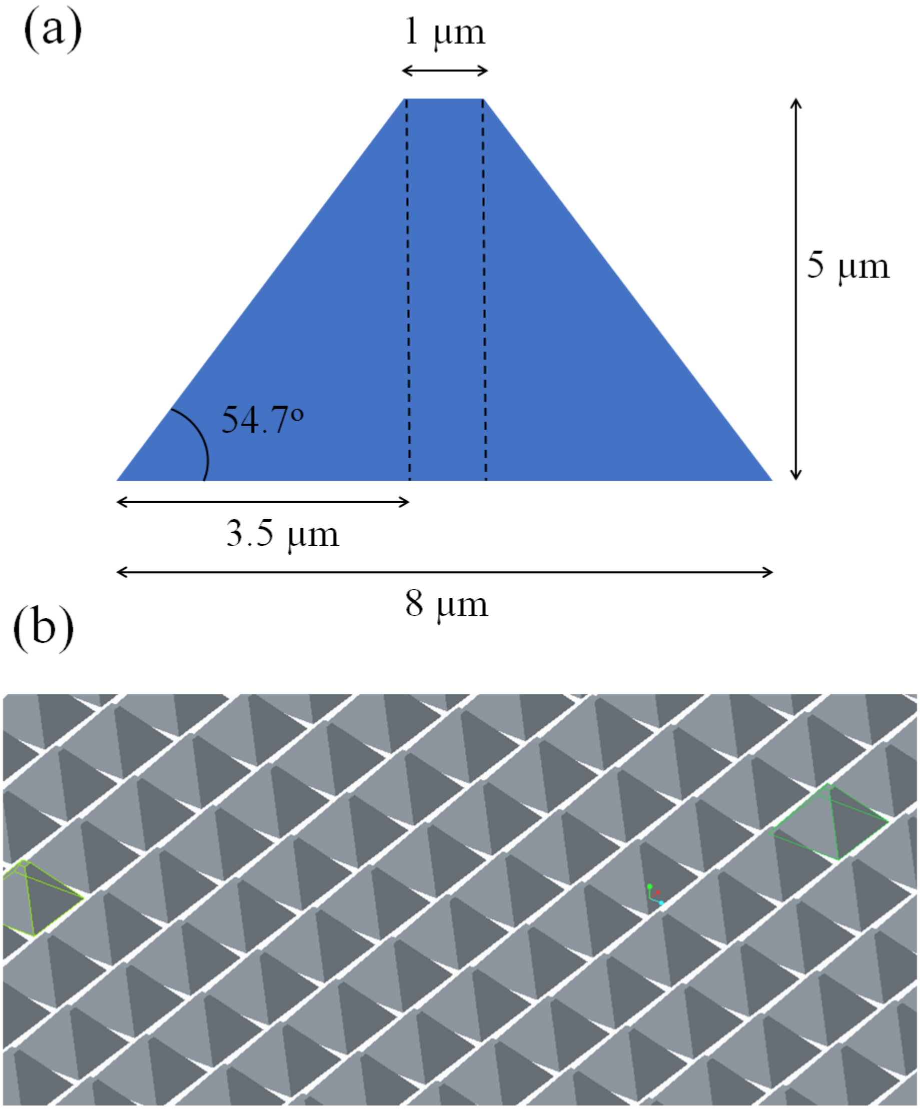

Figure 5.12: (a) Dimensions of our pyramid microstructures. (b) Stl file showing desired $TiO_2$ light trapping pyramid periodic pyramid array, stamp is made from inverse.

commands for the TPP system. After the stl file is imported the 3D structure is sliced into several layers as seen in figure 5.13a and b, thereby allowing the TPP system to build the desired structure layer by layer. Next hatching is selected for the internal structure, which can be done in two different ways either with contour hatching or linear cross hatching, seen in figure 5.13c and d respectively. The parameters selected for slice thickness and hatching frequency and type (along with laser power) are of the utmost importance for achieving both high quality and stable structures. When determining these parameters it is also worth bearing in mind that when fabricating large structures or arrays overdoing these parameters can result in extremely long build times.

Different structures will require different parameters depending on their size and shape, these parameters can only really be determined by empirical optimisation. Although a general rule can be followed whereby slicing should be at least half the Z resolution and hatching distance should be also be at least half the X-Y resolution resulting in significant overlap of layers and contours which gives high quality and stable structures. Another factor to take into account is the potentially excessive heating of the photoresist if the slicing distance is too small. This can result in increased shrinkage, higher internal stresses and uncontrolled polymerisation. With respect to internal hatching another important factor is that if single direction hatching is used, the shrinkage during the development process can lead to anisotropic strain within the structure, and subsequent deformation.

A typical example is shown in figure 5.13 here slice thickness is 500nm, and contour distance is 100nm. With X-Y resolution being $\sim$ 150nm and Z$\sim$ 1µm respectively. After these parameters are selected the newly prepared structure is automatically converted into commands in the GWL language.

### 5.4.5 Fabrication and development process

This section will describe the work flow for sample preparation, laser writing and development.

25x25mm square glass cover slips with a thickness of $\sim$ 170µm are used as a substrate onto which the structures are fabricated. Substrates are first cleaned by rinsing with acetone, isopropanol and deionised water respectively and dried under nitrogen gas flow. Substrates are placed into the sample holder and fixed. The desired photoresist is drop cast onto the substrate. Unlike most photolithography techniques, in TPP spin coating of the photoresist is not generally required since only the very specific voxel volume will be exposed. In this work the predominately used IP-L photoresist does not require any preprocessing but others, such as the commonly used SU-8 [186], may need to be pre-baked before exposure. Immersion oil is drop cast onto the other side of the substrate which will be in contact with the microscope and the sample holder is loaded into the system. Prepared sliced and hatched GWL files, as shown in figure 5.13, are loaded into the system. The interface between the substrate and the photoresist is found and focused to, it is

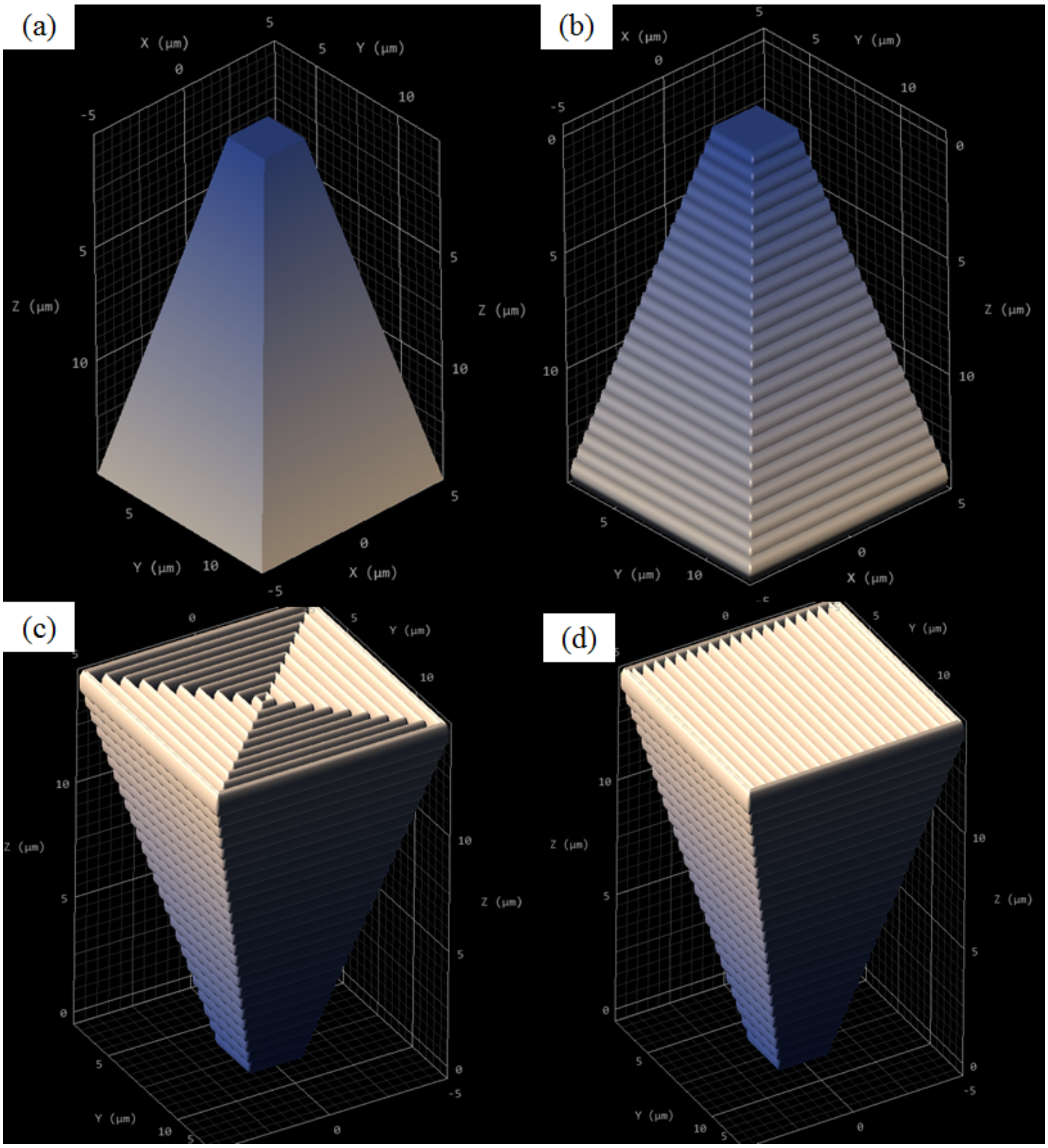

Figure 5.13: (a) Structure is imported as stl file. (b) Structure is sliced. The internal structure can either be hatched in contours (c) or in a linear cross hatching (d).

important that the first layer of the structure, or first layer of voxels, is anchored into the substrate so fabricated structures do not become loose and come away during either exposure or development. Position on the substrate can be checked for cleanliness and or defects via the live microscope and adjusted if appropriate using the stage's manual controls. Once all of these steps are completed exposure to laser light is begun.

For the development of IP-L samples are placed vertically in a PGMEA bath for approximately 30 minutes. Samples are then rinsed in an IPA bath. PGMEA and IPA bathing is repeated once more before samples are dried under nitrogen gas flow. It is important that great care is taken during the development process and that as little force as possible is applied when pulling the samples through the liquid developers to ensure minimal strain is placed upon the structures and they do not become loose and break away from the substrate. Other materials may require significantly different post processing, for example SU-8 requires a post bake before development in ethyl lactate or diacetone alcohol, before rinsing, drying and further baking.

### 5.4.6 Examples of fabricated structures

Some examples of our fabricated structures are shown in the SEM images seen in Figure 5.14. With 5.14a showing a helical cone structure, demonstrating how conventional structures, like cones, can be easily adapted using TPP. A square pillar array is shown in 5.14b. And templates or stamp structures are shown in 5.14c and 5.14d, the honeycomb like structures in 5.14c being a template for hexagonal pillars and the holes seen in 5.14d being templates for a cylindrical pillar array structure. All of these examples also show how large arrays can be produced with the high quality of the structures maintained across the array. These examples are not based on any detailed theoretical work on light trapping in DSSCs and were primarily printed while testing the capabilities of the TPP system. With resolution, reliability of the fabrication set up, the development process and final structure quality being assessed. However they were selected to roughly reflect the scale and structure types that have previously been investigated in work relating to light trapping in conventional p-n junction solar cells and DSSCs [49, 50, 52, 53], as previously discussed in chapter 2.

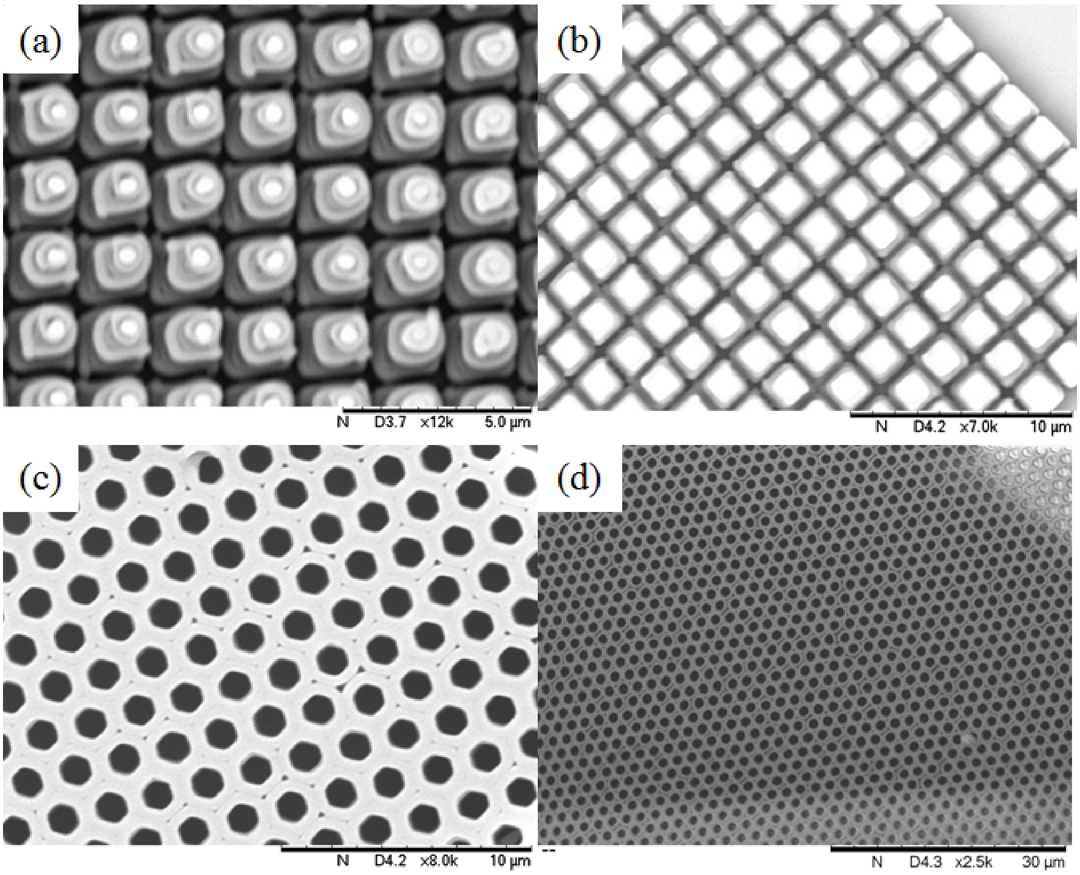

Figure 5.14: (a) Conelike structures. (b) Square pillars. (c) Honeycomb structure and hexagonal stamp/template. (d) Holes and pillar stamp/template.

The structures most extensively studied in this work are periodic pyramidal arrays. This type of structure was chosen for a detailed study both because it has been shown to have excellent light trapping capabilities and the gradient of the wall of the pyramid makes them ideal for a stamping procedure as discussed further in chapter 2.4. The inverse pyramidal stamps are fabricated in 200µm$^2$ arrays, shown in the SEM shown in figure 5.15. As can be seen in these images there are visible deformations and defects at the edges of the array, these can be attributed to shrinkage (and possibly some mechanical damage) during the development process. Although this damage can be reduced it is difficult to remove completely. By using these 200×200µm arrays we can ensure that the stamps maintain their high structural quality over a significant area in the centre of the stamp. This size of area of a $TiO_2$ patterned electrode is easily characterised in a DSSCs using the SPCM technique. Once the fabrication parameters are optimised for structures like this they can be reliably reproduced with high quality. For the inverse pyramidal

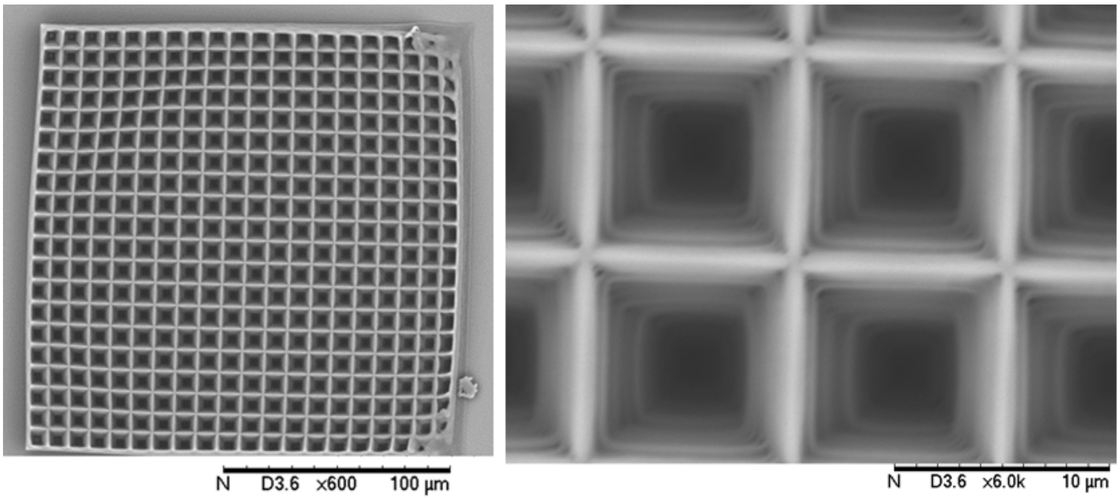

Figure 5.15: 200x200$\mu$m periodic pyramid array stamps.

stamps shown in figure 5.15 the optimised parameters were found to have a slicing distance of 400nm with contour hatching being used with a distance of 200nm.

As previously mentioned stamps cannot be characterised with SEM imaging and also be used to pattern $TiO_2$. Once the structures were optimised and shown to be reproducible with SEM characterisation future stamps which would go on to be used to pattern the $TiO_2$ were checked for quality using optical imaging as shown in figure 5.16a. Here again, as in the SEM images, deformations of the stamps can be seen around the edges, along with the high quality and low defect central region. Even with these steps taken, sometimes significant damage can occur during fabrication or post processing rendering the stamp useless for patterning. For example sometimes parts of or even entire structures can become dislodged from the glass substrate and are lost altogether. To counter this they are fabricated in batches of 9 separate stamps on the same substrate as seen in figure 5.15b, this way even with losses there will be a number of samples to work with. An optical image of one of these batches is seen in figure 5.16b. Here it can been that there are the expected slight deformations at the edges of the structures on all the stamps, however the stamp at the top right of the image has some more substantial damage than the rest and would therefore not be selected as a candidate for further characterisation. Going further using TPP it is also easy to fabricate a number of different structures with potential light trapping capabilities onto the same device. Allowing for their characterisation and testing on the same solar cell, ensuring variables such as the electrolyte, contacts and $TiO_2$ film quality

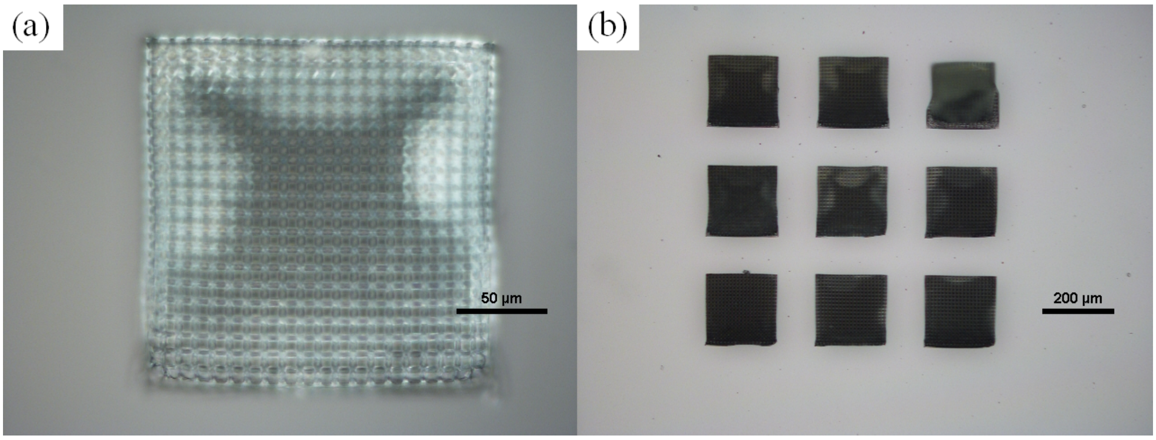

Figure 5.16: (a) Optical image of single periodic pyramid stamp. (b) Optical image of 9 stamps on the same substrate.

are the same, enabling a true comparison of their effectiveness.

## 5.5 Electrode Patterning

This section will begin with a full description of the method by which our $TiO_2$ electrodes are patterned with these polymer stamps and made ready for their introduction into DSSCs. The process begins with the careful preparation of the substrate and the application of a $TiO_2$ nanoparticle paste. Next the electrodes are patterned using the polymer stamps previously described. Before completing the process by sintering and selectively removing any organic material and other contaminants.

The description of the stamping procedure will only deal with the final optimised method for electrode patterning, however further detail on how this process has evolved and been adapted will be explored afterwards. The discussion that follows will first present EDX mapping and spectra along with SEM images, to highlight the removal of the stamps and other organic material by the sintering process. Problems and issues surrounding the fabrication of high quality patterned electrodes, such as cracking, will be highlighted using these characterisation techniques. Solutions to or the mitigation of these problems will presented and their effectiveness showcased with further optical and SEM imaging. The end result being the reproducible and consistent fabrication of high quality patterned $TiO_2$ electrodes for use in DSSCs.

### 5.5.1 Stamping Procedure

Before patterning, electrodes must be carefully prepared. This preparation follows in a similar manner to the preparation for a traditional planar $TiO_2$ electrode, any differences will be highlighted. The working electrodes use fluorine doped tin oxide (FTO) conducting glass substrates (Pilkington, TEC15, sheet resistance 15Ω/square). These are first cleaned in an ultrasonic bath with acetone for 1min, isopropanol for 1min and finally ethanol for 1min before being dried under nitrogen gas flow. Next a $TiCl_4$ blocking layer is applied to increase adhesion and reduce recombination [187]. The FTO conducting glass is placed in a $TiCl_4$ solution (0.04mM) at 70°C for 30min, before being rinsed with deionised water and isopropanol and dried again.

The $TiO_2$ layer (18NR-T transparent titania paste, Dyesol [188]), with an average particle size 20nm, can be applied to the electrode either by screen printing or by a doctor-blading technique. This titania paste is optimised for 43T screen printing synthetic mesh which was used here when this method was applied. Screen printing gives a layer thickness of approximately 6-7µm. For the doctor-blading technique scotch tape is used as a mask, the paste is applied to the edge of the mask and pressure is carefully and evenly applied with a glass rod to ensure an even spread across the area. For both techniques a 5x5mm active layer of $TiO_2$ paste is applied. In this work the doctor-blade technique was predominantly used due to availability of resources. The electrodes are now prepared for patterning with the polymer stamps. SEM image of a final patterned electrode can be seen in figure 5.17.

When preparing a $TiO_2$ electrode for use in traditional planar cells, this first layer is applied and sintered at 500°C for 30min. Another layer is then applied which is sintered again under the same conditions. Now a final scattering layer of 300nm average size $TiO_2$ nanoparticle is applied before another $TiCl_4$ treatment and final round of sintering. This second $TiCl_4$ treatment helps to increase dye adsorption due to changes in film morphology [16]. The result is a $\sim 15-20$µm thick $TiO_2$ layer. In this work highly optimised and high performance complete cells are not generally required, as we are only comparing light trapping effects in local areas of the same cell with our SPCM technique. Therefore these multilayer cells with a larger nanoparticle light scattering layer are not required and only one layer of patterned $TiO_2$ is used, both simplifying the fabrication procedure and allowing for easier comparisons.

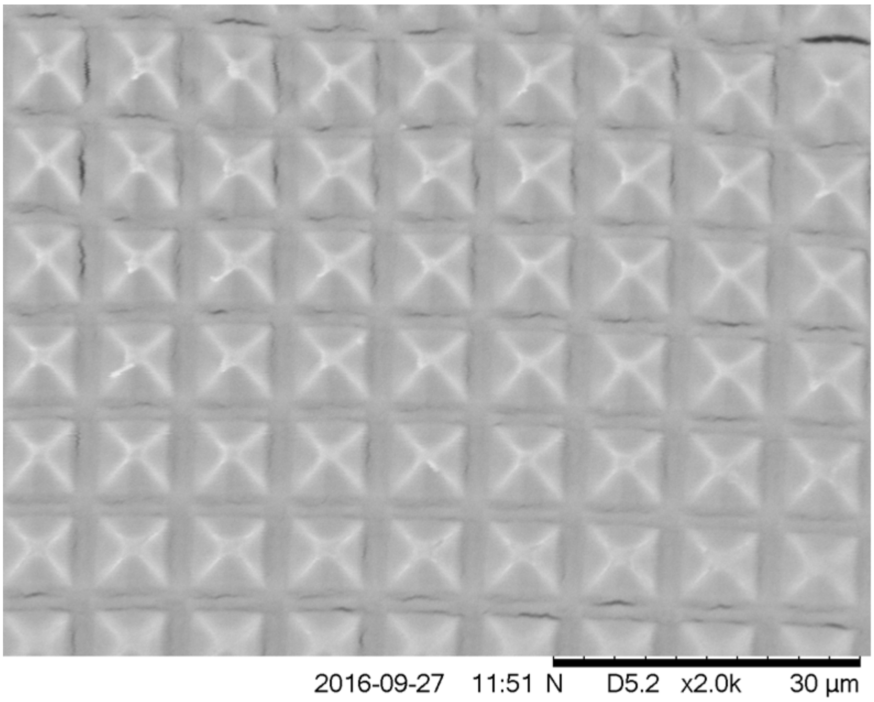

Figure 5.17: SEM image of final patterned electrode.

The prepared electrodes are quickly transferred to a hotplate and left to partially dry for 1min at 100°C. Polymer stamps are carefully pressed into the $TiO_2$ and lightly clamped to secure in place, where they are left to stand for 5min before being removed. The stamps are now sintered by slowly heating the sample to 500°C at 5°C/min then held for 30min. Individual $TiO_2$ nanoparticles tend to partially weld together during this sintering process significantly improving the electrical conductivity in the layer [16]. In some cases the stamps come away from their glass substrates and remain on the $TiO_2$. In this case the sintering process also acts to remove all organic material, including any remaining polymer stamps from the $TiO_2$ leaving the desired patterned $TiO_2$ electrode. The electrode is now ready to be incorporated into the DSSCs, a description of DSSC fabrication will follow later in the chapter.

### 5.5.2 Further Details on Development of Method: Sintering, Stamp Removal and Design Changes

As mentioned the sintering of the $TiO_2$ layer not only helps to greatly increase the conductivity of the cell but also, in our method, it has the added benefit of removing any organic material from the cell. This means the polymer stamps can be selectively removed whilst maintaining the high quality patterned $TiO_2$ layer.

After sintering cells are imaged with SEM, to check the quality and success of the patterning of the $TiO_2$ electrode. An EDX map is then taken over the same area of the cell to check for any remaining carbon, the major elemental component of the organic molecules contained in the polymer stamps, and/or other contaminates. Figure 5.18a and c show SEM images and EDX maps for patterned electrodes before sintering. Carbon is superimposed in yellow over the area which was mapped with EDX. Figure 5.18b and d shows the corresponding spectra of these maps, both show a strong carbon peak along with other expected elements, titanium and oxygen from the $TiO_2$ and the conducting substrate (FTO) which also contains tin, and silicon from the glass substrate.

These examples were chosen to show the results of some early stamping before the procedure has been effectively optimised, they highlight what happens to the electrodes if the $TiO_2$ paste is insufficiently dried before the stamping is undertaken. Much of the paste sticks to the stamp's substrate and is pulled off the electrode. This results in streaks of $TiO_2$ in-between which all material has been completely removed from the substrate. The $TiO_2$ is seen in these SEM images as dark streaks and the lighter areas between are the TCO glass substrate. Figure 5.18a represents a complete failure to pattern the electrode whilst 5.18c shows some preliminary success. It can be seen in SEM that there is some patterning of the electrode, but the quality is poor and true periodic pyramidal structures are not seen.

The EDX maps in figure 5.18a and c show only carbon in the overlay with the rest of the elements being removed to avoid cluttered and confusing images. It can be noted that the titanium, as expected, predominantly resides in the dark streaks on the SEM images, whilst the tin and silicon are found in between with oxygen pervading the entire map. Figure 5.18a shows the case where no stamps

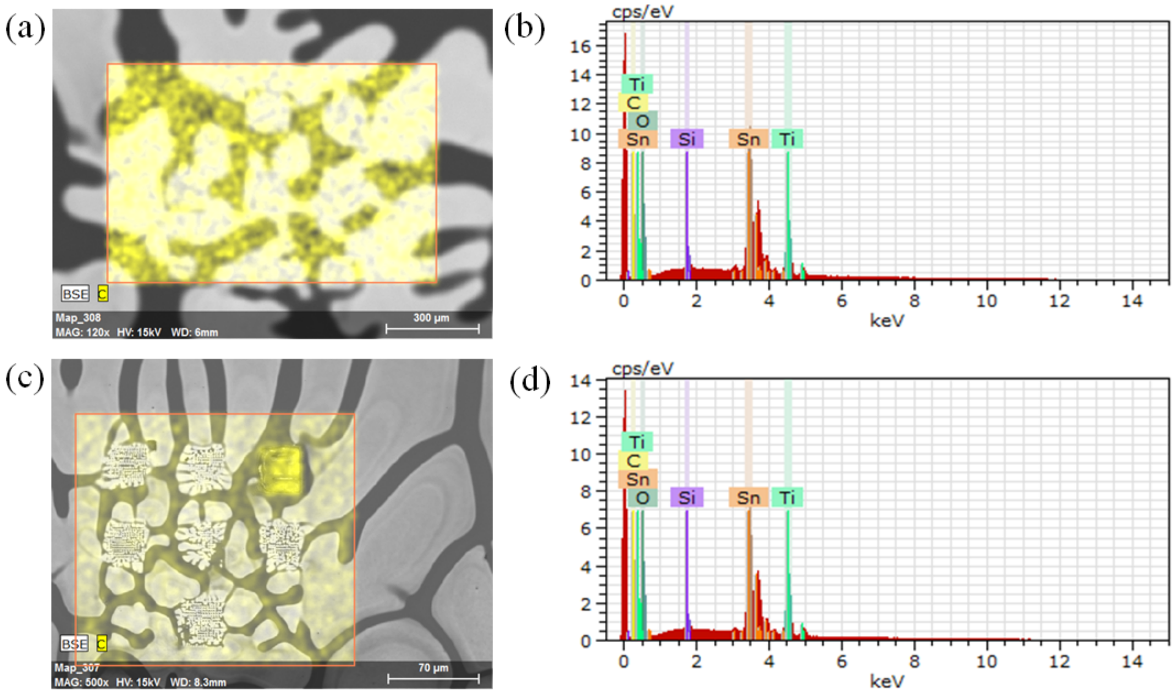

Figure 5.18: (a) EDX map of patterned electrode before sintering. (b) Corresponding spectra. (c) EDX map of patterned electrode before sintering, stamp remains on electrode at top right of image. (d) Corresponding spectra.

are left on the electrode. And figure 5.18c also shows a case where in most of the patterned areas the stamps do not remain on the electrode. However in one area, towards the top right, the stamp has come away from its substrate and is left on the electrode. This is shown by the higher density of carbon towards the top right. It is worth noting that if the stamp remains on the electrode it can be easily seen in SEM images and EDX is not necessarily required for detection. In both cases it can be seen that there is carbon across the whole cell and not just in the stamped areas, as such the sintering process is helpful in removing these contaminants along with the polymer stamps.

Figure 5.19a and c show SEM images (and EDX map in 5.19a) of patterned electrodes after the sintering process has been complete. With their corresponding spectra seen in 5.19b and d respectively.

It can been seen in both spectra and the EDX map overlay that the carbon peak has gone, suggesting that most of the carbon has been effectively removed from the electrode. Optical imaging, taken before sintering, was able to show that the

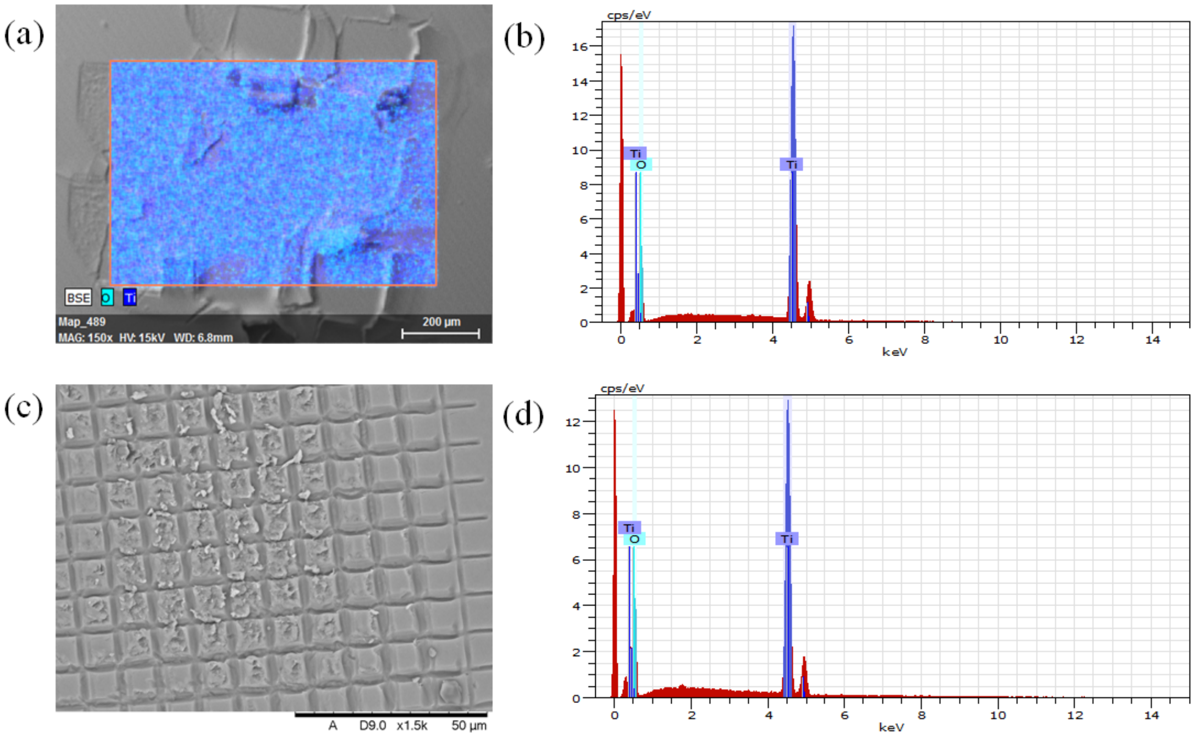

Figure 5.19: (a) EDX map of patterned electrode after sintering. (b) Corresponding Spectra. (c) SEM image, with the whole image being mapped. (d) Corresponding spectra.

polymer stamp remained on the surface in 5.19a. Showing the sintering process effectively removed this stamp along with any organic contaminates. Both spectra also show the presence of both titanium and oxygen in the EDX map overlay as expected. In figure 5.19c the overlay has been removed, in this example the whole area of the SEM image was mapped. Figure 5.19c represents a case where the stamps did not remain on the electrodes after patterning. Again no carbon contaminates are seen as they were for the same case in figure 5.18. Both 5.19a and c show examples a little further along the optimisation process of the patterning procedure, however quality is still poor. In figure 5.19a the sintering is done with a high temperature ramp damaging the patterned electrode. This damage will be discussed in more detail in the following pages. Figure 5.19c shows an example where the electrode is not sufficiency dried before stamping, resulting in the pyramid pattern not being fully formed, highlighting how important it is to stamp at the optimal viscosity of the $TiO_2$ paste. Note that no tin or silicon is seen in this EDX analysis, EDX has a resolution depth of about $1-2$µm, so only the surface elements of titanium and oxygen would be expected here.

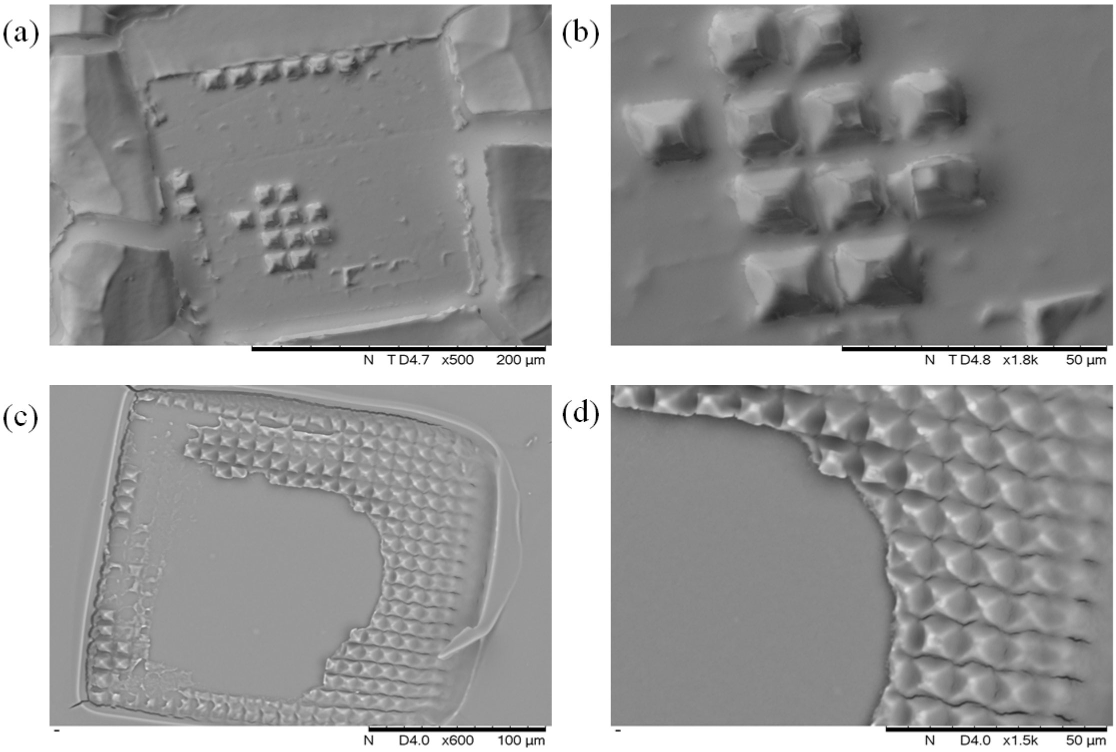

Figure 5.20: (a) SEM image showing an example of poor patterning due to high temperature ramp during sintering. (b) Higher magnification SEM image. (c) SEM image showing an example of poor patterning due to high temperature ramp during sintering. (d) Higher magnification SEM image.

Another issue related to sintering is if the temperature is ramped to 500°C too fast. This can result in the violent removal of the polymer stamp leading to mechanical damage to the patterned electrode as well as increased cracking in the $TiO_2$ film. SEM images seen in Figure 5.20a and c and their corresponding magnified images in 5.20b and d show damage to the patterned electrode, which results from a fast temperature ramp. The polymer stamps undergo some shrinkage during heating, if the samples are heated quickly then this shrinkage is rapid and the strain placed on the structures can lead to the damage seen in figure 5.20. This damage can be significantly reduced by the reduction of the temperature ramp to 5°C/min.

The reduction of the temperature ramp also helps to reduce large micron to mm size cracks which can appear on the electrodes during sintering. Figure 5.21a shows an optical image of a patterned electrode prior to sintering. Figure 5.21b shows the same electrode after sintering at a high temperature ramp before being dried. As can be seen there is significant damage to both the planar $TiO_2$ and the patterned

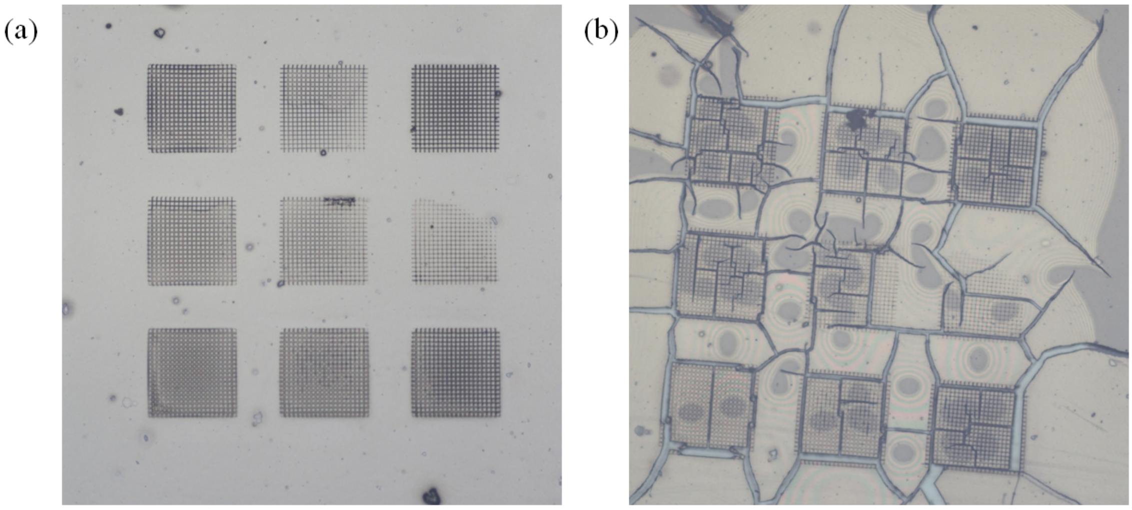

Figure 5.21: (a) Optical image of patterned electrode before sintering. (b) Image after sintering with fast temperature ramp and insufficient drying.

area, effectively ruining any chance for characterisation of the effectiveness of these light trapping structures in DSSC. These cracks are much more prominent when the samples are sintered before being properly dried. Ensuring the samples are dried at 100°C for 10min before a slow temperature ramp to 500°C for sintering can drastically reduce or even completely remove this large scale cracking in the electrode.

By reducing the temperature ramp during sintering and ensuring electrodes are sufficiently dry before sintering we can mitigate or remove these large cracks from the $TiO_2$. However smaller cracks in-between the pyramids, as seen in figure 5.22a, remain. This issue can be tackled with a slight modification of the stamp design to give a larger gap between the pyramids. This extra space means that the pyramid walls are no longer joining each other directly, and the walls of adjacent pyramids now join a flat surface, giving less chance for cracks to form. Figure 5.22b shows the original stamp design. In the modified design, shown in figure 5.22d, the pyramid dimensions remain constant, but the gap between individual stamps is increased to 2µm. The effects of this modification can be seen in figure 5.22c which shows an SEM image of patterned $TiO_2$, cracks between individual pyramids have now been drastically reduced.

By controlling the sintering temperature ramp along with slight modifications to the stamp design, high quality patterned electrodes can be reliably reproduced.

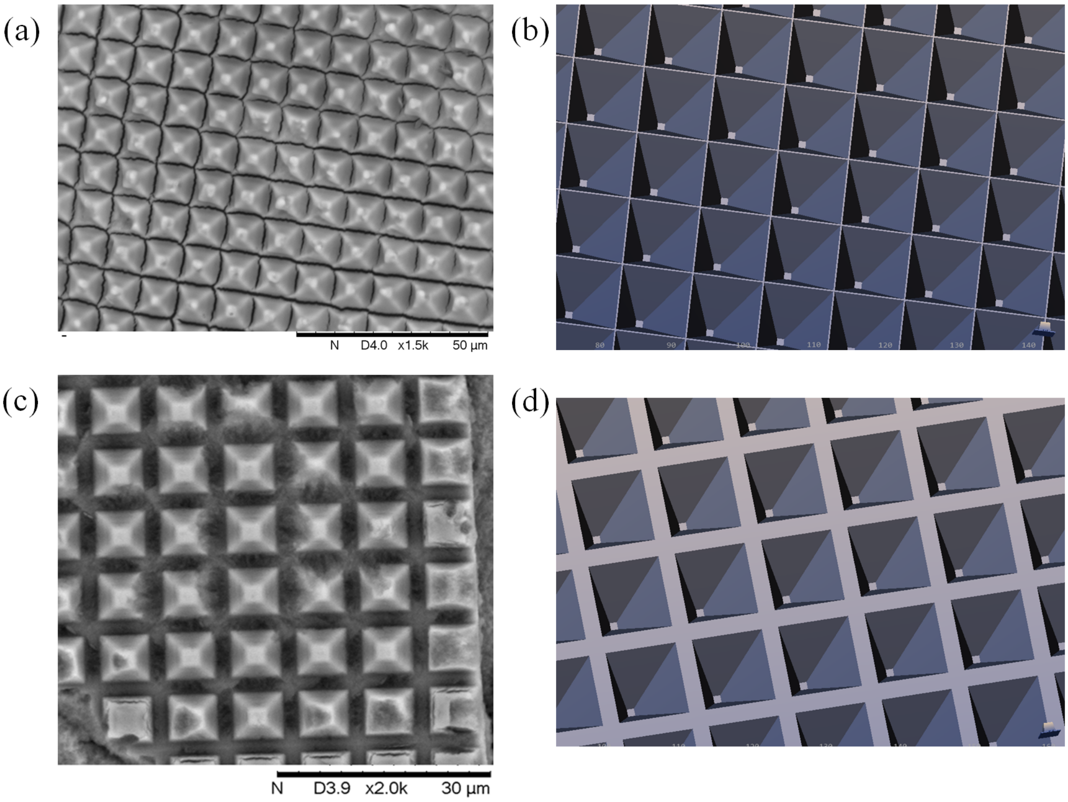

Figure 5.22: (a) SEM image showing cracking in-between pyramid structures. (b) Original stamp design. (c) SEM showing improvement in cracking. (d) Modified stamp design.

Figure 5.23 shows the results of the careful improvement and optimisation of the electrode stamping process. With figure 5.23a showing an SEM image and b showing a higher magnification image of this same electrode. Despite a dramatic reduction of cracks on the micro scale, some still remain. Again these cracks form where the pyramid walls join the planar $TiO_2$. Figure 5.23c and d show SEM images from two further examples where the fabrication process has been finalised. Here figure 5.23c shows no cracking at all at the bases of the pyramids, although there is some structural damage at the pyramid apex. And figure 5.23d shows an electrode where the quality is very similar to that of the example shown in 5.23a and b but with slightly improved cracking. These examples were selected to show that although the quality is generally high it is impossible to completely remove all defects and damage from the sample using these methods. The complete removal of one type of defect tends comes at the cost of the introduction or growth of others.

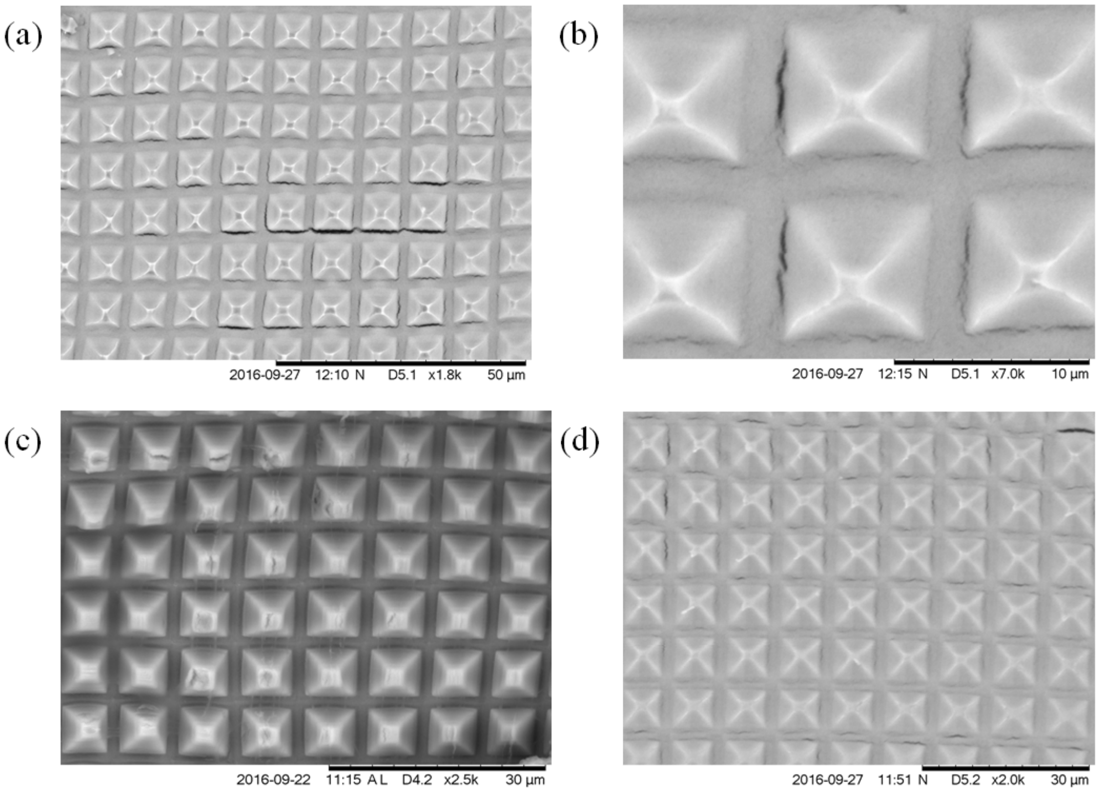

Figure 5.23: (a) SEM image showing patterned electrode after optimised stamping procedure (b) Higher magnification image of same sample. Further examples of patterned electrodes (c) and (d).

## 5.6 DSSC Fabrication

### 5.6.1 $TiO_2$ Electrode Sensitisation

Following the final sintering stage of the preparation of the working electrode described in the previous section electrodes are cooled to 70°C and immersed into a 0.5mM N719 ethanol solution dye bath (Solaronix, Ruthenizer 535-bisTBA) where they are left in the dark for at least 12 hours. As previously mentioned this dye is predominantly used in this work, the absorption spectra and molecular structure can be seen in figure 2.8. However the characterisation of traditional planar cells shown in the results chapter use the dye known as D149. The absorption spectra and molecular structure of this dye are shown in figure 5.24. Again when using this dye electrodes are immersed in a 0.5mM D149 (Sigma-Aldrich) tetrahydrofuran solution dye bath overnight. This is the most popular of a group of dyes known

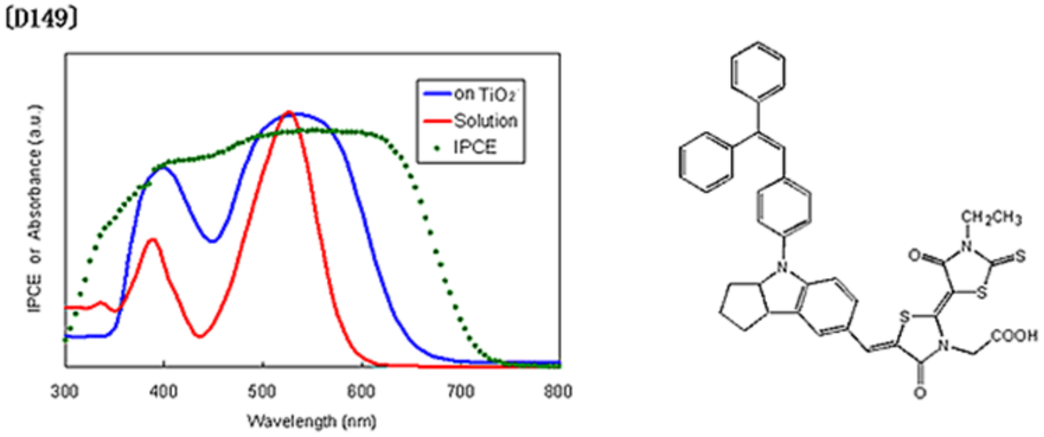

Figure 5.24: Absorption spectra of dye D149 and molecular structure [189].

as indoline dyes which attract attention as they can be significantly cheaper and less volatile than their better performing ruthenium dye counterparts. For both dyes electrodes are removed from their dye bath, rinsed in ethanol and dried under nitrogen gas flow, and used immediately in cell assembly.

### 5.6.2 Preparation of Counter electrode

To prepare the counter electrodes first a small hole ($\sim$ 1mm) is drilled into the corner of the FTO conducting glass (Pilkington, TEC15, sheet resistance 15$\Omega$/square). The electrolyte will be injected through this hole once the cell is assembled. The electrode is thoroughly cleaned in detergent solution, rinsed with deionised water, cleaned in ultrasonic bath with acetone for 1min, isopropanol for 1min and finally ethanol for 1min before being dried under nitrogen gas flow. The platinum catalyst precursor (Platisol, Solaronix) is brush-painted onto the electrode and activated with heat treatment at 450°C for 15min before allowing the sample to cool to room temperature. Prepared electrodes can be left in air at room temperature without a significant drop in performance but it is advised to use the electrodes as soon as possible after their preparation.

### 5.6.3 Cell Assembly

Cells are assembled with the electrodes face-to-face with 25 or 30µm thick thermoplastic frame (Surlyn-30, Dyesol). As mentioned working electrodes are removed from the dye bath, rinsed in ethanol and dried. The suryln frame is arranged so it is in the corner of the counter electrode with the hole on the inside of the frame. Electrodes are carefully put in place over the counter electrodes and transferred to a hotplate at 120°C, pressure is applied and after a few seconds the cell is removed, if the cell is completely sealed no air bubbles will be seen in the thermoplastic. The assembled cell is filled with the electrolyte containing the $I^-/I_3^-$ redox system (Iodolyte HI-30, Solaronix) through the pre-drilled hole in the counter electrode. This hole is sealed with a solid piece of surlyn and a glass coverslip. Figure 5.25 shows a schematic of the full process of DSSC fabrication with the insert showing an optical image of a finished cell. Conductive sides of the electrodes outside the seal are cleaned with ethanol and painted with silver paste. The cell is now complete, however cell performance can improve over the next 24h as electrolyte diffuses fully through $TiO_2$ film.

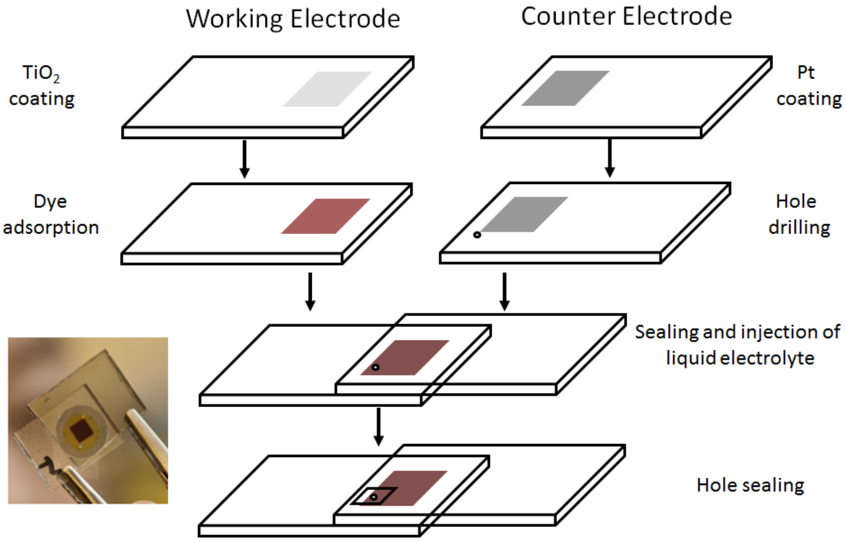

Figure 5.25: Schematic diagram showing cell fabrication procedure. Insert shows optical image of finished cell.

## 5.7 Summary and Conclusions

This chapter has detailed the full methodological approach for the 3D printing and implementation of light trapping designs into the $TiO_2$ active layer of DSSCs. It begins with the method and model description for our ray-tracing simulations, the results of which will be presented in the next chapter, before moving on to the characterisation methods used to analyse these structures through every stage of their fabrication process and their eventual performance enhancing effects for the cell. Optical and SEM imaging is used during both the stamp fabrication and the electrode patterning stages, to evaluate structure quality and highlight any defects and deformations in the patterned areas. EDX is used for elemental analysis after electrode patterning to check for any residual carbon from the stamping procedure. Traditional methods of solar cell characterisation are detailed and their appropriateness for our purposes discussed. Our SPCM set-up is described next, it will be this technique that plays the predominant role in the characterisation of our light trapping structures in the results chapter to follow.

Next the chapter moves on to detail and discuss stamp design and fabrication using TPP. This novel technique allows an unprecedented level of control over the fabrication of micron and sub-micron light trapping structures of virtually any arbitrary shape for DSSCs. The fabrication procedure for polymer stamps and templates from the design and software stage through to their fabrication and subsequent development is carefully optimised to ensure the highest quality structures are produced. During the optimisation stages fabricated structures are sputter coated and imaged with SEM, until high quality and reproducible samples are achieved. Many stamps can be fabricated on the same substrates allowing for the easy comparison of a number of different light trapping designs to be compared locally on the same device.

Some other interesting points to raise are that the fabrication process can, with small modifications, be adapted for the printing of polymer templates directly onto the transparent conduction oxide. The templates could then be infiltrated with $TiO_2$ much like some of the examples in chapter 3, before being selectively removed. In this work relatively simple inverse pyramidal periodic polymer arrays are most extensively studied, however almost any arbitrary 3D shapes can be fabricated and tested, freeing designers from the limitations of some of the fabrication methods discussed in previous chapters.

It is also shown here that $TiO_2$ electrodes can be successfully and reliably patterned with these 3D printed polymer stamps. First electrodes are prepared with a planar $TiO_2$ layer, when this layer is partially dried the polymer stamps are pressed into the electrodes and held. Stamps are removed and now the electrode is sintered at high temperature, this process also removes polymer stamps which remain on the electrode along with any other remaining organic contaminates.

Structure quality is assessed with optical and SEM imaging and elemental analysis is conducted with EDX. These results show that the polymer stamps are completely removed during the sintering stage, along with any other carbon contaminants. With the only elements of significant quantity present at the surface being titanium and oxygen, as expected. Results show that careful control of all the stages of the patterning procedure must be optimised and maintained to acquire high quality patterned electrodes. From the beginning stamp structures must not be designed for their light trapping capabilities only, but also for their ability to create high quality $TiO_2$ structures. This can be seen by the stamp modifications that were made to reduce cracking. Another important factor is the waiting for the $TiO_2$ to be dry but not too dry so structures can be stamped into the paste. And finally temperatures must be increased slowly to the required sintering temperature of 500°C. This can help to mitigate cracking on the electrode as well as ensuring any stamps that are left on the electrode do not damage the structures during their removal. If all of these steps are followed carefully high quality light trapping structures can be patterned into electrodes with a high degree of reproducibility. Finally details of cell fabrication are shown, with counter electrode preparation, $TiO_2$ electrode sensitisation and cell assembly discussed.

The chapter also details the method for our ray-tracing simulations the result of which will presented in the next chapter. A description of our model and details on the material properties are discussed.

To conclude we have shown a reliable method for the fabrication, using TPP, and implementation, using a mechanical stamping method, of light trapping designs onto small area of the $TiO_2$ electrode of a DSSC. We present the necessary characterisation techniques to assure both high quality of structures throughout all stages of fabrication and to analyse the structures performance. The following chapter will look at the results obtained when characterising the performance enhancing effects of these light trapping microstructured DSSCs.

# Chapter 6

# Results

## 6.1 Introduction

This chapter presents the results from our ray-tracing simulations and experimental results for the DSSC characterisation techniques described in the preceding chapter.

Ray-tracing simulation results will include a study of the performance of our light trapping structures with the pyramid geometries used in experimental work. Their performance will be evaluated over the AM1.5 solar spectrum and compared with planer controls. Further results follow which will explore the effects on performance when adaptations to this structure are made to help facilitate fabrication and pyramid arrays of differing side wall angles.

Some results from traditional DSSC characterisation techniques will be presented to highlight how these methods are only sufficient for the analysis of whole devices and not appropriate for investigating our patterned light trapping areas within the planar active area of the device. The majority and remainder of this chapter will focus on results from our SPCM technique, which is perfect for the characterisation of our areas of light trapping structures in DSSCs. This technique is also a valuable tool for the detection and characterisation of defects and cracks in the device, with further results in this chapter reflecting this.

## 6.2 Ray-tracing Simulations

Ray tracing simulation results begin with single wavelength studies at the average of the solar spectrum (540nm), incidentally this is also close to a peak in absorption for the dye N719 which is used in these simulations and all light trapping experimental results to follow. Our light trapping structures will be compared against a planar control device.

Further results to follow will look at the adaptations in the light trapping structures made to help facilitate their microfabrication whilst maintaining high structure quality across the array and how these changes can affect absorption enhancement. Finally results from a number of pyramid arrays of differing geometries will be shown.

### 6.2.1 Pyramid array of side wall angle 54.7$^o$ (Used in experimental work)

The ray-tracing simulation results begin with a model of our light trapping designs which were used for the fabrication of patterned electrodes, and detailed in the preceding chapter. These structures have a side wall angle of 54.7$^o$, height 5$\mu$m and base diameter 8$\mu$m. These structures also have a 1$\mu$m plateau at the pyramid apex and a 1$\mu$m gap between pyramids in the array, with these modifications to the design being made for practical reasons to ensure high quality structures during microfabrication. Structure geometry can be seen in figure 6.4a below.

The first simulation results are at single wavelength of the average solar spectrum (540nm) as previously mentioned. Under these conditions the control model was found to absorb 68% of incident light, compared to our light trapping structures which absorbed 86%. An increase of total light absorbed by 18% or an enhancement in absorption by $\sim 30\%$ over the planar control. The increased absorption is attributed to the increased path length of light propagating through the active layer. This can be seen in a visual representation in figure 6.1 where only one ray is traced in the simulation for both our light trapping structures and the planar control. Note than the pyramids and base in (a) are both the same material but the pyramids are represented in a different colour due to the electrolyte which is in-between the pyramids.

Although absorption and photocurrent generation do not perfectly correlate, absorption is the most important contributing mechanism for this process. We can expect experimental results of photocurrent enhancement to be in the same region as absorption enhancements, although somewhat less due to recombination losses. In other words the absorption enhancement seen in these simulations is the maximum possible limit for photocurrent generation enhancement in our fabricated light trapping structures.

SPCM results were conducted under laser irradiation at 405nm. Simulation results at this wavelength show 16% more total light absorbed, or an enhancement in absorption by $\sim$ 22%. Experimental results (presented later in this chapter) show enhancement in photocurrent generation of up to $\sim$ 9%. Both results show reasonable agreement, with experimental work showing expected lower photocurrent enhancement than the absorption enhancement in the simulation, indicating the model is effective.

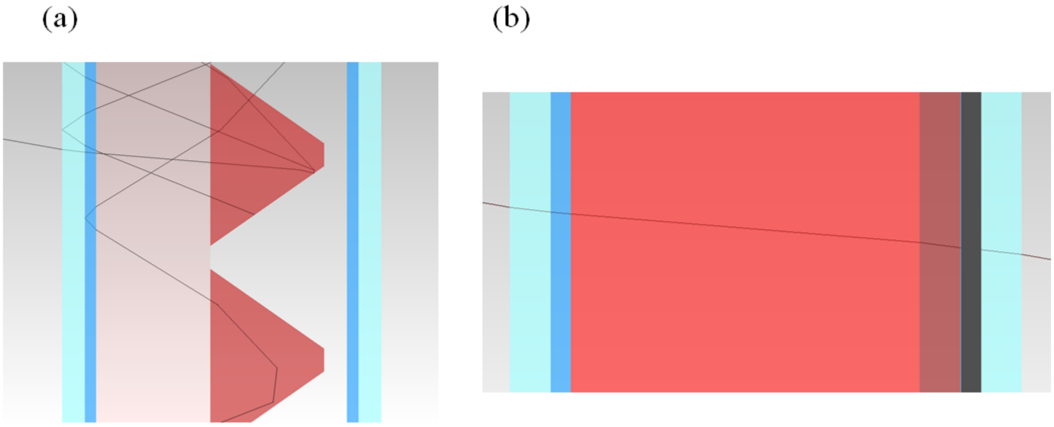

Figure 6.1: Visual aid showing how light can propagate through a DSSC device for (a) pyramid array and (b) planer device. 10° incident angle. Note increased path length for pyramid array.

### Spectral dependence and maximum achievable photocurrent density (MAPD)

Next, simulations were conducted for the same structures (control and light trapping) over the AM1.5 solar spectrum from 380-800nm. Results can be seen in Figure 6.2a, which shows that the light trapping structures absorb a higher percentage of light across this entire wavelength range. There is a dip in absorption for both systems at ∼ 450 nm. However, interestingly this is less dramatic for our light trapping structures than the planar control. With the difference between the first maxima and the first minima for the control being 15% compared to only 8% for our light trapping results. Figure 6.2b shows the increase in absorption for our structures and the planar control across this spectrum, where there is significant variation in enhancement ranging from ∼ 15% to ∼ 25% with the greatest seen between 550 − 700nm.

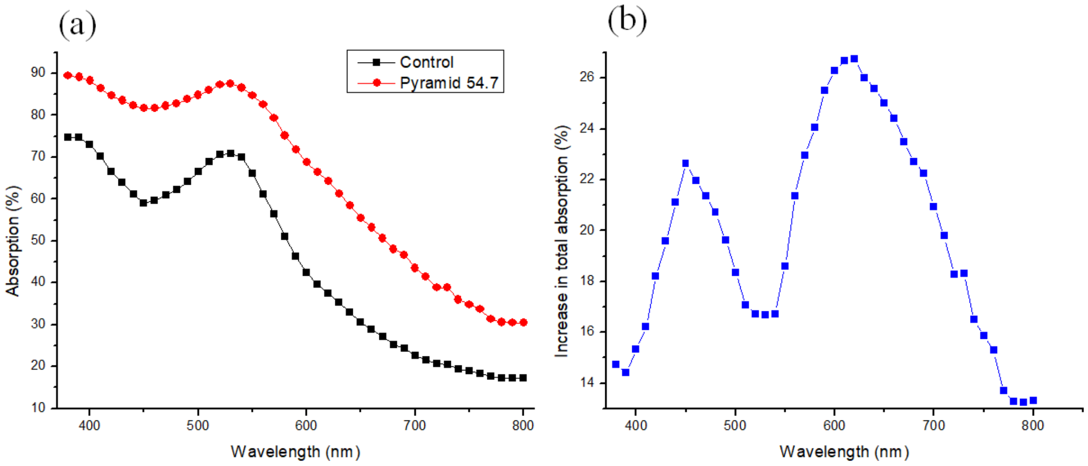

Figure 6.2: (a) Absorption over spectrum from 380-800nm for planer control and pyramid array of side wall angle 54.7°. (b) Increase in total absorption in light trapping DSSC model.

Figure 6.3a shows spectral photocurrent density plotted against wavelength over the AM1.5 solar spectrum from 380-800nm assuming an internal quantum efficiency of 100%. And figure 6.3b shows the photocurrent enhancement of the light trapping device over the planer control. This gives us more information about how the devices will perform under their intended conditions of solar irradiation. Although the devices reach their maximum absorption close to 380nm the low power of solar irradiation at this wavelength means we see the lowest value of photocurrent density. The MAPD is calculated to be 11.22 mAcm$^{-2}$ for the control and 16.55 mAcm$^{-2}$ for our light trapping device, an improvement of $\sim$ 45%. MAPD values agree well with experimental reports of the short circuit current obtained for DSSC using the dye N719 [178, 20], helping to further validate the model. These results cannot be directly compared with experimental SPCM results as they were conducted under laser irradiation of a single wavelength of 405nm and recombination losses are not taken into account. But they are a good indication that we should see significant enhancement of the photocurrent generation in these experiments.

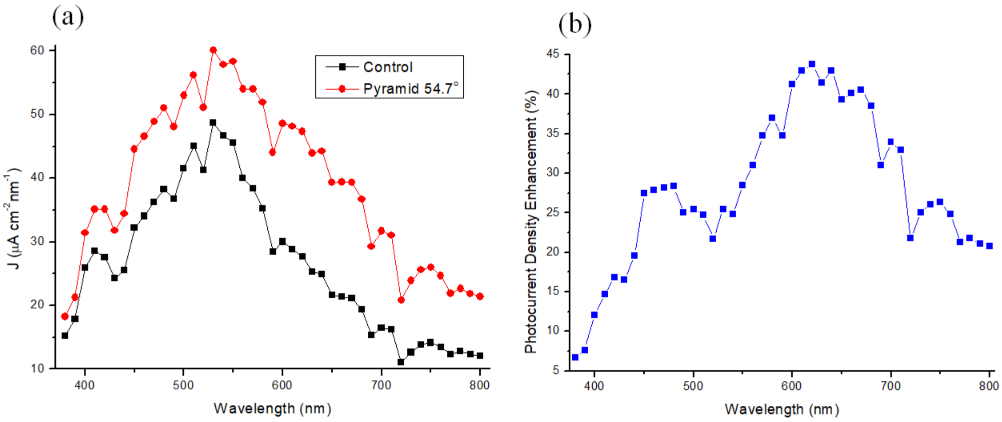

Figure 6.3: (a) Simulated spectral current-density plotted as a function of wavelength over the AM 1.5 solar spectrum from 380-800nm (b) Spectral photocurrent enhancement of light trapping model over planar control.

### 6.2.2 Variations on pyramid array of side wall angle 54.7°

With adaptations to our designs made to help facilitate the high quality microfabrication of the pyramids arrays. The next set of simulations were conducted to look at the effects these changes have on absorption. Figure 6.4 shows the four different pyramid structures compared in these results. The structures fabricated in the experimental work and studied in the previous simulations detailed above can be seen in figure 6.4a, containing both modifications of the plateau and the gap between pyramids in the array and named ‘Pyramid 54.7°’. Next, the so named ‘Perfect Pyramid’ can be seen in figure 6.4b containing no plateau and no gaps. Followed by the structure where there is a gap between pyramids in the array but no plateaus seen in figure 6.4c, named ‘Gaps Only’. Finally the structures with a

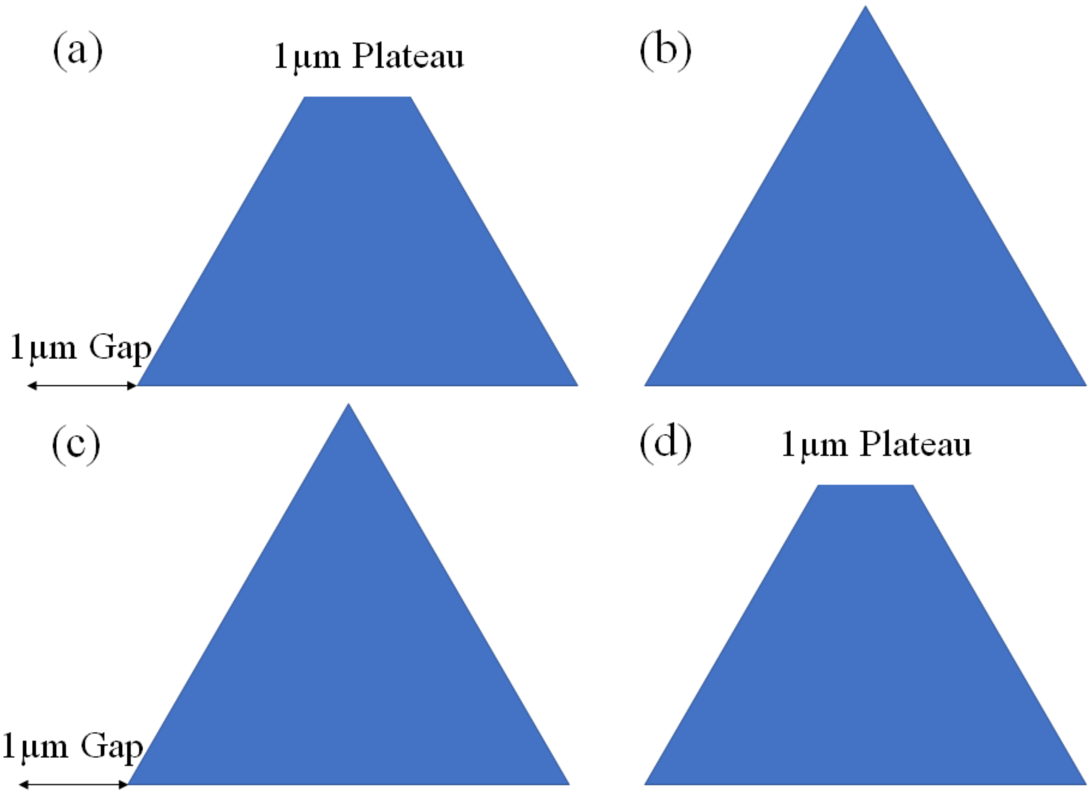

Figure 6.4: Figure showing different variations of pyramid of side wall angle $54.7^0$, where adaptations were made for practical reasons during microfabrication. (a) Pyramid geometry fabricated experimentally with $1\mu$m gap between pyramids and $1\mu$m plateau at pyramid apex. (b) Perfect pyramid array with no gaps and no plateau. (c) Gaps between pyramids only. (d) Plateau at pyramid apex only.

plateau at the pyramid apex but no gaps between pyramids in the array named as ‘Plateau Only’.

Results for these four structures and the planar control are shown in figure 6.5. Here, it can be seen that when these modifications are removed the structures perform better, with the ‘Perfect Pyramid’ structure absorbing up to 10% more light than the structures used experimentally. The structures where only one modification is removed also absorb more light than the ‘Pyramid 54.7’ however not as much as the ’Perfect Pyramid’. This is to be expected as for each modification there is a greater surface area of the array which is planar, increasing the chance that light will be not reflected back into the active layer, thus reducing the overall path length of the light in the active layer leading to a drop in absorption. Interestingly this difference reduces at longer wavelengths where the difference in all four structures falls to only a few percent. Figure 6.5b shows the corresponding

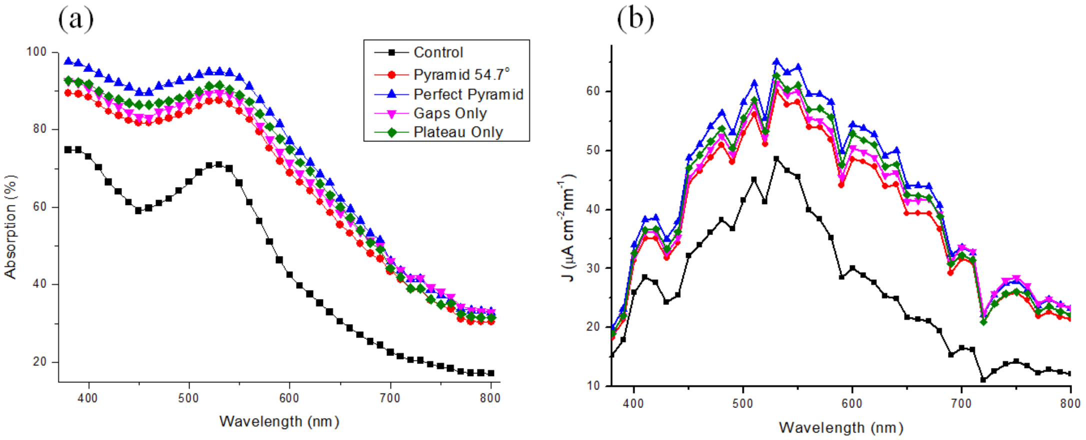

Figure 6.5: (a) Graph showing the effects structure adaptations made during microfabrication have on absorption enhancement in the device. (b) Spectral photocurrent density for pyramid modifications.

spectral photocurrent density for these structure modifications where the enhancements in absorption are reflected, their calculated MAPD and its comparison with all other simulated devices can be seen table 6.1.

### 6.2.3 Pyramid arrays of differing side wall angle geometries

Finally, simulations were repeated for differing pyramid geometries. Here the height is kept constant and side wall angle is changed with angles of 30°, 40°, 60° and 80° being studied. Note that the modifications made for fabrication are not implemented here, and all are considered to be 'Perfect Pyramids' with no gaps and no plateau at the pyramid apex.

Results are shown figure 6.6 where is can be seen that absorption is higher for only pyramids of side wall angle 40° than those physically fabricated and characterised, however this is only by a small amount. And at larger wavelengths, where there is less absorption, those pyramids of side wall angle 54.7° perform better than even these. All pyramid arrays perform better than the planar control apart from pyramids of side wall angles 30° which surprisingly perform worse at shorter wavelengths and matches the planer absorption at longer wavelengths.

At longer wavelengths (> 650nm) there is much more variation in the percentage of incident light absorbed across the different geometries. Here our structures fabricated and characterised experimentally outperform all other pyramid geometries apart from those of side wall angles of 60° which absorb a few percent more at wavelengths greater than 740nm.

Generally it can be said that all structures with a side wall angle of greater than 30° absorb more light than the planar control device. With the maximum enhancement seen in structures with side walls angle of 40°, 54.7° and 60° which are only separated by a few percent up to 650nm after which the variation increases. Pyramids with the steepest side wall angle of 80° still outperform the planar control but are significantly worse than the three best performing geometries. The corresponding spectral photocurrent density can be seen in figure 6.6b where the enhancements in absorption are reflected.

The calculated MAPD for all results are collected in table 6.1 and figure 6.7 below where the best light trapping structures show impressive improvements over the planer control. Results are in good agreement with reports in the literature using similar simulations of light trapping structures [115], and combined experimental work [88] as well as general agreement with the performance of the dye N719 [178, 20].

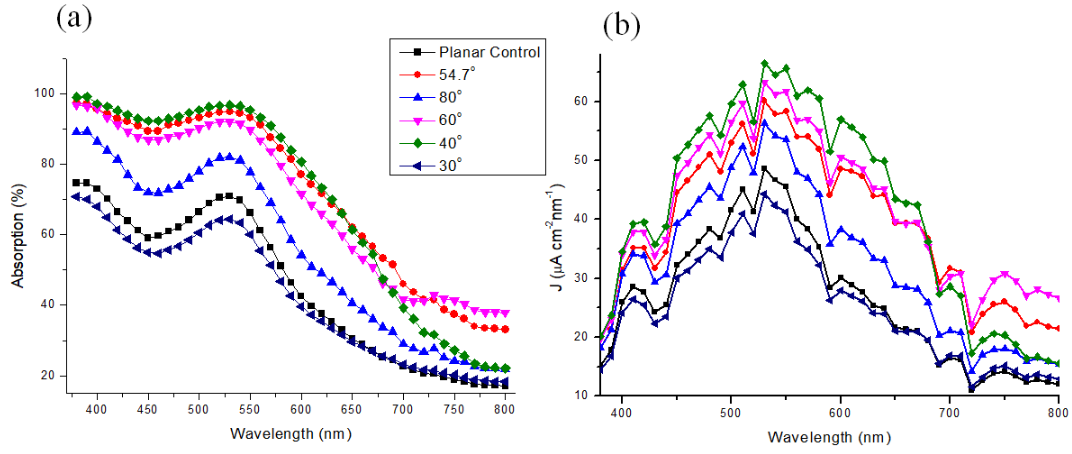

Figure 6.6: (a) Graph showing absorption for a number of pyramid arrays with differing side wall angles. (b) Spectral Photocurrent density.

| **DSSC Geometry** | **MAPD (mAcm$^{-2}$)** |
|---|---|
| Planar Control | 11.22 |
| Pyramid 54.7$^{0}$ | 16.55 |
| ’Perfect Pyramid’ | 18.21 |
| ‘Gaps Only’ | 17.25 |
| ‘Plateau Only’ | 17.42 |
| 30$^{o}$ | 10.59 |
| 40$^{o}$ | 17.71 |
| 60$^{o}$ | 17.56 |
| 80$^{o}$ | 13.81 |

Table 6.1: Table showing calculated MAPD for all device geometries simulated.

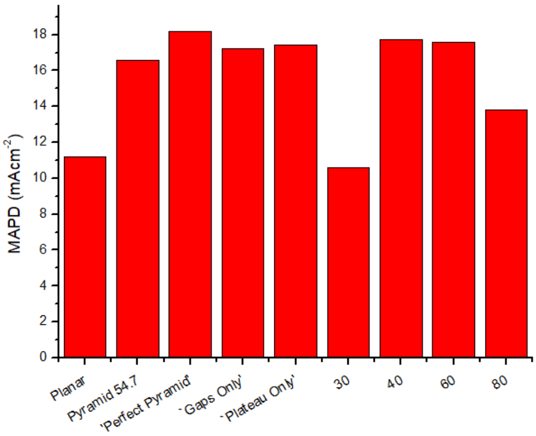

Figure 6.7: Graph showing calculated MAPD for all device geometries simulated.

## 6.3 Traditional DSSC characterisation

Before moving onto the major result of this thesis some results from traditional solar cell characterisation techniques will be presented. The purpose of this small detour is to both show how solar cells are most often characterised and that these methods are not suitable for characterising our light trapping structures which are only patterned onto a region of the active area of the device. For these experiments DSSCs were fabricated using the method described in the previous chapter, the only difference here is that these cells use the dye known as D149 as opposed to the dye used in all other results in this work, known as N719. More details on these dyes are given in the preceding methodology chapter.

Figures 6.8a and 6.9a and b show $J-V$ characteristics from three DSSC samples

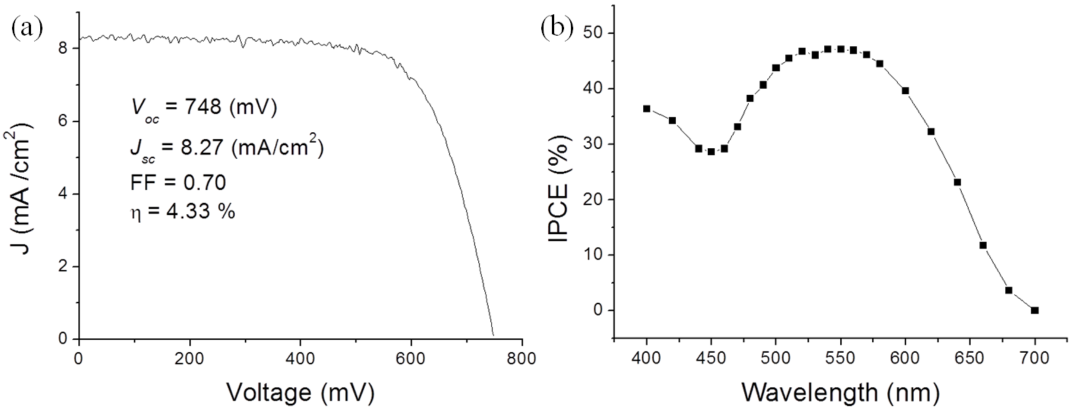

Figure 6.8: (a) $J - V$ Characteristics of T-Cell 1 using dye D149. (b) IPCE of same cell.

fabricated with a planar $TiO_2$ electrode in the traditional manner labelled T-Cell 1, T-Cell 2 and T-Cell 3 respectively. Along with values of their $V_{oc}$, $J_{sc}$, their fill factors and the overall solar-to-electrical conversion efficiencies, $\eta$. Table 6.2 shows the recorded data for all three characterised cells. All three cells show comparable fill factors, open circuit voltages. However, T-Cell 3 shows a significantly lower short circuit current. T-Cell 1 and T-Cell 2 have a value of $\sim$ 9mA/cm$^2$ by comparison T-Cell 3 has a value of $\sim$ 5mA/cm$^2$. This results in a drop in overall solar-to-electrical conversion efficiencies from $\sim$ 4.40% to 2.27%. During the assembly of T-Cell 3 there were some difficulties in back filling the electrolyte with some significant air bubbles left in the cell which this drop in efficiency can be attributed to. IPCE measurements were also made for T-Cell 1, as seen in 6.8, with results showing good agreement with expected values for D149 DSSCs [190].

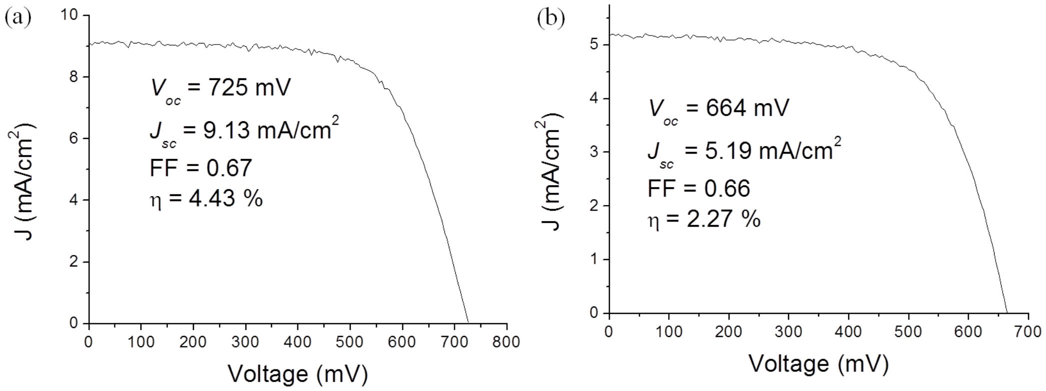

Figure 6.9: (a) $J - V$ Characteristics of T-Cell 2 and (b) T-Cell 3.

| Sample | $V_{oc}(mV)$ | $J_{sc}(mA/cm^2)$ | $FF$ | $\eta(\%)$ |
|---|---|---|---|---|
| T-Cell 1 | 748 | 8.27 | 0.70 | 4.33 |
| T-Cell 2 | 725 | 9.13 | 0.67 | 4.43 |
| T-Cell 3 | 664 | 5.19 | 0.66 | 2.27 |

Table 6.2: Table showing vales of $V_{oc}$, $J_{sc}$, FF and $\eta$ for characterised samples.

Whilst these methods are excellent for the characterisation of the overall performance of the cells, they give no information about how different areas of the device perform, therefore they are not tailored to investigate photocurrent generation on the microscopic scale required for our fabricated microstructures. For that we need the SPCM technique, where we can measure just the specific area of the cell which has been patterned with our light trapping structures. This technique can also allow for the direct comparison of different light trapping structures which can all be patterned onto the same device and tested together ensuring conditions for different structures are as close as possible.

## 6.4 Scanning photocurrent microscopy

This section will first present SPCM results from traditional planar $TiO_2$ DSSCs. This will show how there is some significant variation in photocurrent, even in a planar DSSCs. It will also serve to highlight the versatility of our SPCM system. SPCM results of our light trapping pyramid array DSSCs will next be introduced and detailed. Finally we will look at the use of the SPCM system for solar cell artefact and defect detection and characterisation.

### 6.4.1 Conventional planar $TiO_2$ DSSCs

The use of a variety of microscope objectives and the high range of the hybrid translation-piezo scanning stage (±10cm) gives our SPCM system great versatility to characterise large area devices before looking more closely and characterising them in more detail by enlarging a specific or important area of the device. The active area of our traditional planar $TiO_2$ DSSCs is between $5-6\text{mm}^2$ which can be easily mapped using large step sizes and a x10 microscope objectives. Figure

6.10 shows the whole active area of one of these planar $TiO_2$ DSSCs. In this example the laser is focused to the surface of the $TiO_2$ through the TCO glass substrate using the x10 objective, this gives a laser spot size of $\sim$ 15µm. To avoid long mapping times XY-grid spacing is set to 0.1mm, before areas of interest were selected and mapped with a greater resolution. The mean photocurrent of the active area of the device is 51.93nA ($s = 3.99$nA, $N = 400$). An interesting area of the device is towards the bottom left, where a number of low photocurrent artefacts are seen, here the value drops by $\sim$ 30% from the mean.

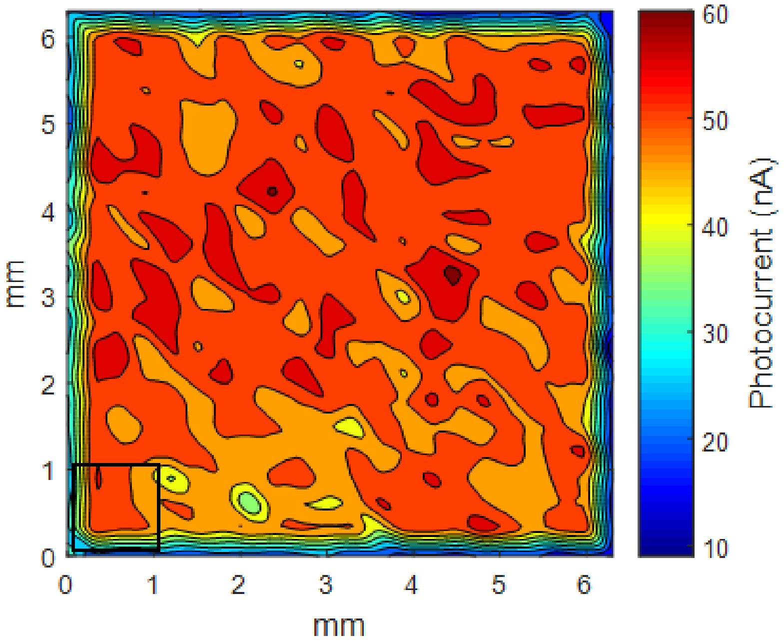

Figure 6.10: Photocurrent map of whole active area 6x6mm of traditional planar DSSC. Resolution 100µm. The region highlighted towards the bottom left of the map is mapped at a higher resolution and can be seen in figure 6.11.

The next figure (6.11) shows a higher resolution $1 \times 1$mm photocurrent map taken towards the bottom left of the same cell, the area can be seen as the black bordered region in figure 6.10. Here a low photocurrent artefact and the border of the active area of the cell can be seen, this map was taken using the x20 objective giving a $\sim$ 5µm laser spot. For this map measurements are made every 20µm. At this resolution the artefacts and the inhomogeneous nature of the photocurrent can be seen in much greater detail and reveal a lot more information about the local photocurrent conditions as these features cannot be seen in figure 6.10. The ability of this system to detect and characterise defects and artefacts in DSSCs (and by extension other semiconductor devices) will be discussed in more detail later in the chapter. In this example it is worth noting that no obvious defects or deformations on the $TiO_2$ surface or the glass substrate are seen in optical images of this area of the device, showing the effectiveness of the system at detecting artefacts unresolved with optical imaging. In this map the mean photocurrent of the active area of the device is 58.98nA ($s = 3.28$nA, $N = 1520$).

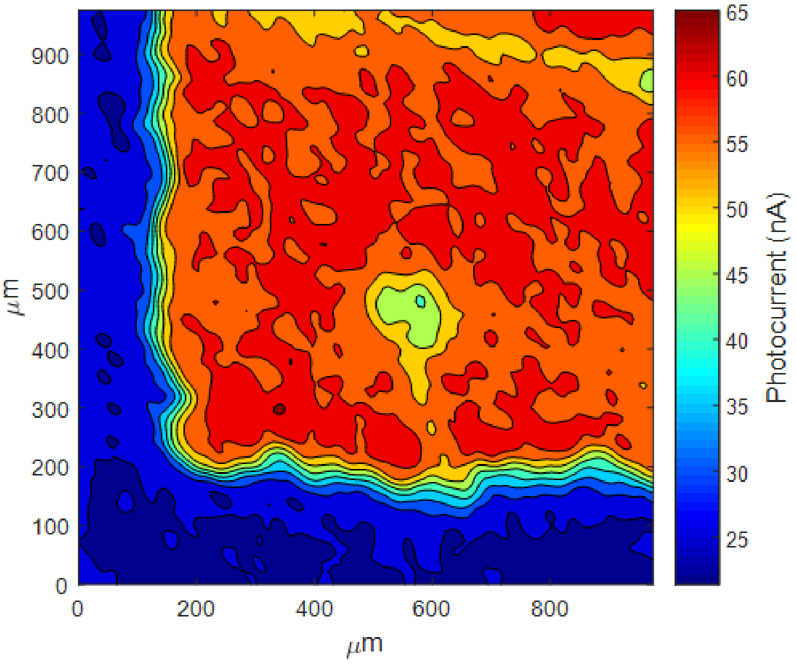

Figure 6.11: Photocurrent map of corner area of traditional planar DSSC. Resolution 20µm.

As the reader will have noticed the photocurrent is significantly higher here than in figure 6.10 in the same area. It is worth commenting on this discrepancy here as it will also be seen later in SPCM results for our light trapping structures when moving between the x10 and x20 microscope objective. One potential reason for this difference is that when using different microscope objectives the focus of the incident laser beam also changes. Whilst the total power will remain constant this change in focus will affect the power density which can in turn increase carrier mobility and electron transport through the active layer helping to increase photocurrent generation in the DSSC device [191]. To conclusively determine the mechanisms involved here further investigation is required. For the purposes of this thesis the discrepancy in total photocurrent seen in these measurements means it is important that when comparing planar and light trapping structures for enhancement in photocurrent generation we must not compare maps using different microscope objectives directly.

The next example, shown in figure 6.12, presents a high resolution photocurrent map of a different traditional planar $TiO_2$ DSSC. Here the x20 microscope objective is used to focus the laser spot to $\sim$ 5µm and measurements are taken every 5µm. A typical area of the device was selected where there were no obvious artefacts seen in lower resolution photocurrent maps. Here the mean photocurrent is 61.29nA ($s$ = 2.48nA, $N$ = 5400). In this cell, even in this significantly smaller area ($\sim$ 350µm$^2$), there is still some considerable variation in the photocurrent over the device, the nature of which is characterised excellently via the SPCM technique.

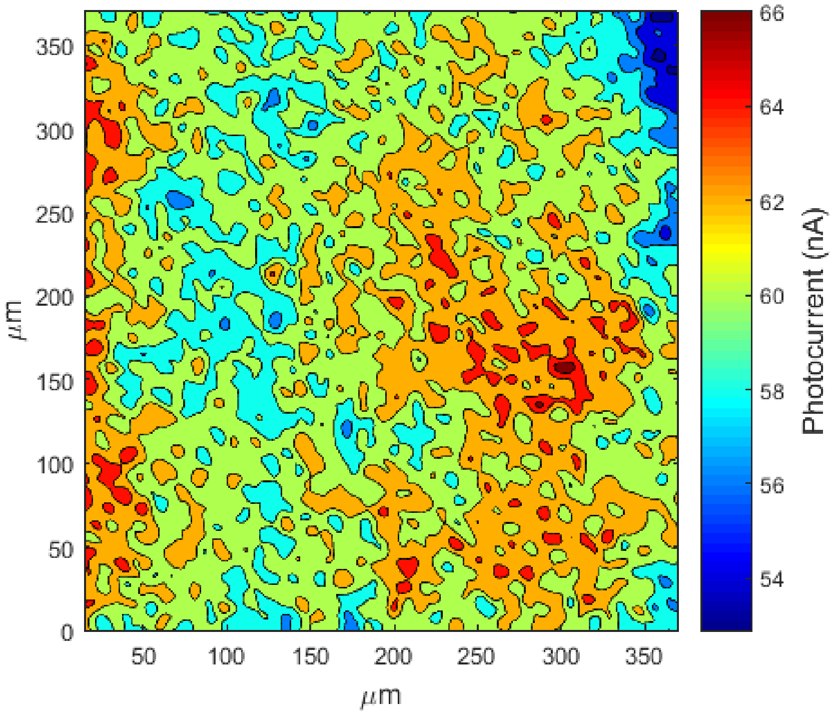

Figure 6.12: High resolution photocurrent map of traditional planer DSSC. Resolution 5µm.

Together these results demonstrate the ability of our SPCM system to measure large area devices before zooming to areas of interest and repeating measurements at a much greater resolution. This versatility can be useful in the characterisation of many different semiconductor devices and is not limited to DSSCs measurements presented in this work. They also show the system's capacity to detect and characterise artefacts and defects in DSSCs and other devices, as mentioned this will be explored in more detail later in this chapter. These results also reveal that there can be significant variation in photocurrent when randomly oriented planer

$TiO_2$ electrodes are used in the fabrication of DSSCs. We now move on to the characterisation of our light trapping structures using the SPCM techniques.

### 6.4.2 DSSCs with $TiO_2$ light trapping structures

SPCM is the perfect tool for the characterisation of our light trapping designs. It produces maps where any effect of the structures on the photocurrent generation can be clearly seen. Our light trapping stamping procedure allows many structures to be fabricated on one sample. With the versatility of the SPCM technique these structures can be mapped altogether and then specific structures or areas can be selected and remapped at much greater resolutions. This section will present SPCM results of various light trapping pyramid arrays structures on a number of DSSC samples. It will aim to showcase both the effectiveness of the technique and more importantly how successful these structures are at trapping light and consequently improving photocurrent generation in the cell.

Figure 6.13a shows a photocurrent map using the x20 objective with a laser spot size of $\sim 5\mu$m, with 480 individual measurements taken every $4\mu$m. Alongside a corresponding optical image seen in 6.13b, of four isolated pyramid structures towards the centre left of the figures (and another pyramid to the extreme right of the figure). Graphically it can be seen that the four distinct peaks towards the centre left of the photocurrent map overlap with the four pyramids in the optical image. These four pyramid structures are circled in white in the optical image and the peaks are circled in black in the photocurrent map to help highlight this overlap. The next peak in the photocurrent map comes over an area where there is a damaged pyramid structure (seen in the optical image) to the right of the four distinct pyramids. The final peak towards the extreme right is also over a pyramid structure. In this example significant damage during fabrication led to the removal of most of the pyramid array structure, but these isolated pyramid structures remained in place.

To quantify this enhancement the mean background photocurrent is compared with the mean photocurrent over the pyramid structures, the photocurrent starts to drop dramatically towards the top of the map which is towards the edge of the active area of the device, and is removed from the analysis. The mean of the

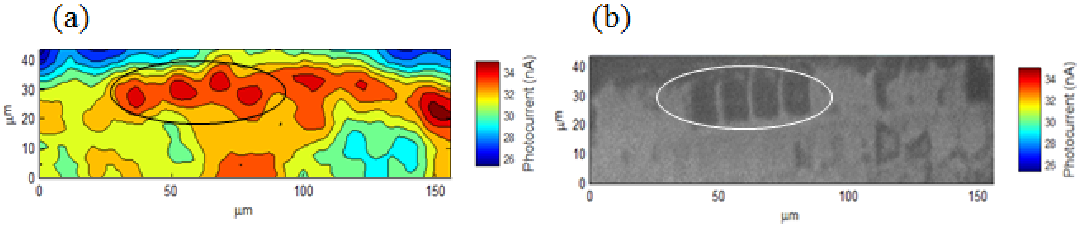

Figure 6.13: (a) Photocurrent map of four individual pyramid structures. (b) Corresponding optical image. Referred to as Cell 1 in table 6.5.

planar background photocurrent is 30.71nA ($s = 2.84$nA, $N = 102$) and the mean photocurrent over the pyramids structures is 33.74nA ($s = 2.32$nA, $N = 132$). The difference in the means is 2.63nA (CI = 1.97nA, 3.29nA) or an enhancement of 8.56% (CI = 6.41%, 10.71%). This enhancement is the first empirical evidence presented for successful light trapping in these structures. However as mentioned there is some significant damage to the electrode during fabrication resulting in the removal of most of the pyramid array. This damage may have affected the photocurrent generation in the background or planar regions which are used in the analysis of this data and as such more evidence is needed before conclusive statements can be made.

As discussed in the methodology chapter, stamps can become dislodged from their glass substrates during post processing. And as already seen in figure 6.13 significant damage can occur during the stamping procedure. To mitigate these losses and damage to the electrode stamps can be fabricated in batches of 9 separate $200\mu\text{m}^2$ periodic arrays per sample. This allowed for the selection of the highest quality areas of the patterned electrodes during SPCM mapping. Figure 6.14a shows a large area ∼$1\text{mm}^2$ low resolution photocurrent map using the x10 microscope objective giving a laser spot size of $15\mu$m and measurements taken every $15\mu$m for this 3x3 arrangement, with 4,500 individual measurements. Figure 6.14b shows the corresponding optical image. As can be seen towards the bottom left one of the stamps became dislodged the substrate leaving only 8 successfully patterned areas on the device. Graphically the figure suggests some significant enhancement of the photocurrent from our light trapping structures, which overlap nicely with the patterned areas in the optical image seen in figure 6.14b. It can also be seen that there is variation in the enhancement between the pyramid arrays. This should come as no surprise as it can be seen from the optical image, and will be seen in more detail in subsequent figures, that there is some variation in the quality of the patterned areas. Cracking is seen in positions 2, 3, 5 and 6 and, as will be discussed later the chapter in more detail, this cracking can lead to both some positive but mostly negative contributions to photocurrent generation. There is also some drift in the background photocurrent seen in the figure with the photocurrent increasing in the positive X direction over the map, this drift will be analysed in more detail below.

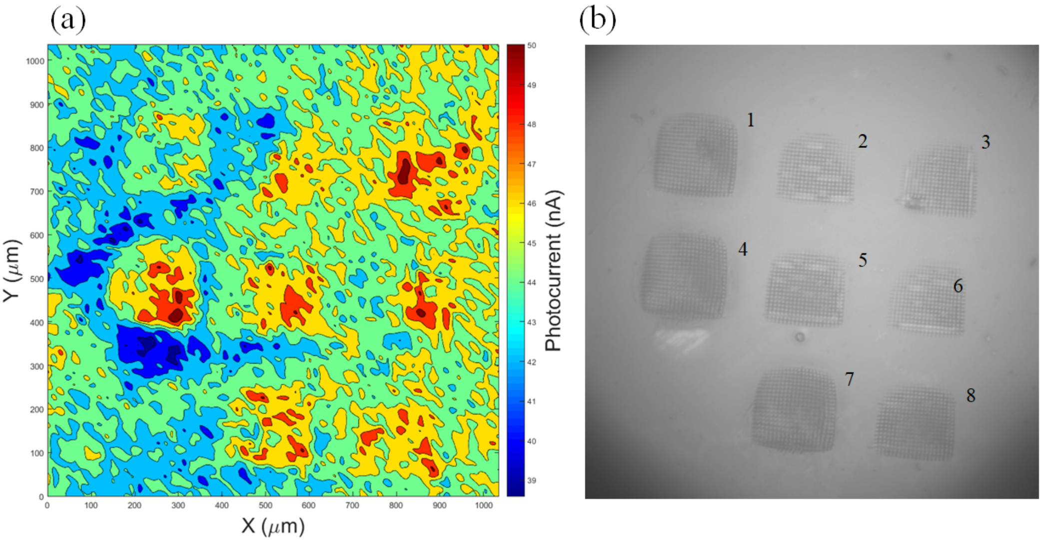

Figure 6.14: (a) Photocurrent map of 8 light trapping patterned arrays in a DSSCs. Resolution 15$\mu$m (b) Corresponding optical image with individual arrays labelled. Referred to as Cell 2 in 6.5.

Figure 6.15 shows the drift in the background photocurrent in the X and Y directions of the map in figure 6.14. The photocurrent for values labelled XX and YY in the figure are taken from across the map at positions where there are no light trapping structures. For data in the figure labelled XX, X values are read from the map when Y $= 960\mu$m. For data in the figure labelled YY, Y values are read from the map when X $= 395\mu$m. From the figure the drift in X is $1.94 \times 10^{-3}$nA$\mu$m$^{-1}$ resulting in a total drift of 2.01nA across the entire map. Although graphically it is difficult to see any drift in the Y direction this analysis reveals a small drift of $7.14 \times 10^{-4}$nA$\mu$m$^{-1}$ resulting in total drift of 0.74nA across the entire map.

The mean background photocurrent of the map, that is to say the mean of the photocurrent with the eight 200μm$^2$ pyramid arrays masked, is 44.66nA ($s = 1.70$nA, $N = 3628$). The mean photocurrents and their enhancements over the background for the 8 light trapping pyramid arrays can be seen in table 6.3, which shows enhancements of $\sim 1 - 5\%$ over the background. The standard deviation in the

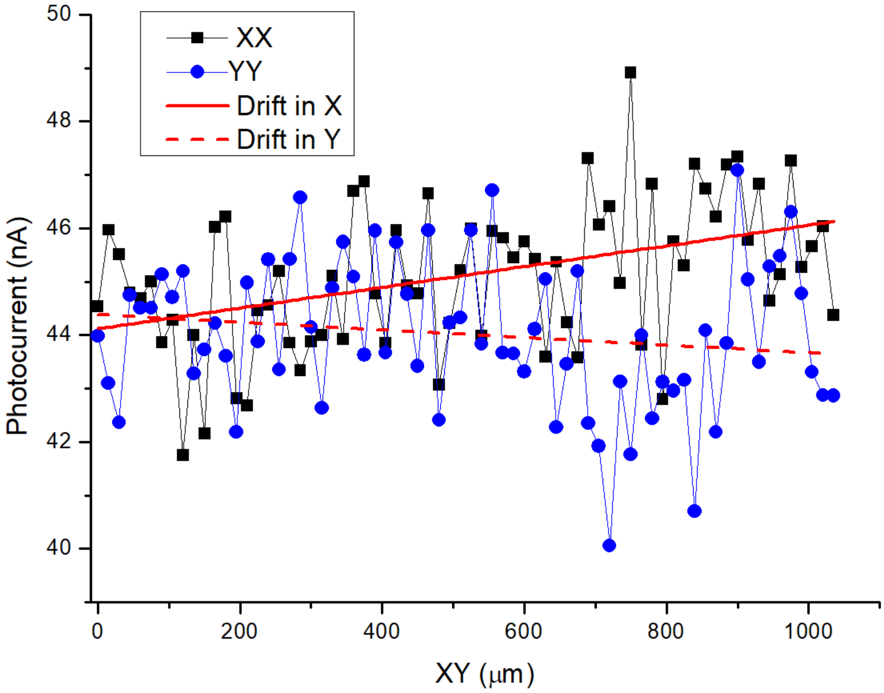

Figure 6.15: Drift in the background photocurrent in the X and Y directions of figure 6.14

background mean is significantly more that the drift in Y and should not affect results when using this measurement during the analysis. However the drift in X is larger than the standard deviation indicating that the results could be affected when using this background for photocurrent enhancement comparisons. Across the 200$\mu$m of one light trapping array the drift is only 0.38nA in X and 0.14 in Y. Which as can be seen from the collected results in table 6.3 is significantly less than the standard deviations in the light trapping regions of the DSSCs and should not affect results. To mitigate the effects of the drift in X higher resolution photocurrent maps can be taken of the light trapping structures and compared with their immediate planar background and their enhancement calculated. Results to follow will present these higher resolution photocurrent maps where the x20 microscope objective is used to focus the laser spot to $\sim 5\mu m$ and measurements are made every $5\mu m$ over an area of $250\mu m^2$, resulting in 2,500 individual measurements. Over $250\mu m$ the drift in X is 0.48nA and drift in Y is 0.18nA which is too small to affect our results. These higher resolution maps should both mitigate the effects of the drift in X on the photocurrent background seen in figure 6.14 and give us more precision when determining enhancement, as they will be only compared with local photocurrent conditions. The greater number of measurements made in the light trapping areas in these maps should also improve precision when determining our mean photocurrent across the light trapping arrays.

| Position | Mean Photocurrent (nA) | Enhancement (%) |
|---|---|---|
| Background | 44.66 ($s = 1.70$, $N = 3,439$) | N/A |
| 1 | 45.25 ($s = 1.49$, $N = 177$) | 1.31 (CI = 0.73, 1.89) |
| 2 | 45.80 ($s = 1.97$, $N = 177$) | 2.56 (CI = 1.98, 3.14) |
| 3 | 47.26 ($s = 1.69$, $N = 177$) | 5.83 (CI = 5.23, 6.39) |
| 4 | 46.41 ($s = 2.17$, $N = 177$) | 3.93 (CI = 3.35, 4.52) |
| 5 | 46.79 ($s = 1.60$, $N = 177$) | 4.75 (CI = 4.19, 5.35) |
| 6 | 46.64 ($s = 1.72$, $N = 177$) | 4.44 (CI = 3.85, 5.00) |
| 7 | 46.39 ($s = 1.88$, $N = 177$) | 3.88 (CI = 3.29, 4.45) |
| 8 | 46.81 ($s = 1.87$, $N = 177$) | 4.83 (CI = 4.25, 5.37) |

Table 6.3: Table showing mean photocurrent for background and light trapping arrays in positions 1-8 in figure 6.14 using data from this map.

These higher resolution maps are presented in figures 6.16 and 6.17 for light trapping arrays in positions numbered 3, 4, 7 and 8 in figure 6.14b. Results for the remaining positions alongside the ones presented in these figures can be seen in table 6.4. These areas were selected for presentation as they have a variety of different structure qualities over a number of different positions across the device.

Higher resolution photocurrent maps of the arrays in position 3 and 4 in figure are shown in figure 6.16a and c respectively. Figure 6.16b shows the SEM image corresponding with a, and 6.16d shows an optical image that corresponds with 6.16c. Graphically the figures suggest enhancement in photocurrent over the light trapping arrays when compared to the surrounding non-patterned planar $TiO_2$. However as could also be seen in the low resolution map, the enhancement in both these photocurrent maps is not uniform across the patterned area.

In figure 6.16a the mean background photocurrent is 51.57nA ($s$ = 3.10nA, $N$ = 900) and the mean photocurrent across the whole light trapping array is 55.37nA ($s$ = 2.98nA, $N$ = 1600) a difference of 3.79nA (CI = 3.54nA, 4.05nA) or an enhancement of 7.37% (CI = 6.88%, 7.86%). The corresponding SEM image seen in 6.16b shows some non-uniformity in stamped pyramid structures, with the areas towards the outside of the array, especially towards the top, not being as well patterned as the centre. This is reflected in the photocurrent map where the enhancement is seen in an area less than the 200µm$^2$ patterned region in the SEM images. If only these high quality area of the light trapping array are considered at enhancement could rise up to ∼ 15% from the background. It is worth noting that the SEM image and the photocurrent map are not perfectly orientated with the SEM image being at a slight angle when compared to the map, so care must be taken when comparing them directly.

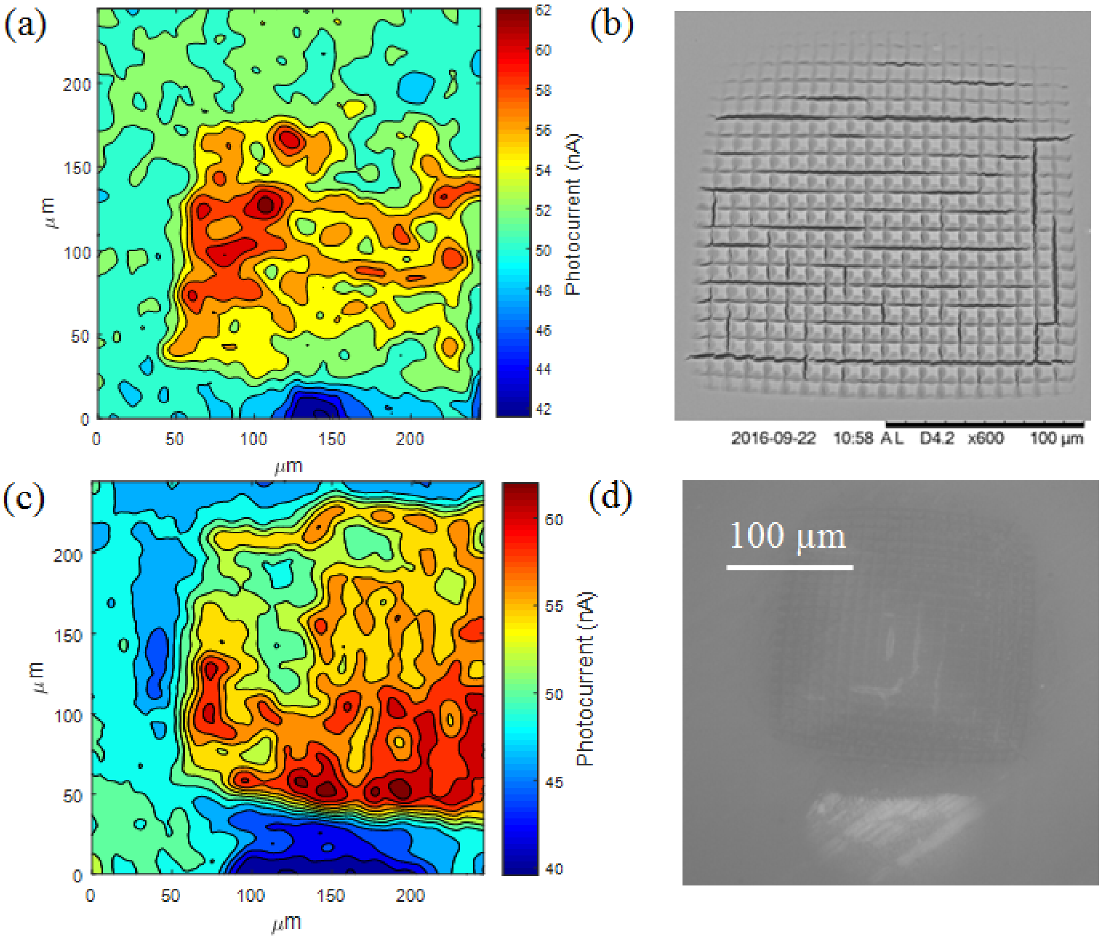

Figure 6.16: (a) Higher resolution photocurrent map and (b) SEM image of light trapping array in positions 3 in figure 6.14b. (c) Higher resolution photocurrent map and (d) SEM image of light trapping array in position 4 in figure 6.14b.

Before looking more closely at the second example, shown in figure 6.16c, one area should be highlighted. Just below the array in position 4 it can be seen in the optical image (figure 6.16b) there is mark, which leads to a significant drop in photocurrent in the corresponding map. This is likely to be sub surface damage leading to a deformation in the planer $TiO_2$ as it could not resolved in SEM images of this area. In this example the enhancement in the photocurrent extends over the whole 200µm$^2$ array. Here the pattern is stamped more successfully over the whole array accounting for the difference in size of the area where we see photocurrent enhancement. The enhancement over the background in this example is larger than in 6.16a, although this is in part due to the much lower background photocurrent from the defect in the planar $TiO_2$. In this example the mean background photocurrent is 48.95nA ($s$ = 2.39nA, $N$ = 900) and the mean photocurrent from the whole light trapping array is 53.31nA ($s$ = 3.74nA, $N$ = 1600) a difference of 4.36nA (CI = 4.12nA, 4.60nA) or an enhancement of 8.92% (CI = 8.43%, 9.41%). Again the enhancement in photocurrent generation is greater if only the highest quality areas of the array are considered. Comparing the peaks of both photocurrent maps we can see a similar value of ∼62nA. Both the SEM image and the optical image show some cracking in both samples incurred during sintering, which could help to account for the non-uniformity of the enhancement in the centre of the patterned areas. Again, the cracks seen in the corresponding SEM and optical image do, in some regions, have a positive effect on the photocurrent enhancement and in other regions a negative ones. However these cracks cannot alone account for the enhancement seen there as the region with the highest photocurrent enhancement in figure 6.16c, towards the bottom of the array, there are no cracks seen. Cracking and defects in DSSCs and their characterisation via SPCM will be considered in more detail later in the chapter. Again note the optical image in this example is slightly zoomed out from the map and has more space towards the bottom to show the defect in the planer $TiO_2$ more clearly, and therefore they do not perfectly overlap.

Figure 6.17 contains higher resolution photocurrent maps in 6.17a and 6.17c of positions 7 and 8 respectively. First we will discuss figure 6.17a and the corresponding SEM image seen in 6.17b, or position 7. The mean background photocurrent is 50.51nA ($s$ = 1.92nA, $N$ = 900) and the mean photocurrent from the whole light trapping array is 54.31nA ($s$ = 2.93nA, $N$ = 1600) a difference of 3.80nA (CI = 3.62nA, 3.98nA) or an enhancement of 7.52% (CI = 7.18%, 7.86%). Again when comparing the map and SEM image we see that the large crack running across the array at the bottom seems to have a negative contribution to the photocurrent whilst others in the array either do not significantly contribute or have some positive contributions.

The final example from this cell is seen in figure 6.17c which shows enhancement in a much smaller area than the whole 200µm$^2$ patterned array, again this is likely due to insufficient stamping towards the edges of the array. The mean background

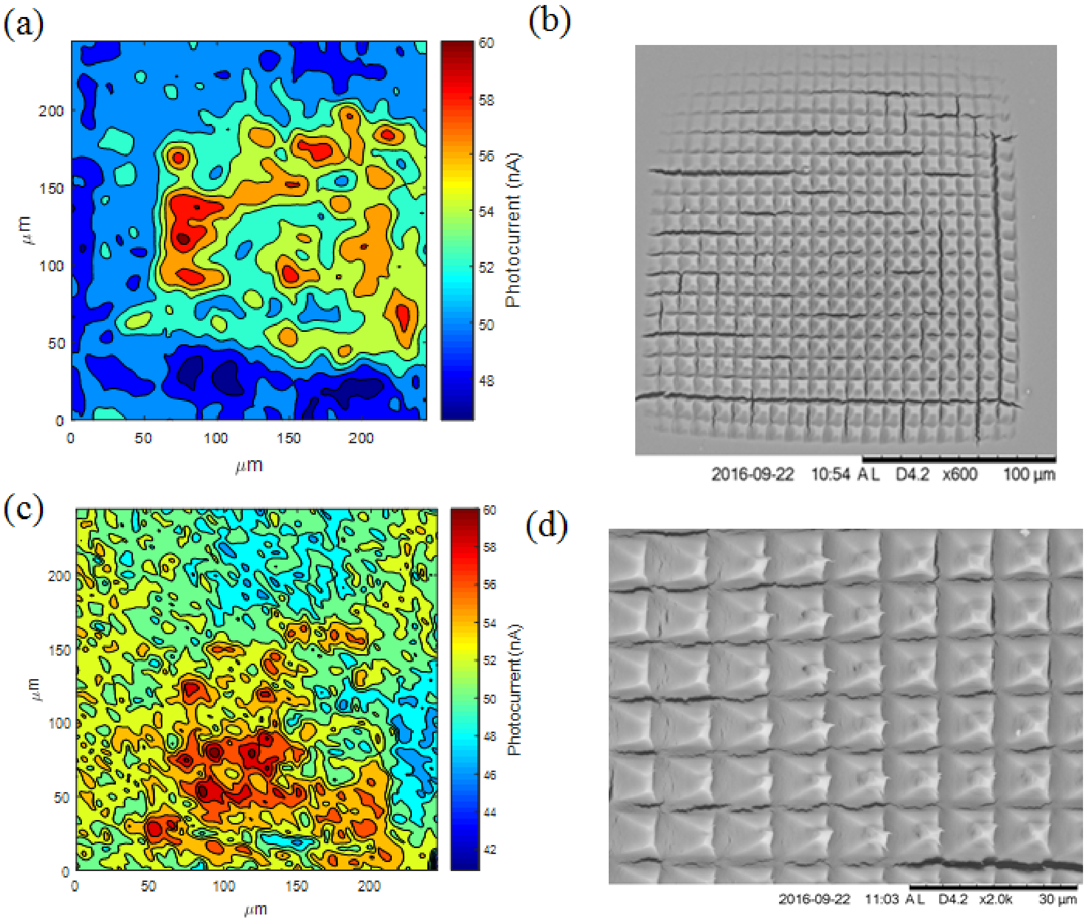

Figure 6.17: (a) Higher resolution photocurrent map and (b) SEM image of light trapping array in position 7 in figure 6.14b. (c) Higher resolution photocurrent map and (d) SEM image of light trapping array in position 8 in figure 6.14b.

photocurrent is 51.43nA ($s = 2.11$nA, $N = 900$) and the mean photocurrent from the whole light trapping array is 53.49nA ($s = 2.69$nA, $N = 1600$) a difference of 2.05nA (CI = 1.88nA, 2.23nA) or an enhancement of 3.99% (CI = 3.64%, 4.34%). The area of highest enhancement in the map is seen in the higher resolution SEM image in figure 6.17b where we find good quality whole pyramid structures in the array. Focusing on just this area the enhancements rise to up to $\sim$ 10%. We also see some small amount of cracking in-between these structures which do not seem to have any negative contributions to the photocurrent. The larger crack towards the bottom right of the SEM image overlaps with some of the horizontal strip where there is a drop in photocurrent towards the bottom of map, from $x \sim 75 - 150$µm.

| Position | Background photocurrent (nA), $N = 900$ | Light trapping photocurrent (nA), $N = 1600$ | Enhancement (%) |
|---|---|---|---|
| 1 | 49.78 ($s = 1.72$) | 52.57 ($s = 3.32$) | 6.14 (CI = 5.68, 6.60) |
| 2 | 50.47 ($s = 2.12$) | 52.89 ($s = 3.34$) | 4.19 (CI = 3.69, 4.69) |
| 3 | 51.57 ($s = 3.10$) | 55.37 ($s = 2.98$) | 7.37 (CI = 6.88, 7.86) |
| 4 | 48.95 ($s = 2.39$) | 53.31 ($s = 3.74$) | 8.92 (CI = 8.43, 9.41) |
| 5 | 50.89 ($s = 2.36$) | 53.95 ($s = 2.52$) | 5.99 (CI = 5.60, 6.38) |
| 6 | 51.11 ($s = 2.57$) | 54.12 ($s = 3.21$) | 5.89 (CI = 5.40, 6.38) |
| 7 | 50.51 ($s = 1.92$) | 54.31 ($s = 2.93$) | 7.52 (CI = 7.18, 7.86) |
| 8 | 51.43 ($s = 2.11$) | 53.49 ($s = 2.69$) | 3.99 (CI = 3.64, 4.34) |

Table 6.4: Table showing mean background photocurrent, photocurrent from light trapping arrays and % enhancement. Using data from high resolution maps. Positions 1-8 in figure 6.14.

Table 6.4 collects results from these higher resolution maps, where it can be seen that we calculate higher photocurrent generation enhancements when using data from these higher resolution maps. We expect these higher resolution maps to be more precise for a number of reasons. First due to the mitigation of the effects of the drift in X, seen in figure 6.14 and 6.15. The comparison with only local photocurrent ensuring similar background conditions. And the much greater number of measurements made in the map over the light trapping regions ($N = 1600$). Note that the enhancement in position 4 may be inflated due to surrounding lower photocurrent from sub-surface defects in the background.

The next two examples in figures 6.18 and 6.19 are both taken from patterned areas of different devices referred to as cells 3 and 4 in table 6.5. The first photocurrent map can be seen in 6.18a with the corresponding optical image in 6.18b and SEM image in 6.18c. Graphically we see significant enhancement in the photocurrent in the patterned area of the cell. And we see some significant cracking, the largest crack towards the bottom left of the map can be seen in the SEM image, and more importantly in the optical image where we can see its extent goes beyond that which is observable in the SEM image but reflected in the photocurrent map. This large crack leads to a huge drop in photocurrent. On the other hand the many smaller cracks make either a positive or no contribution to the photocurrent enhancement. Excluding the large defect from the data analysis from both the background and the light trapping areas we get value of 49.06nA ($s = 1.81$nA, $N = 1035$) for the mean background photocurrent and 52.67nA ($s = 2.41$nA, $N =$

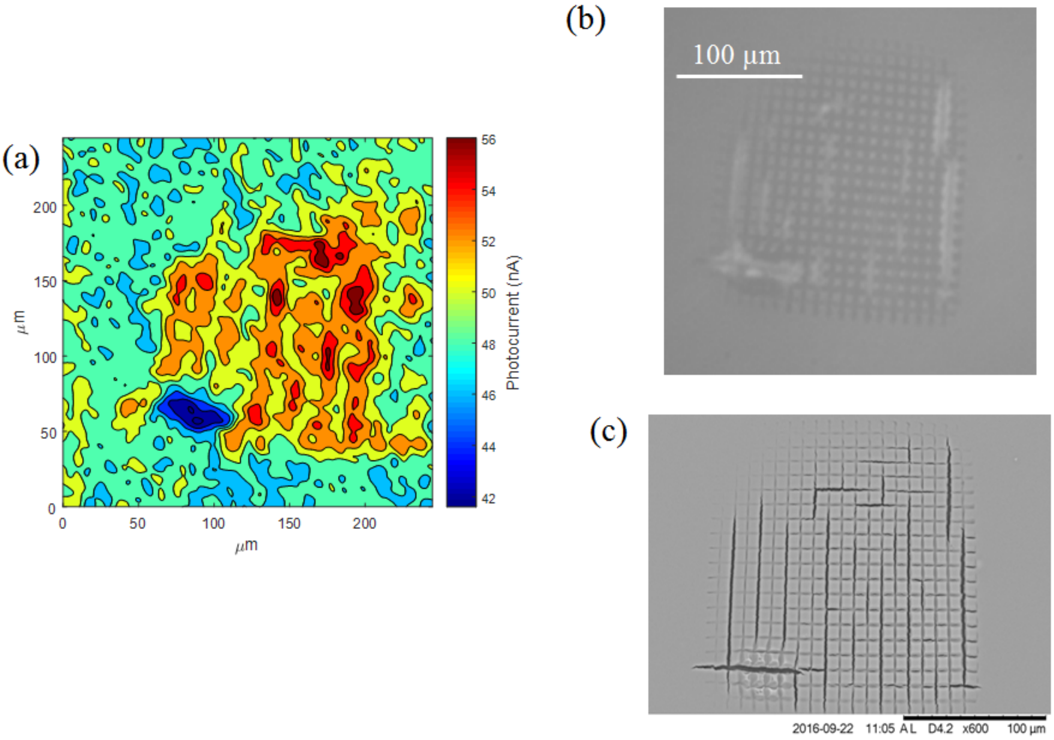

Figure 6.18: (a) Photocurrent map of light trapping array in DSSC. (b) Corresponding optical image. (c) Corresponding SEM images. Referred to as Cell 3 in table 6.5.

900) for the light trapping array. A difference of 3.61nA (CI = 3.41nA, 3.80nA) or an enhancement of 7.36% (CI = 6.95%, 7.77%).

The Final photocurrent map can be seen in 6.19a with corresponding SEM images in b and c. Here 6.19b shows the SEM image of the whole patterned area and 6.19c shows a higher resolution photocurrent map of the best quality area where the highest enhancement in photocurrent is seen. In this example we can see two large cracks running vertically and horizontally along the left hand-side and top of the patterned array. These cracks overlap with the lowest photocurrent regions seen in the map. Inside these cracks, further towards the centre of the array, is the area with the best stamped (figure 6.19c) and highest quality structures which overlap with the area of highest photocurrent enhancement seen in the map. Little or no enhancement is seen towards the bottom right of the array where we can see from the SEM image in 6.19b that the pattern has not been stamped deeply into the planar $TiO_2$. With the two cracks removed from the data analysis the mean background photocurrent is 19.44nA ($s$ = 2.49, $N$ = 900) and the mean

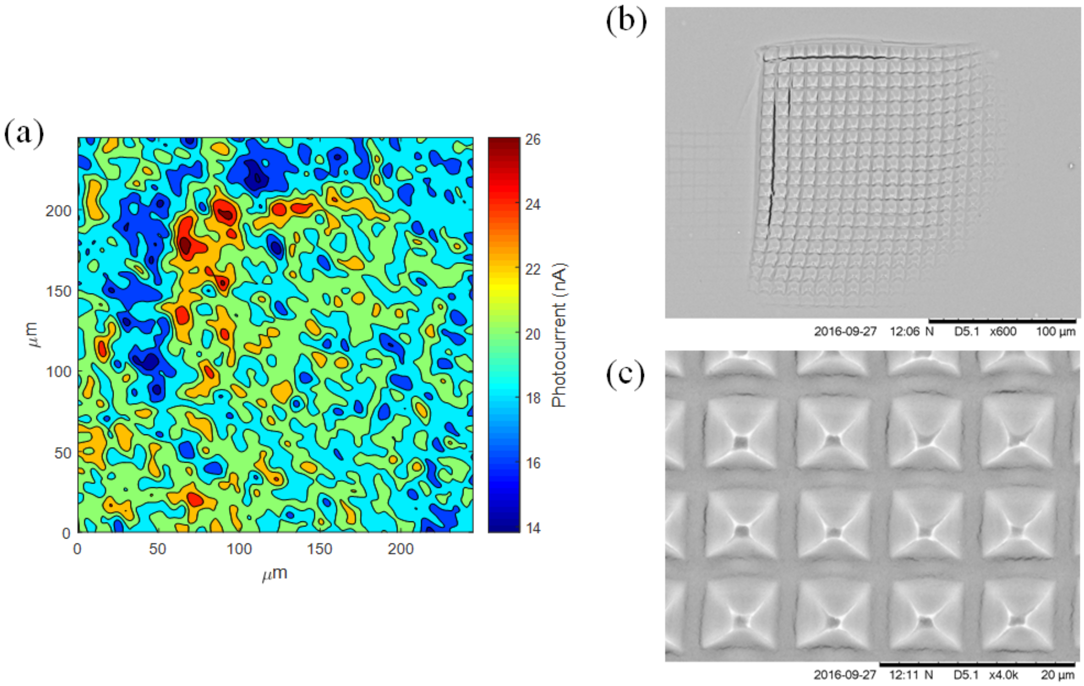

Figure 6.19: (a) Photocurrent map of light trapping array in DSSC. (b) SEM image showing whole array. (c) Higher resolution image. Referred to as Cell 4 in table 6.5.

photocurrent in the light trapping area is 20.49 ($s = 2.57$, $N = 1248$) a difference of 1.06nA (CI = 0.84nA, 1.28nA) or an enhancement of 5.05% (CI = 3.40%, 6.70%). The lower overall photocurrent in this example is due to electrolyte leakage from the cell, discovered after this map was taken and rendering the remaining structures on this device unsuitable for characterisation via SPCM.

Table 6.5 shows the collected results for mean background photocurrent, mean photocurrent over the light trapping arrays and % enhancement for all cells presented in this chapter. Cell 2 shows these values for all 8 individual areas containing light trapping structures, labelled positions 1-8 in figure 6.14 and using results from the high resolution maps ($\sim 5\mu$m). Note that the background photocurrent is taken from the immediate area around the light trapping structure and is not the photocurrent of the whole cell. The mean photocurrent enhancement from this collected data is 6.45% ($s = 1.65$%).

| Device | | Background PC (nA) | LT PC (nA) | % Enhancement (CI) |
|---|---|---|---|---|
| Cell 1 | | 30.71 ($s = 2.84$) | 33.74 ($s = 2.32$) | 8.56 (6.41, 10.71) |
| Cell 2 | 1 | 49.78 ($s = 1.72$) | 52.57 ($s = 3.32$) | 6.14 (5.68, 6.60) |
| | 2 | 50.47 ($s = 2.12$) | 52.89 ($s = 3.34$) | 4.19 (3.69, 4.69) |
| | 3 | 51.57 ($s = 3.10$) | 55.37 ($s = 2.98$) | 7.37 (6.88, 7.86) |
| | 4 | 48.95 ($s = 2.39$) | 53.31 ($s = 3.74$) | 8.92 (8.43, 9.41) |
| | 5 | 50.89 ($s = 2.36$) | 53.95 ($s = 2.52$) | 5.99 (5.60, 6.38) |
| | 6 | 51.11 ($s = 2.57$) | 54.12 ($s = 3.21$) | 5.89 (5.40, 6.38) |
| | 7 | 50.51 ($s = 1.92$) | 54.31 ($s = 2.93$) | 7.52 (7.18, 7.86) |
| | 8 | 51.43 ($s = 2.11$) | 53.49 ($s = 2.69$) | 3.99 (3.64, 4.34) |
| Cell 3 | | 49.06 ($s = 1.81$) | 52.67 ($s = 2.41$) | 7.36 (6.95, 7.77) |
| Cell 4 | | 19.44 ($s = 2.49$) | 20.49 ($s = 2.57$) | 5.05 (3.40, 6.70) |

Table 6.5: Table showing collected results for the 4 cells measured via SPCM in this chapter. For mean background photocurrent (PC), light trapping array mean photocurrents (LT PC) and % enhancement. Results from Cell 2 are all taken from the higher resolution photocurrent maps and in positions 1-8 in figure 6.14.

### 6.4.3 Defect detection and characterisation

We have already seen the SPCM technique's great ability to characterise DSSCs and light trapping DSSCs looking at selected areas of these cells at a wide range of resolutions. These features make this technique an excellent tool for detecting, locating and characterising defects and artefacts in the cell. We have already briefly discussed cracking and its effects on photocurrent generation in light trapping arrays, this section will look in more detail that these defects. Defects such as cracks can often be clearly seen in optical or SEM images of the cell, however this optical characterisation does not give us any information about how these cracks are affecting photocurrent generation in the cell. Using SPCM we get detailed high resolution photocurrent maps showing exactly how these cracks can degrade or even improve photocurrent generation (as seen in figure 6.20). Defects and artefacts are not always seen in optical or SEM imaging, since the artefact or damage could be below the surface of the cell. Again with SPCM these unseen artefacts do not present a problem and can be easily detected and characterised.

Figure 6.20 shows a photocurrent map of traditional un-patterned planar $TiO_2$ DSSC. The photocurrent map shown in 6.20a shows the whole ~6.5mm$^2$ active area of this cell. This map was taken with a x10 microscope objective giving a focused laser spot of $\sim$ 15µm when focused through the glass and measurements

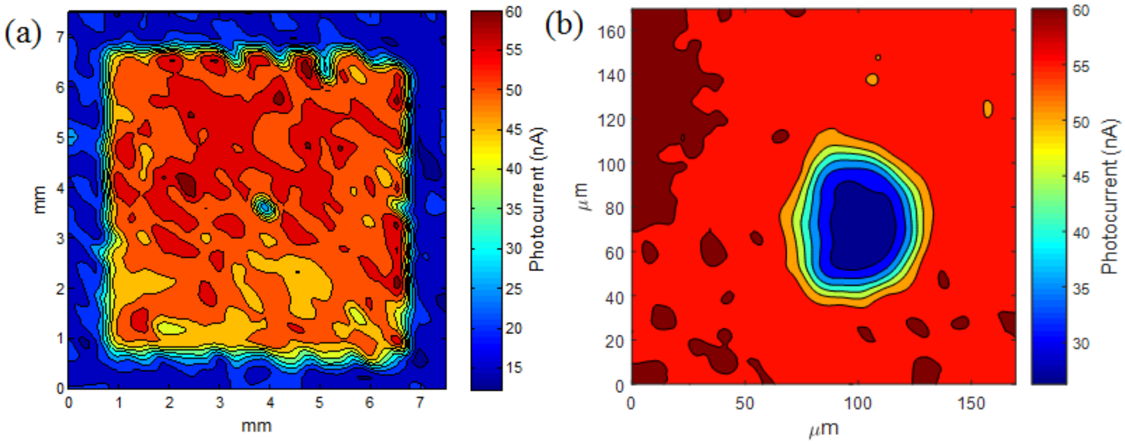

Figure 6.20: (a) Low resolution photocurrent map of active area of DSSC. (b) High resolution photocurrent map of defect in centre of same cell.

are taken every 300µm. In this device the mean photocurrent is 52.76nA ($s = 6.55$nA, $N = 400$). As with previous results presented there is some variation in the photocurrent generated across the planar $TiO_2$ device. However there is also a small region towards the centre of the cell where the photocurrent drops by approximately half of the mean photocurrent of the device. Figure 6.20b shows a higher resolution (5µm) photocurrent map of the artefact detected in the centre of this cell. At this higher resolution the nature of the defect can be seen in much greater detail, it shows the same drop in photocurrent to $\sim$ 30na in the centre of the defect, but it also reveals that the defect is actually much smaller than seen in 6.20a. Note that cell's surface was checked with an optical microscope for quality before SPCM measurements were made and no significant changes in the surface could be seen where this defect was detected.

Figure 6.21a shows the photocurrent map of a micro crack that can be seen in the corresponding SEM image in 6.21b. This photocurrent map, and the rest in this section, have measurements taken every 5µm with a laser spot diameter of $\sim$ 5µm. Here the crack has a negative effect on the photocurrent leading to a significant drop. Interestingly the negative impact on photocurrent extends beyond the physical area of the crack seen in the corresponding SEM image suggesting the damage extends below the surface. Figure 6.21c and 6.21d show the photocurrent map and the corresponding SEM image of another sample of planar $TiO_2$ respectively. Here, although no obvious features are visible in the SEM image there is a clear drop of current in the sample. The drop in current over this small area

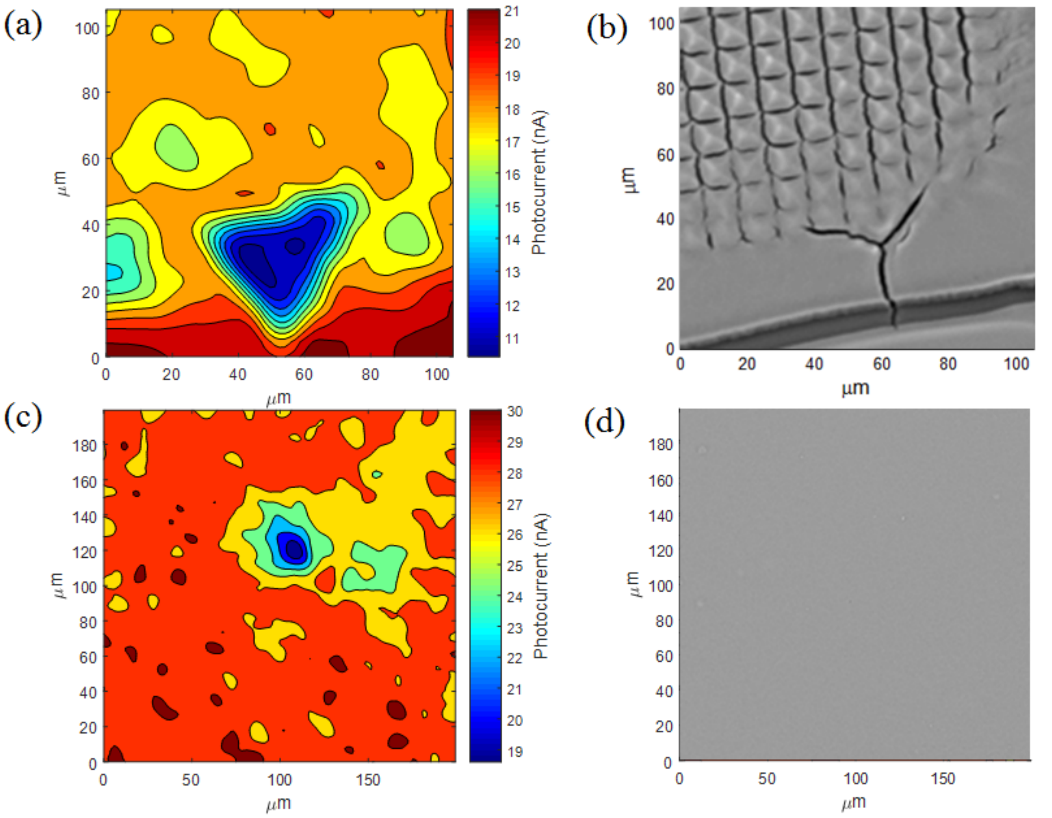

Figure 6.21: (a) Photocurrent map showing crack in $TiO_2$ electrode. (b) Corresponding SEM image. (c) Photocurrent map of hidden defect in $TiO_2$ electrode. (d) Corresponding SEM image.

is significantly larger than the smaller current variations across the rest of this sample. Again showing how effective this technique can be at detecting defects unseen in SEM and optical imaging.

These previous examples have shown how this technique can both detect and characterise defects. All of the defects and cracks in these examples have had an entirely negative effect on the photocurrent, however this is not always the case. Figure 6.22a shows a photocurrent map, with the corresponding SEM image shown in 6.22b, of a crack on a planar area of the cell which emanates in three directions from its centre. Here although there is a negative effect on the photocurrent in the centre, the three protruding arms all have a significant positive effect on photocurrent generation. With the overall contribution of the crack to photocurrent generation actually being positive. Again these effects, both negative and positive, extend beyond the extent of the crack seen in the SEM image.

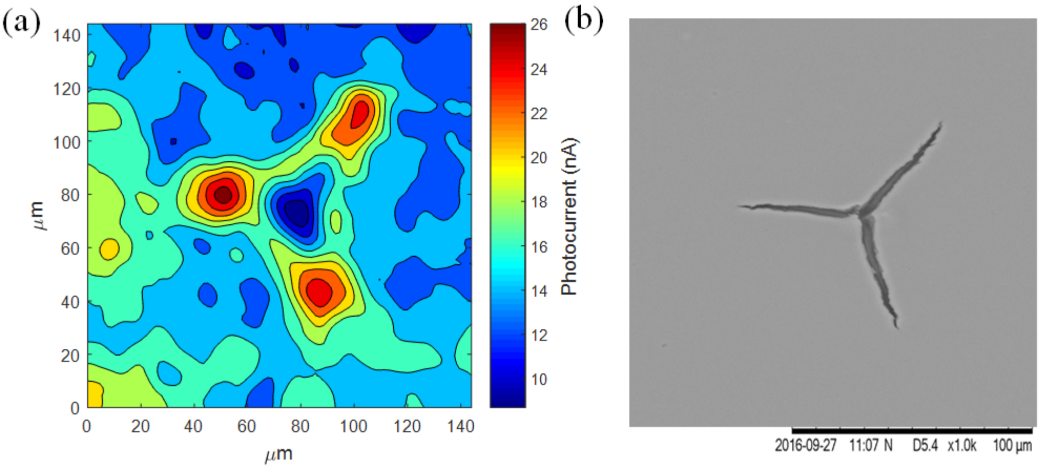

Figure 6.22: Crack in $TiO_2$ electrode and effects on photocurrent. (a) Photocurrent map. (b) Corresponding SEM Image.

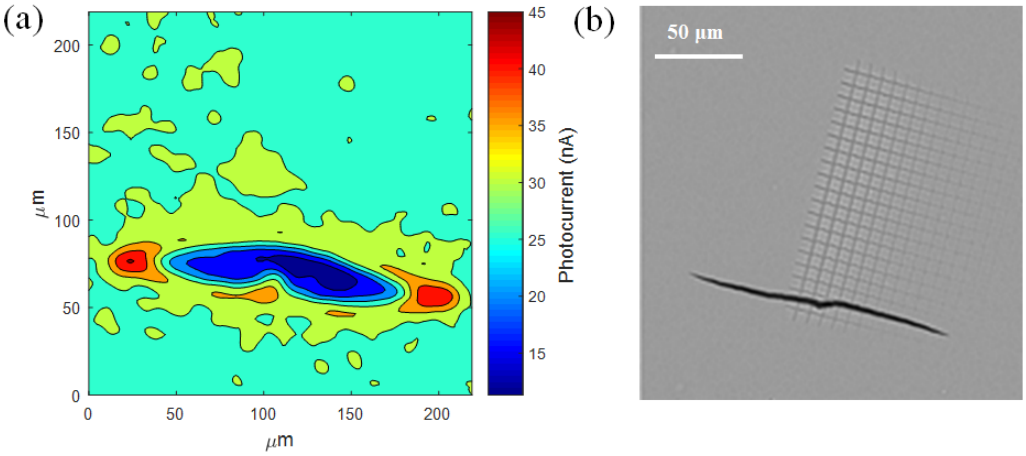

Figure 6.23: Crack in $TiO_2$ electrode and effects on photocurrent. (a) Photocurrent map (b) Corresponding SEM image.

Figure 6.23 shows a further example of the unexpected effects of this cracking on photocurrent generation in the cell. The photocurrent map is presented in figure 6.23a with the corresponding SEM image being shown in 6.23b. It can be seen in the SEM image that there is some patterning of this electrode. Higher resolution images showed that the stamping had not been effective at stamping our pyramidal light trapping design deep enough into the $TiO_2$, so it is not surprising that we do not see any significant improvement in the photocurrent in the patterned areas. In this example the crack has a more significant negative effect on photocurrent but it does also lead to some increases around the edges with the highest positive contribution coming from the two ends of the crack. Again these regions of higher and lower photocurrent, similar to figure 6.22, are proof that these defects are not necessarily bad for photocurrent generation in the cell. Here also the effects, both positive and negative, extend beyond the crack seen on the surface.

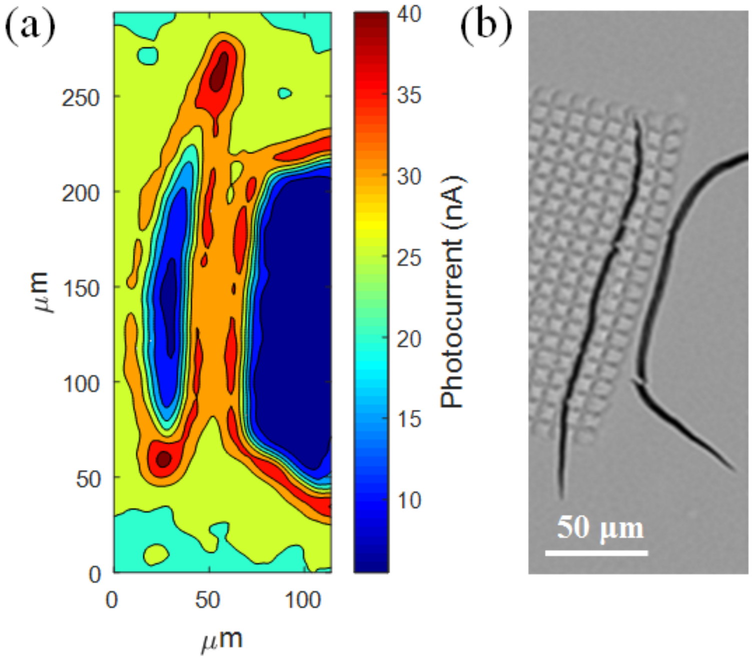

Figure 6.24: Crack in $TiO_2$ electrode and effects on photocurrent. (a) Photocurrent map. (b) Corresponding SEM image.

Another interesting example of these positive contributions to the photocurrent around the edges of the visible cracking along with more significant negative contributions is seen in the photocurrent map in figure 6.24a and the corresponding SEM image in 6.24b. Here, there is both a significant positive impact around the edges of these cracks, extending beyond the physical crack seen in the SEM image. But there is also a very substantial negative impact on the photocurrent seen beyond the right hand side of the cracks, which again appears flat in the SEM imaging. However in this case optical images did reveal some deformation in the surface not seen resolved in the SEM.

Finally figure 6.25a shows a photocurrent map of some cracks in a planar $TiO_2$ device and corresponding optical image seen in 6.25b. Here the only contribution from the cracks to the photocurrent is negative, with no positive contribution around the edges of the cracks. As can be seen in the optical image the effects of the cracks on the surface extends to a larger area than is seen in the previous SEM images, accounting for why we, in some cases, see the effects on the photocurrent extending beyond the cracks seen in the SEM images.

Essentially the cracking can lead to deformations on the surface extending around the crack which cannot be resolved with SEM but can optically. These areas are of interest because they seem to be able to lead to both positive and negative contributions to the photocurrent generation. Another interesting area here is the increased photocurrent towards the right hand side of the map, with no change being seen in the optical image, again showing the technique's ability to detect unseen artefacts. All of these examples help to highlight that physical defects and deformations can be complex with cracks not necessarily leading to a purely negative impact on the photocurrent. These figures show how effective this technique is at characterising not just visible defects such as cracks and to what extent they can affect the cell performance, but it also shows how this technique can be used to find and characterise defects that are hidden below the surface or unseen in traditional characterisation methods.

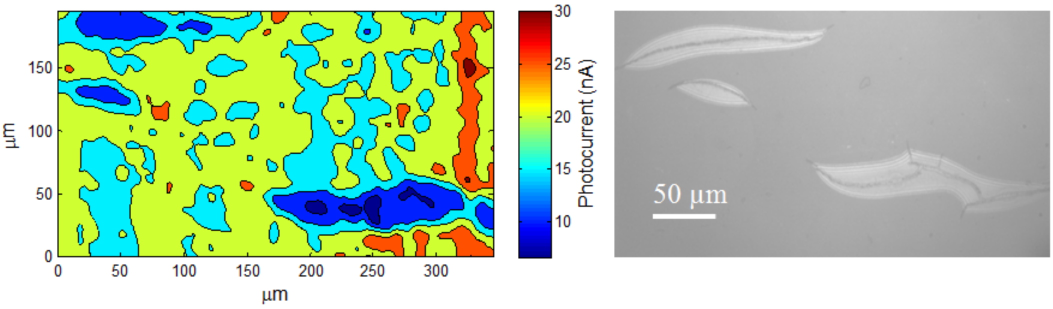

Figure 6.25: Crack in $TiO_2$ electrode and effects on photocurrent. (a) Photocurrent map. (b) Corresponding optical image.

## 6.5 Summary and conclusions

This chapter presents results for our ray-tracing simulations and SPCM experiments used to characterise our light trapping DSSCS. Ray-tracing simulations were used to study our light trapping designs across the solar spectrum, where they were shown to significantly increase absorption and photocurrent generation over planar DSSC devices. Further simulations studied a number of geometries differing from those physically fabricated and characterised via SPCM. First to see what effect the practical adaptations to our design (made to help facilitate fabrication) have on absorption. Then a number of pyramid structures of differing side wall angles were tested to again compare absorption enhancing effects.

The periodic pyramid patterned $TiO_2$ electrodes fabricated and characterised in this work were able to trap light incident to the cell to enhance the photocurrent generated when compared to planar regions of the sample cell. In this chapter, we have demonstrated that the 3D-printing of periodic sub-micron structures can enhance solar cell performance increasing photocurrent generation by up to $\sim 9\%$ with a mean enhancement of $\sim 6.5\%$. However as simulations and aspects of SPCM suggest greater enhancement could be achieved in future work. This will be discussed in more detail in the following chapters. Results presented here show that our DSSC patterning and fabrication procedure can reliably and reproducibly lead to significant photocurrent enhancement in the light trapping areas of the cell.

This chapter has shown how SPCM is an excellent technique for the characterisation of our light trapping designs in DSSCs. It has also proven to be very effective at detecting and characterising defects and artefacts on the cell's surface and importantly below the surface where they cannot seen by traditional characteristics methods such as optical and SEM imaging. All of the results presented here and their implications, with comparisons to similar work in the literature, along with further comment on our fabrication methods will be examined in more detail in the discussion chapter to follow.

# Chapter 7

# Discussion

The aim of this work is to develop a novel method for the fabrication of a variety of structures which can increase the light trapping properties of DSSCs, thereby increasing the amount of incident solar radiation absorbed, enhancing photocurrent generation and the overall efficiency of the device. DSSCs are a novel third generation device, which have significantly lower efficiencies than conventional photovoltaics and could benefit greatly from this enhanced performance. Our resulting light trapping arrays are able to show photocurrent generation enhancing effects of up to $\sim 9\%$ at a wavelength of 405nm. These structures are shown to reliably increase photocurrent in our devices with a mean enhancement of 6.45% ($s = 1.65\%$) across all measured arrays. When focusing on areas of only the highest structure quality, results suggest potential greater photocurrent enhancements than those presented here, indicating that further improvements of the method could results in increased performance gains.

This is achieved via the use of the TTP technique for the microfabrication of polymer stamps or templates, which are used to pattern the light trapping structures into a planar $TiO_2$ nanoparticle thin film, the active layer of a DSSC device. The method is developed and optimised to increase the reliability and quality of the resulting light trapping structured DSSC devices. The effectiveness of the structures performance enhancing effects is evaluated using a SPCM technique. Whilst there is much work done into light trapping in DSSC and solar cell research in general. The development of this novel fabrication technique is important as it potentially allows unprecedented levels of control over the structures geometries which are difficult to achieve using more traditional patterning methods. Whilst there is only one structure geometry fabricated and tested in this pilot study, in principle these methods could be applied to the fabrication of structures of arbitrary geometries.

Results from simulations show 16% more total light absorbed at 405nm or a 22% enhancement in absorption for our light trapping structures over a planar control. This can be considered a 22% enhancement in photocurrent generation assuming internal quantum efficiency of 100%, or in other words the maximum possible limit for photocurrent enhancement in our experimental results. In reality of course recombination in the dye molecules, recombination from the conduction band of the semiconductor with holes in the HOMO of the dye and recombination from the conduction band of the semiconductor with acceptors in the electrolyte all act to reduce efficiency in the device. Even with these unfavourable processes involved, the simulations suggest that photocurrent enhancements in the experimental results could be improved, getting closer to this 22% limit. This is backed up somewhat in aspects of our experimental results, when focusing on the regions of only the highest quality results suggest photocurrent enhancement could rise up $\sim$ 15%. However further work would be needed before this could be conclusively determined.

The use of pyramidal patterns for light trapping Si solar cells is widely reported in the literature to show significant performance enhancing effects [50, 61, 75]. Reports of light trapping pyramidal patterns for use in DSSCs or similar devices are less common, however several studies similar to ours have been conducted. Labelle *et al.* [88] present a combined experimental and theoretical study for their QDSC using pyramidal structures and PbS QD sensitisers. This group used the same pyramid geometries used in this work and were able to show improvements in short-circuit current density of 24%. Whilst results cannot be compared directly, due to the different device architecture and sensitisers used, it shows the potential of these simple structures to greatly improve the performance of similar devices. Wooh *et al.* [192] report a pyramidal structured DSSCs patterned using a soft-molding method, which is a type of soft-lithography technique, they also using the same dye as in this study, N719. In this work enhancement of $\sim$ 20% in absorption at 405nm and enhancement of $\sim$ 20% in photocurrent generation across the AM 1.5 solar spectrum are recorded. Jieng *et al.* [184] also report measurements from pyramidal structured DSSCs using the dye N719 for sensitisation. Here enhancement in absorption of $\sim$ 20% is seen, similar to those seen in our numerical simulations. And overall photocurrent density enhancements of $\sim 16\%$ over the AM 1.5 solar spectrum are recorded. This work also shows that this pyramidal layer combined with the conventional larger nanoparticle scattering layer used in conventional DSSCs is significantly better for performance than the light scattering layer alone. Although care should be taken when comparing these results directly with ours, due to the different wavelengths and characterisation techniques used to probe cell performance, these reports together with ours show the reliable and significant performance enhancing effects of mirco-pyramid patterned DSSCs over planar counterparts.

Before moving on to some of the other significant results in this work some of the limitations of this study should be discussed. There are a number which could be encompassed in the scope of future wok. Such as the limited number of patterned arrays measured in this work. Since much of the time of this project was spend in developing stamp fabrication and the electrode patterning methods, successful patterning and measurement was only available towards the end of the study. With the fabrication of a greater number of patterned devices more measurements could be made, increasing confidence in our findings. Another is the only single pyramid geometry measured here, now the fabrication method is established the work could easily be expanded to the study a greater number of structures. Finally there is one limitation to the study which could not be overcome in future work, since it is an intrinsic property of the TPP microfabrication technique. This is that the scale of and speed of fabrication make this technique currently impractical to be scaled up for commercial solar cell applications. However the potentially unprecedented speeds at which a greater number of designs could be patterned and tested is a great advantages over other techniques. Because of this great ability to rapid prototype on the micro scale, this technique should be thought of as an investigative tool aiding the determination of the best possible light trapping structures for use in DSSCs. A use for which this work could also have implications in the wider study of numerous optoelectronic devices.

Ray-tracing simulation results suggests that although our structures are only characterised at one wavelength of 405nm they should have excellent absorption and photocurrent generation enhancing effects across the AM 1.5 solar spectrum. A number of different pyramidal geometries are tested using these methods, with pyramid side wall angles of $40^{\circ}$ showing the best performance. However, in this work pyramidal side wall angles of $54.7^{\circ}$ are chosen for fabrication they are shown to absorb only a few percent less incident light and are better compared with reports in the literature. The significant variation in the performance of these (only slightly) different structure geometries show the importance of theoretical work in aiding light trapping design. This work is also able to help quantity the effects that our practical adaptations (made to help facilitate fabrication) would have on their end performance. These adaptations are shown to decrease the total light absorbed by up to 10% at shorter wavelengths although at longer wavelengths this difference is not as large, again showing further improvements of the fabrication techniques could result in greater performance enhancing effects.

Our results for planar electrodes agree well with experimental results of DSSCs using the dye N719 [178, 20]. Our results also show excellent agreement with a combined experimental and theoretical work studying pyramidal arrays in DSSCs using the same dye N719 [192]. Further experimental work into devices of similar cell geometries using the dye N719 [183] are in good agreement with the results presented here, all helping to validate our model. As mentioned our devices are only measured experimentally at 405nm however these reports along with results from our simulations indicate the structures ability to outperform planar devices across the AM 1.5 solar spectrum.

Other interesting results are those showing the effects of cracks and defects in photocurrent generation in DSSCs, which are characterised excellently with the SPCM technique. Which is able to characterise, in detail, any cracks and defects visible in optical and SEM imaging and their effects on photocurrent generation. It also able to detect and characterise defects or artefacts unseen by these traditional imaging techniques, such as sub-surface damage. Results show that whilst one would intuitively expect cracks to significantly affect photocurrent generation in a negative manner this is not always the case. Whilst there are indeed always negative contributions from these cracks there can also be, unexpectedly, significant positive contributions, and in one case an overall positive contribution is seen in one of these cracks. These results show that SPCM is a powerful tool for the investigation of defects and artefacts in DSSCs and by extension many other semiconductor devices or optoelectronic devices which could find this type analysis useful.

Much research has been done into the formation of micro-cracks in crystalline silicon solar cells and how these cracks affect the cell's electrical and optical properties

[193]. However, it is difficult to get a full picture of how these defects affect cell performance. Cracking in the active layer does not necessarily lead to an initial strong reduction of the cell's output power [194] but they do lead to lower cell stability leading to a reduction of the performance of the cell over time [195]. There is evidence for heavy cracking on the mm scale leading to an introduction of new recombination centres that lead to a subsequent reduction in cell performances [196].

Whist detailed studies of the localisation and characterisation of specific cracks and defects in DSSCs are rare, much care is taken during the fabrication of high performance DSSCs to reduce cracking in the $TiO_2$ to a minimum [197]. When a variety of different $TiO_2$ nanoparticle pastes are studied, pastes which lead to a surface that is heavily populated with micro-cracks has been shown to perform significantly worse than electrodes with smooth surfaces [198]. The bending of $TiO_2$ electrodes in flexible DSSCs tests leads to increased cracking and decreased cell efficiency with increasing number of bends [199], with this reduction being attributed to the decline of the short circuit current from the increased electron transport resistance, and to decreased electron collection efficiency. SPCM has also been used to study intentionally induced defects of cracks on the millimetre scale. These large cracks all lead to significant drops in photocurrent performance [142].

That these defects and cracks in the cell surface can lead to both positive and negative contributions to photocurrent generation is fascinating and largely unexplored in the DSSCs literature. There are several physical processes responsible for photocurrent generation. The two most important being light absorption and transport of photogenerated carriers. One possible explanation for why we see both positive and negative contribution in these defects/cracks is that they might improve light trapping increasing absorption but quench electron transport, or vice versa. For further insight into the mechanisms which cause these positive and negative contributions to photocurrent generation an in depth study of theses interesting phenomena are required.

Finally, as already touched upon, this discussion raises some interesting points which could be the focus of further research. We will next turn to some of this potential future work, and briefly examine some of the possible strategies by which it could be conducted.

# Chapter 8

# Future Work

There are many avenues to explore for future research building on the work presented in this thesis. The next logical step for immediate further work would be to continue improvements of the stamping method for $TiO_2$ electrode patterning. Whilst the current method can reliably produce photocurrent enhancing light trapping arrays they show some significant variation in performance across the array. This is reflected by the inhomogeneous quality of the arrays seen via SEM and optical imaging. Our results suggest, as one would expect, that the higher quality regions have better performance enhancing effects, therefore improving the quality of our light trapping arrays should further increase photocurrent enhancement.

Another first step for future work would be to develop and fabricate a number of different light trapping designs to be patterned onto the same device allowing for their direct comparison and ensuring local conditions are as similar as possible. This could start with the different pyramidal geometries looked at in the ray-tracing simulations in this work, and comparing these experimental and theoretical results. Utilising SPCM these different light trapping structures can be experimentally tested to see which has the best photocurrent performance enhancing effects. Since DSSCs are complex devices with various mechanisms contributing to photocurrent generation theoretical work alone may not be enough to determine the best performing structures. Our method of fabrication (via TPP) and characterisation (via SPCM) is perfect for the experimental testing of various optimised light trapping designs. This rapid prototyping on the micron and sub-micron scale is impossible with many other microfabrication techniques previously used for the development of light trapping DSSCs.

Future structure design can be aided by the expansion of the theoretical simulations of light trapping designs for DSSC presented in chapter 6. In this pilot study only periodic pyramidal microstructures were used patterned into $TiO_2$ electrodes. We limited ourselves to these basic designs, in part, because there is little theoretical work done into more complex designs. Previous work has been constrained by established fabrication methods such as the use of self-assembly of latex spheres [84], or multi-beam interference lithography to make polymer templates [200]. While these techniques are both able to create complex structures, close control over precise geometry is impossible. However, using TPP any arbitrary negative polymer structure, with a resolution approaching the nanoscale, can be produced. The $TiO_2$ nanoparticles can then be infiltrated into the template, much like some of the examples in chapter 3, before being removed via calcination, freeing designers to find the best light trapping structures. For the realisation of these more complex structures this more advanced method for electrode patterning is required. Whilst the stamping technique is sufficient for our pyramidal arrays it is inadequate for structures with complex internal 3D geometries. Another interesting idea to explore these more advanced light trapping $TiO_2$ fabrication techniques is that with some modification the TPP system used here could be adapted for the printing of polymer templates directly onto the transparent conducting oxide, thus reducing the number of steps for fabrication, and potentially improving final structure quality.

The results of this research have also raised some interesting questions regarding the nature of cracks and defects in DSSCs with cracks showing both positive and negative contributions to photocurrent generation. A further more detailed study of these cracks could be compelling and may help to definitively reveal the mechanisms behind this complex relationship between cracking in the $TiO_2$ surface and the photocurrent generation. Another interesting result which could lead to an engaging physical study is the seeming increase in photocurrent generation with the greater power density of laser illumination in SPCM. Again further work in this area could conclusively determine the mechanisms behind these observations.

# Chapter 9

# Summary and conclusions

This work demonstrates a flexible and novel 3D-printing method for the fabrication of DSSC based on pyramidal periodic micron structures. Our structures are shown to produce significant enhancement of the DSSC performance. Photocurrent enhancements of up to $\sim 9\%$ across the whole patterned array are recorded, including areas with significantly lower structure quality. We also demonstrated 3D printing of large scale $1\text{mm}^2$ area of DSSCs which contain several regions with individually designed periodic systems of microscopic light-trapping structures. This work was also able to show the effectiveness of the developed SPCM technique in the mapping of local DSSC photocurrents with sub-micron resolution on large scale (>1cm) devices. This project shows the successful integration of the state-of-the-art Engineering (sub-micron 3D printing) and Physics (advanced photocurrent microscopy).

The most important experimental results of this work are presented in chapter 6 where we are able to show reliable and significant photocurrent enhancing effects from our light trapping DSSCs using SPCM. Mean enhancements of up to $\sim 9\%$ in photocurrent are recorded at a wavelength of 405nm, this enhancement includes areas where the patterns were not well stamped into the electrode. This technique also proved incredibly effective at the detection and/or characterisation of defects and artefacts in our DSSC electrodes. Artefacts and defects below the surface of the $TiO_2$ which cannot be seen in either optical or SEM imaging are easily spotted in these photocurrent maps. The technique also shows that some cracks/defects have effects on the photocurrent that extend well beyond the physical area seen in SEM and optical images. Interesting results are seen when SPCM is used to look in more detail at cracks in the $TiO_2$ surface. Unexpectedly these cracks were shown, in some instances, to have both positive and negative contributions to photocurrent generation. A further more detailed study of these cracks could be compelling and may help to reveal the mechanisms behind this complex relationship between cracking in the $TiO_2$ surface and the photocurrent generation.

The results chapter also demonstrates conventional characterisation methods for traditional planar $TiO_2$ DSSCs. Results from some planer $TiO_2$ test cells are shown as examples of these traditional techniques. Whilst these methods are excellent for the characterisation of the overall performance of the cells, they are, unlike our SPCM technique, not tailored to specifically look at the effectiveness of different light trapping structures. Simulation results, also presented in this chapter, indicate that our light trapping designs have impressive absorption and photocurrent generation properties across the AM1.5 solar spectrum. A number of structures of differing pyramid geometries are also studied in these simulations. These help to quantify the losses in enhancement we should expect from our practical adaptations made to the structure design, to aid quality fabrication.

The thesis begins with an introduction to DSSCs, which aims to give the reader a general understanding of the operating principles and current state of research in the DSSC community. Chapter 3 moves on to explore light trapping in solar cell devices focusing on light trapping in the DSSC. Chapter 4 introduces the micron/sub-micron scale fabrication technique TPP, which is utilised in this work for the fabrication of our polymer stamps. The complete methodology for the work is presented in chapter 5, where ray-tracing simulations, characterisation techniques and fabrication methods are described. The chapter first introduces our methods and a model description for the ray tracing simulations before moving on to look in detail at the various characterisation techniques used in this work, including optical and SEM imaging, EDX elemental analysis, tradition solar cells characterisation and SPCM mapping. The SPCM is looked at in greater detail as it is the technique used to analyse photocurrent enhancement in our light trapping DSSCs. Some background on the technique is given before showing some examples of its applications for the characterisation of micron/sub-micron features of DSSCs, solar cells in general and other semiconductor devices before our experimental set-up is detailed.

Next the experimental method for the novel microfabrication technique TPP is detailed alongside some additional comments on our light trapping structure design. Some examples of the resulting polymer stamps and of other possible microstructures are showcased here via SEM imaging. These examples are able to show unprecedented levels of control over the fabrication of micron and sub-micron light trapping structures that can be achieved via TPP. The procedure, and its development, for the patterning of planer $TiO_2$ electrodes with these polymer stamps is next outlined. Final structure quality is assessed with optical and SEM imaging. EDX elemental analysis is able to show that the sintering of the $TiO_2$ after patterning is able to completely remove the stamps and any other organic contaminates left on the electrodes. To produce high quality structures reliably careful control of the patterning procedure must be maintained throughout. With the electrodes patterned, they are now used in the fabrication of DSSCs. This fabrication procedure is described next, which contains details of $TiO_2$ sensitisation, the preparation of the counter electrodes and final cell assembly.

To conclude, this work aimed to develop methods for the microfabrication of light trapping structures for DSSCs, a novel third generation solar cells device which could benefit greatly from enhanced performance. This problem was tackled with the use of the novel 3D printing technique TPP, which was used to fabricate polymer microstructure stamps, which were subsequently used to pattern $TiO_2$ electrodes. Light trapping arrays within assembled devices were then tested for performance enhancing effects with SPCM.

This project has demonstrated the novel 3D printing of sub-micron light trapping structures used in DSSCs. Even a pilot series using simple pyramidal structures was able to achieve photocurrent enhancement of up to $\sim 9\%$, including areas where the patterns were not well stamped. Focusing on the best regions results indicate this enhancement could rise up $\sim 15\%$, however future work would be needed to show this conclusively. Results compare well with reports using structures of similar geometries and a similar stamping technique in DSSCs devices using the dye N719 [184, 192]. Further developments of the stamping technique (to realise more complex and better light trapping designs), improvements of the $TiO_2$ film quality (reducing the number of cracks and imperfections) and theoretical modelling of 3D-light trapping microstructures to optimise design, will all lead to further enhancement of device performance.

# Appendix A

# Appendix

## A.1 Materials data used in ray-trace simulations

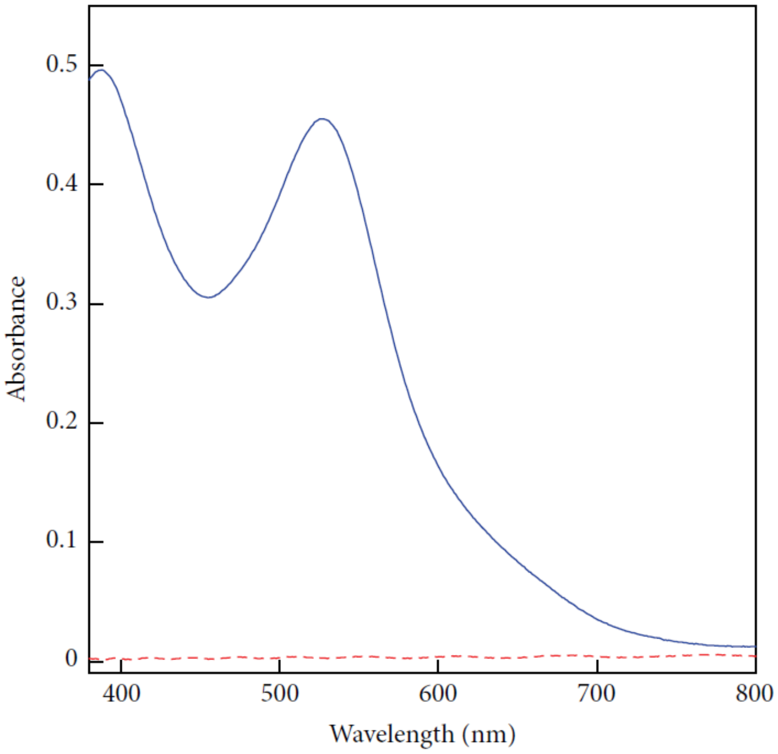

Figure A.1: $TiO_2$ + N719 absorbance data [178].

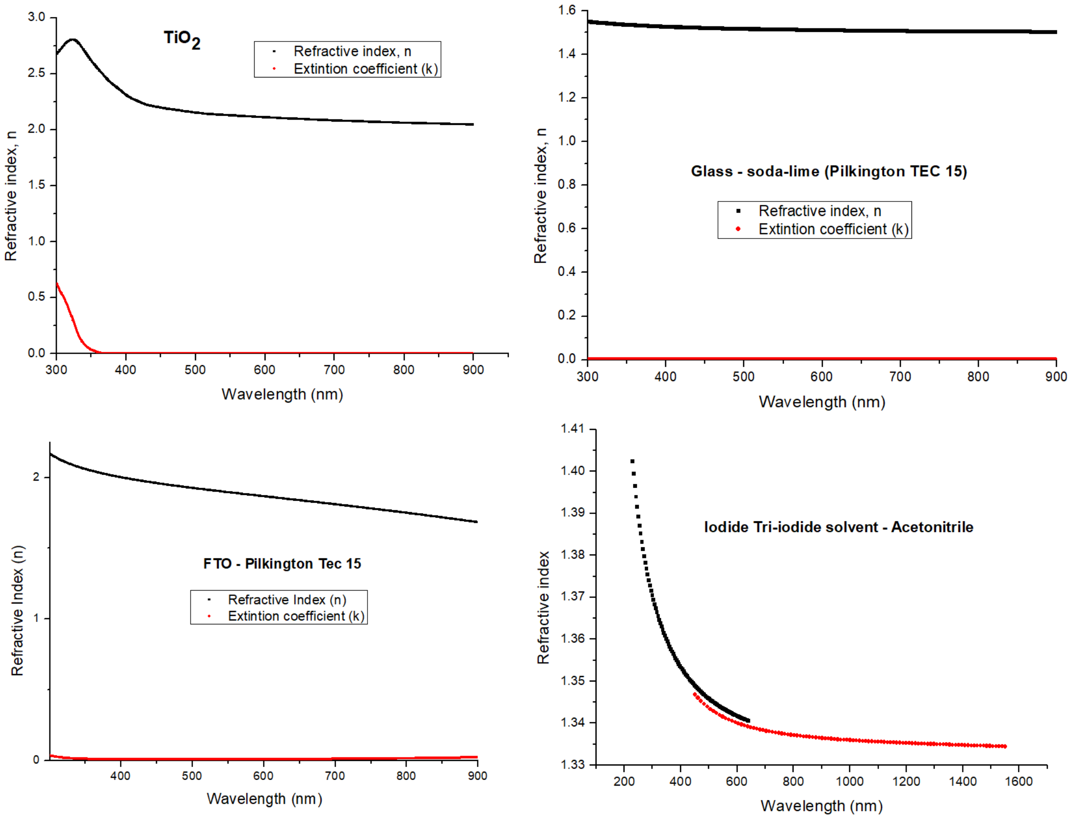

Figure A.2: Materials data for Ray-trace simulations for FTO, $TiO_2$ and Tec15 glass [175] and Electrolyte [176, 177].

## A.2 AM1.5 solar spectrum data used in ray-trace simulations

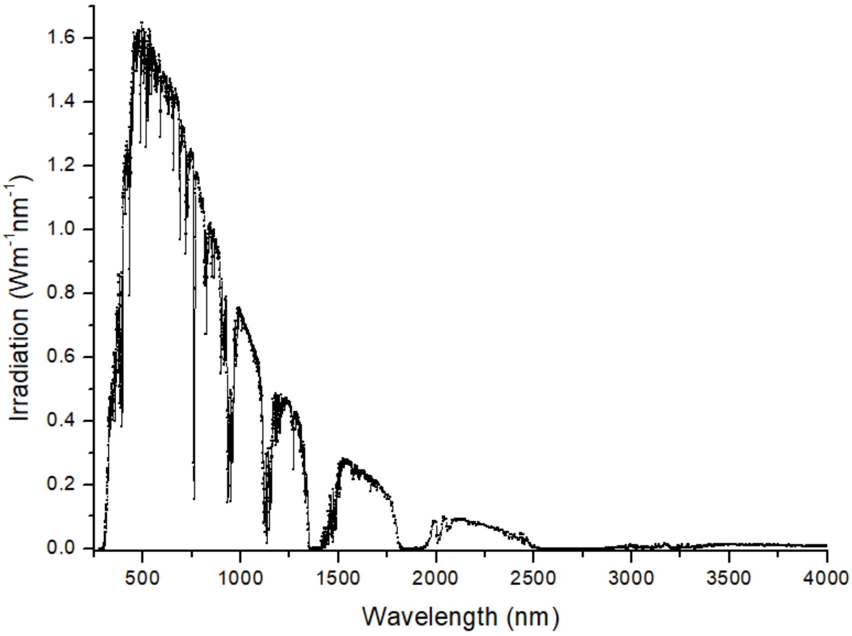

Figure A.3: AM 1.5 Solar Spectrum data [173].

# Bibliography

[1] M. Z. Jacobson. *Energy Environ. Sci,*, 2:148–173, 2008.

[2] J. M. Pearce. *Futures*, 34(7):663–674, 2002.

[3] T. Saga. *NPG Asia Mater.*, 2:96–102, 2010.

[4] N. K. Elumalai, A. Mahmud, D. Wang, and A. Uddin. *energies*, 9:961, 2016.

[5] M. Grätzel. *J. Photochem. Photobio. C. Photochem. Rev.*, 47:145 – 153, 2003.

[6] U.S. Energy Information Administration. *International Energy Outlook 2016*, 2016.

[7] Spiegel Online. *http://www.spiegel.de/international/spiegel/grossbild-429968-685811.html.*

[8] United Nations. *World Energy Assessment Report*, http://www.undp.org/content/dam/aplaws/publication/, 2000.

[9] S. Shockley and H. J. Queisser. *J. Appl. Phys.*, 32:3, 1961.

[10] European Commission. *PV Satus Report*, 2016.

[11] F. et al. Dimroth. *Prog. Photovolt: Res. Appl.*, 22:277–282, 2014.

[12] K. L. Chropra, P. D. Paulson, and V. Dutta. *Prog. Photovolt. Res. Appl.*, 12:69–92, 2004.

[13] National Renewable Energy Laboratory. *Best Research-Cell Efficiency*, 2016.

[14] Renewable Energy Policy Network. *Global Status Report*, 2016.

[15] B. O'Regan and M. Gräzel. *Nature*, 353, 1991.

[16] A. Hagfeldt, G. Boschloo, S. Licheng, K. Kloo, and H. Petterson. *Chem. Rev.*, 110:6569–6663, 2010.

[17] Nick84. *http://commons.wikimedia.org/wiki/File/Solarspectrumita.svg*, 2009.

[18] M. Ye, X. Wen, M. Wang, A. Locozzia, N. Zhang, C. Lin, and Z. Lin. *Materialstoday*, 19(3):155–162, 2015.

[19] S. Shalini, R. Balasundaraprabhu, S. T. Kumar, N. Prabavathy, S. Senthilarasu, and S. Parsanna. *Int. J. Energy Res.*, 40:1303–1320, 2016.

[20] S. Ito, T. N. Murakami, P. Comte, P. Liska, C. Gräzel, Nazeeruddin M. K., and M. Gräzel. *Thin Solid Films*, 516:4613–4618, 2008.

[21] F. D. Angelis, S. Fantacci, E. Mosconi, M. K. Nazeeryddin, and M. Grätzel. *J. Phys. Chem. C.*, 115:8825–8831, 2011.

[22] S. Shalini, R. Balasundaraprabhu, T. S. Kumar, N. Prabavathy, Senthilarasu S., and S. Prasanna. *Int. J. Energy Res.*, 40:1303–1320, 2016.

[23] M. Grätzel. *Phil. Trans. R. Soc.*, 365:993, 2007.

[24] A. Jena, S. P. Mohanty, P. Kumar, J. Naduvath, and G. Vivekanand. *Trans. Ind. Ceram. Soc.*, 71(1):1–16, 2012.

[25] V. Baglio, M. Girolamo, V. Antonucci, and A. S. Arico. *Int. J. Electrochem. Sci.*, 6:3375–3384, 2011.

[26] S. Sheehan, P. K. Surolia, O. Byrne, S. Garner, P. Cimo, X. Li, D. P. Dowling, and K. R. Thampi. *Sol. Energ. Mater. Sol. Cells*, 132:237–244, 2015.

[27] S. Yoon, S. Tak, J. Kim, J. Kim, Y. Jun, K. Kang, and J. Park. *Build. Environ.*, 46(10):1899–1904, 2011.

[28] T. Yu, J. Guan, X. Yu, J. Zhang, J. Lui, and Z. Zou. *Int. J. Electrochem. Sci.*, 7:1496–1511, 2012.

[29] R. C. Alkire, A. D. Kolb, J. Lipkowski, and P. N. Ross. *Photoelectrochemical Materials and Energy Conversion Processes.* Wiley, 2010.

[30] J. Wu, Z. Lan, S. Hao, P. Li, J. Lin, M. Huang, L. Fang, and Y. Huang. *Pure Appl. Chem.*, 80(11):2241–2258, 2008.

[31] S. Radhakrishnan, L. V. Munukulta, A. Htun, and A. M. Kannan. *Mater. Res. Soc. Symp. Proc.*, 1322:119–125, 2011.

[32] I. Lee, S. Hwang, and H. Kim. *Sol. Energ. Mater. Sol. Cells*, 95(1):315–317, 2011.

[33] D. Joly, L. Pelleja, S. Narbey, F. Oswlad, J. Chiron, J. N. Clifford, E. Palomares, and R. Demadrill. *Scientific Reports*, 4:4033, 2014.

[34] L. Giribabu and R. V. Kanaparthi. *Current Science*, 104:7, 2013.

[35] S. Gy un, P. D. Lund, and A. Hinsch. *Energ. Environ. Sci.*, 8:3495, 2015.

[36] A. Yella, H. W. Lee, H. N. Tsao, C. Yi, A. K. Chandiran, M. K. Nazeeruddin, E. W. G. Diau, C. Y. Yeh, S. M. Zakeeruddin, and M. Grätzel. *Science*, 334:629–634, 2011.

[37] M. A. Green. *Prog. Photovolt.*, 17:183–189, 2009.

[38] L. Turyanska, O. Makarovsky, U. Elfurawi, A. Patané, M. W. Fay, J. W. Bowers, and M. H. Upadhyaya. *Phys. Status Solidi A*, 208(10):2450–2453, 2011.

[39] C. Cheng, S. K. Karuturi, L. Liu, L.and Jinping, H. Li, L. T. Su, A. L. Y. Tok, and H. J. Fan. *Small*, 8(1):37–42, 2012.

[40] Q. Shen, J. Kobayashi, L. J. Diguna, and T. Toyoda. *J. Appl. Phys.*, 103:084304, 2008.

[41] Y. Tachibana, K. Umekita, Y. Otsuka, and S. Kuwabata. *J. Phys. D*, 41:102002, 2008.

[42] S. Rühle, M. Shalom, and A. Zaban. *J. Phys. D*, 41:102002, 2008.

[43] A. Kokima, K. Teshima, Y. Shirai, and T. Miysaska. *J. Am. Chem. Soc.*, 131(17):6050–6051, 2009.

[44] S. M. Matsui, K. Domanski, J. P. Correna-Baena, M. K. Nazeeruddin, S. M. Zakeeruddin, W. Tress, A. Abate, A. Hagfeldt, and M. Grätzel. *Energ. Environ. Sci.*, 9:1989–1997, 2016.

[45] D. Wang, M. Wright, N. K. Elumalai, and A. Uddin. *Sol. Energ. Mater. Sol. Cells*, 147:255–275, 2016.

[46] M. Cai, Y. Wu, H. Chem, X. Yang, Y. Qiang, and L. Han. *Adv. Sci.*, 4:1600269, 2016.

[47] A. Babayigit, A. Ethirajan, M. Muller, and B. Conings. *Nature Mater.*, 15:247–251, 2016.

[48] G. D. Scholes. *Chem. Rev.*, 117(2):247–248, 2017.

[49] B. Hua, B. Wang, P. W. Leu, and Z. Fan. *Nano Energy*, 2013.

[50] A. Mavrokefal, S. E. Han, S. Yeric, M. S. Branham, and G. Chen. *Nano Lett.*, 12(6):2792–2796, 2012.

[51] G. Otnes and Borgström. *nanotoday*, 12:31–45, 2017.

[52] Y. Shi, X. Wang, W. Liu, T. Yang, and F. Yang. *J. Optics*, 16(7), 2014.

[53] S. F. Leung, M. Yu, Q. Lin, K. L. Kwon, K. L. Ching, K. Gu, K. Yu, and Z. Fan. *Nano Lett.*, 12:3682–3689, 2012.

[54] K. V. Baryshinkova, M. I. Petrov, V. E. Babicheva, and P. A. Belov. *Scientific Reports*, 6:22136, 2017.

[55] J. Escarté, K. Söderstrom, M. Despeisse, S. Nicolay, C. Battagila, G. Bugnon, L. Ding, F. Meillaud, F-j. Huag, and C. Ballid. *Sol. Energ. Mater. Sol. Cells*, 98:185–190, 2012.

[56] B. Swatowska, T. Stapinski, K. Brabczyk, and P. Panek. *Optica Applicata*, 41(2), 2011.

[57] B. Rech and H. Wagner. *Appl. Phys. A*, 89(2):155–169, 1999.

[58] K. Bittkau, W. Böttler, M. Ermes, V. Smirnov, and F. Finger. *Appl. Phys.*, 111(8), 2012.

[59] H. Park, S. M. Ifiquar, A. H. T. Le, S. Ahn, J. Kang, Y. Kim, and J. Yi. *Trans. Electr. Electron. Mater*, 17(5):275–279, 2016.

[60] S. Rühle, S. Greenwald, E. Kore, and A. Zaban. *Optics Express*, 16(26):21801, 2008.

[61] D. B. Williams and C. B. Carter. *Introduction to Light Trapping in Solar Cell and Photo-detector Devices*. Spinger, (2014).

[62] Z. Hameiri. *Prog. Photovolt.*, 25(3):264–267, 2012.

[63] L. Hu and G. Chen. *Nano Lett.*, 7:3249–3252, 2007.

[64] E. Garnett and Y. Peidong. *Nano Lett.*, 10:1082–1087, 2010.

[65] L. Cao, P. Fan, A. P. Vasdev, J. S. White, Z. Yu, W. Cai, J. A. Schuller, S. Fan, and M. L. Brongersma. *Nano Lett.*, 10:439–445, 2010.

[66] R. Elbersen, W. Vijselaar, R. M. Tiggelaar, H. Gardeniers, and J. Huskens. *Adv. Mater.*, 27(43):6781–6796, 2015.

[67] J. Li, H. Yu, S. M. Wong, G. Zhangm, X. Sun, P. G. Q. Lo, and D. L. Kwong. *Appl. Phys. Lett.*, 95(03302102), 2009.

[68] Z. Y. Fan, H. Razavi, J. W. Do, A. Moriwaki, O. Ergen, Y. L. Chueh, P. W. Leu, J. C. Jo, T. Takahashi, L. A. Reichertz, S. Neale, K. Yu, J. W. Wu, M. an Ager, and A. Javey. *Nat. Mater.*, 85:648, 2009.

[69] A. Y. Fan, R. Kapadia, P. W. Leu, X. B. Zhang, Y. L. Chueh, K. Takei, A. Jamshidi, A. A. Rathore, and D. J. Ruebusch. *Nano Lett.*, 10:3823–3827, 2010.

[70] H. P. Yoon, Y. A. Yuwen, C. E. Kendrick, G. D. Barber, N. J. Podraza, J. M. Redwing, T. E. Mallouk, C. R. Wronski, and T. S. Mayer. *Appl. Phys. Lett.*, 965(213503), 2010.

[71] Z. Fen, D. J. Ruebusch, A. A. Rathore, R. Kapadia, O. Ergen, P. W. Leu, and A. Javey. *Nano Res.*, 2:829–843, 2009.

[72] Y. Lu and A. Lal. *Nano lett.*, 10:4651–4656, 2010.

[73] S. Jeong, M. T. McDowell, and Y. Cui. *ACS Nano*, 5:5800–5807, 2011.

[74] S. Jeong, E. C. Garnett, S. Wang, Z. Yu, S. Fan, M. L. Brogersma, M. D. McGehee, and Y. Cui. *Nano Lett.*, 12:2971–2976, 2012.

[75] D. Liang, Y. Huo, K. X. Kang, A. Gu, M. Tan, Z. Yu, S. Li, J. Jia, and X. Bao. *Adv. Energy Matter.*, 22:1254–1260, 2012.

[76] I. Ding, J. Zhu, W Cai, S. Moon, N. Cai, P. Wang, S. M. Zakeeruddin, M. Gräzel, M. L. Brongersma, and Y. Cui. *Adv. Energy Matter.*, 1:52–57, 2011.

[77] J. Yao, Y. abd Yao, Narasimhan V. K., Z. Ruan, C. Xie, S. H. Fan, and Y. Cui. *Nat. Commun.*, 3:664–760, 2012.

[78] S. Pillai, Catchpole K., T. Trupke, and M. Green. *J. Appl. Phys.*, 101(093105), 2007.

[79] S. E. Han and G. Chen. *Nano Lett.*, 10:1012–1015, 2010.

[80] Z. P. Zhang, S. Ito, B. O'Regan, S. M. Zakeeruddin, P. Pechy, R. Humphry-Baker, P. Comte, T. Koyanagi, Mizuno T., Nazeeruddin M. K., and M. Gräzel. *Phys. Chem*, 221:319, 2007.

[81] M-J. Jeng, Y-L. Wung, L-B. Chang, and L. Chow. *Int. J. Photoenergy*, 2013:563897, 2013.

[82] X. Tan, P. Qian, D. Zhang, X. Cai, and S. Tan. *CrystEngComm*, 16:1020, 2013.

[83] W. L. Vos and J. E. G. J. Wijnhoven. *Science*, 281:802 – 804, 1998.

[84] L. Qi and D. P. Birnie. *Mater. Lett.*, 61:2191 – 2194, 2007.

[85] S. G. Park, T. Y. Jeon, and S. Yang. *Langmuir*, 29:9620 – 9625, 2013.

[86] F. Ramiro-Manzano, P. Atienzar, I. Rodrisuez, F. Mesegure, H. Garcia, and A. Corma. *Chemm. Commun.*, 244:242 – 244, 2006.

[87] C. Y. Cho and J. K. Moon. *Materials Views*, 23:2971–2975, 2011.

[88] A. J. Labbelle, S. M. Thon, S. Masala, M. M. Adachi, H. Dong, F. Maryam, A. Ip, A. Fratalocchi, and E. H. Sargent. *Nano Lett.*, 15(2):1101–1108, 2015.

[89] J. B. Baxter and E. S. Aydil. *Appl. Phys. Lett.*, 86(5):053114, 2005.

[90] W-Y. Rho, H. Jeon, H-S. Kim, W-J. Chung, J. S. Suh, and B-H. Jun. *J. Nanomater.*, 2015:247689, 2015.

[91] M. Adachi, Y. Murata, J. Takao, J. Jui, M. Sakamoto, and F. Wang. *J. Am. Chem. Soc.*, 126:14943–14949, 2004.

[92] H. Chriadella. *Appl. Opt.*, 30:3492, 1991.

[93] B. D. Heilman and I. N. Miaoulis. *Appl. Opt.*, 21:33–40, 2009.

[94] S. Yamakana, R. Yano, H. Usami, N. Hayashida, M. Ohuchi, H. Takeda, and K. Yoshino. *J. Appl. Phys.*, 103(074701), 2008.

[95] J. Toster, K. S. Iyer, W. Xiang, F. Rosei, L. Spiccia, and C. L. Raston. *Nanoscale*, 5:873–877, 2012.

[96] H. Tabata, K. Kumazawa, K. Funakawa, J. Takimoto, and M. Akimoto. *Optical Review*, 3(2):139–145, 1996.

[97] D. W. Koon and A. B. Crawford. *Appl. Opt.*, 39(2496), 2000.

[98] Z. Han, S. Niu, C. Shang, Z. Lui, and L. Ren. *Nanoscale*, 4:2879–2883, 2012.

[99] Z. Han, S. Niu, M. Yang, J. Zhang, W. Yin, and L. Ren. *Nanoscale*, 5:8500–8506, 2013.

[100] W. Zhang, D. Zhang, T. Fan, J. Gu, J. Din, H. Wang, Q. Guo, and H. Ogawa. *Chem. Mater.*, 21:33–40, 2009.

[101] C. Bowler, A. E. Allen, J. H. Badger, and C. Grimwood. *Nature*, 456:239–244, 2008.

[102] M. W. Anderson, S. M. Holmes, N. Hanif, and C. S. Cundy. *Angew. Chem., Int. Ed.*, 39:2707–2710, 2000.

[103] C. Jeffryes, T. Gutu, J. Jiao, and G. L. Rorrer. *Nano*, 2:2103–2112, 2008.

[104] D. De Stefano and L. De Stefano. *J. Nanosci. Nanotech.*, 5:15–24, 2005.

[105] C. Jefferyes, J. Campbell, H. Li, J. Jiao, and G. L. Rorrer. *Energy Environ. Sci.*, 4:3930, 2012.

[106] D. De Stefano, P. Maddalena, L. Moretti, I. Rea, I. Rendina, De Tommasi, V. Mocella, and L. De Stefano. *Superlattice Mictostr.*, 46:84–89, 2007.

[107] C. Jeffryes, T. Gutu, J. Jio, and G. L. Rorrer. *J. Mater. Res.*, 23:3255–3262, 2008.

[108] Peter L. M. *J. Phys. Chem.*, 111:6601–6612, 2007.

[109] G. Khelashvili, S. Behrens, C. Weidenthaler, C. Vetter, A. Hinsch, K. Skupien, E. Dinjus, and H. Bonnemann. *Thin Solid Films*, 511:324, 2006.

[110] I. Montanari, J. Nelson, and J. R. Durrant. *J. Phys. Chem. B*, 106:12203, 2002.

[111] J. Nelson and R. E. Chandler. *Coord. Chem. Rev.*, 248:1181, 2004.

[112] E. L. Efurumibe, A. D. Asiegbu, and M. U. Onuu. *Asian, J. Applied. Sci.*, 5:33–34, 2012.

[113] A. Dabirian and N. Taghavinia. *RSC Adv.*, 3:25417–25422, 2013.

[114] F. E. Gálves, E. Kemppainen, H. Mígues, and J. Halme. *J. Phys. Chem. C.*, 116:11426–11433, 2012.

[115] S. Forster and S. John. *Energy Environ. Sci.*, 6:2972–2983, 2013.

[116] K. G. Ong, O. K. Varghese, G. K. Mor, K. Shankar, and C. A. Grimes. *Sol. Energy Mater. Sol. Cells*, 91:250–257, 2007.

[117] J. Halme, G. Boschloo, A. Hagfeldt, and P. Lund. *J. Phys. Chem. C.*, 112:5623–5637, 2008.

[118] F. Demesy, F. Zolla, A. Nicolet, M. Commandre, and C. Fossati. *Opt. Express*, 15:18089–18102, 2007.

[119] X. Liu, Y. Wu, X. Hou, and H. Liu. *buildings*, 7:88, 2017.

[120] F. Zhang, N. Zhang, Y. Zhang, S. Yan, S. Sun, J. Bao, and C. Gao. *Chin. Phys. B.*, 26:054201, 2017.

[121] D. Thorpe and S. R. Wenham. *Sol. Energ. Mater. Sol. Cells*, 48:295–301, 1997.

[122] H. Holst, M. Winter, M. R. Vogt, K. Bothe, M. Kontges, R. Brendl, and P. P. Altermatt. *Energy Procedia*, 38:86–93, 2013.

[123] Y. Takeda, H. Izuka, N. Yamada, and T. Ito. *Applied Optics, volume =.*

[124] T. Yagi, Y. Urakoka, and T. Fuyuki. *Solar Eng. Mater. Sol. Cells*, 90:2647–2656, 2006.

[125] S. Wenger, M. Schmid, G. Rothenberger, A. Gentsch, M. Grätzel, and J. O. Schumacher. *J. Phys. Chem. C*, 115:10218–10229, 2010.

[126] M. Kennedy, H. Ahmed, J. Doran, B. Norton, P. Bosch-Jimenez, M. Della Pirriera, E. Torralba-Calleja, D. G. Tauste, L. Aubouy, S. Daren, F. Solomon-Tsvetkov, S. Galindo, C. Voz, and J. Puigdollers. *Phys. Status Solidi A*, 1:2012, 2015.

[127] R. Graham and D. Yu. *Mod. Phys. Lett. B*, 27(25):133018, 2013.

[128] S. L. Howell, S. Padalkar, H. Yoon, Q. Li, D. D. Koleske, J. Wierer, G. T. Wang, and J. Lauhon. *Nano Lett.*, 13(11):5123–5128, 2013.

[129] J. R. Haynes and W. Schockley. *Phys. Rev.*, 75:691, 1949.

[130] J. Marek. *J. Appl. Phys.*, 55:318, 1984.

[131] K. Balasubramanian, Y. Fan, M. Burghard, K. Kern, M. Friedrich, U. Wannek, and A. Mew. *Appl. Phys. Lett.*, 84:2400–24002, 2004.

[132] J. E. Allen, E. R. Hemesath, and L. J. Lauhon. *Nano Lett.*, 9(5):1903–1909, 2009.

[133] D. B. Strasfield, D. A. Wagner, and M. G. Bawendi. *Nano lett.*, 12(2):569–575, 2012.

[134] H. Cao, G. Aivazian, Z. Fei, J. Ross, D. H. Cobden, and X. Xu. *Nature Phys.*, 12:236–239, 2016.

[135] C. Reuter, R. Frisenda, D. Y. Lin, T. S. Ko, D. Perez de Lara, and Castellano-Gomez A. *Small*, 10.1002/smtd.201700119, 2017.

[136] C. McNiell, H. Frohne, J. L. Holdsworth, E. F. John, B. V. King, and P. C. Dastoor. *Nano Lett.*, 4(2):291–223, 2004.

[137] W. Rouis, M. Haggui, S. Rekaya, L. Sfaxi, R. M'ghaieth, H. Maaref, and Fumagalli. *Sol. Energ. Mat. Sol.*, 144:324–330, 2016.

[138] R. Xiao, Y. Hou, Y. Fu, X. Peng, Q. Wang, E. Gonzalez, S. Jin, and D. Yu. *Nano Lett.*, 16:7770–7717, 2016.

[139] M. J. Scott, M. Woodhouse, B. A. Parkinson, and C. Micheal Elliot. *J. Electrochem. Soc.*, 155(3):290–293, 2008.

[140] J. K. Park, J-C. Kang, S. Y. Kim, B. H. Son, J-Y. Park, S. Lee, and A. H. Ahn. *J. Phys. Chem. Lett.*, 3:3632–3638, 2012.

[141] M. Mitsui, Y. Kawano, K. Mori, and N. Wakabayashi. *Langmuir*, 31:7158–7165, 2015.

[142] T. W. Jones, K. Feron, K. F. Anderson, B. C. Duck, and G. J. Wilson. *J. Appl. Phys.*, 116:043104, 2014.

[143] H. W. Tan, T. Tran, and C. K. Chua. *Virtual Phys. Prototyp.*, 11(4), 2015.

[144] K. Cook, J. Canning, S. Leon-Saval, Z. Reid, A. Hossain, J. Comatti, Y. Luo, and G. Peng. *Optics Letters*, 40(17):3966–3969, 2015.

[145] S. Maruo and J. T. Fourkas. *Laser Photon. Rev.*, 2(1-2):100–111, 2008.

[146] P. T. C. So. *Annu. Rev. Biomed. Eng.*, 2:399, 2000.

[147] S. Katawa, H. B. Sun, T. Tianaka, and Takanda S. *Nature*, 412:612, 2001.

[148] M. Göppert-Mayer. *Ann. Phys.*, 9:273, 1931.

[149] W. Karser and C. G. B. Garret. *Phys. Rev. Lett.*, 4:229, 1961.

[150] W. Denk, J. H. Stickler, and W. W. Webb. *Science*, 247:73, 1990.

[151] K. S. Lee, R. H. Kim, D. Y. Yang, and S. U. Park. *Prog. Poly. Sci.*, 33:631–681, 2012.

[152] K. Sun, T. S. Wei, B. Y. Ahn, S. J. Dillon, and J. A. Lewis. *Adv. Mater.*, 25:4539–4543, 2013.

[153] X-Z. Don, Q. Ya, X-Z. Sheng, Z-Y. Li, Z-S. Zhao, and X-G. Duan. *Appl. Phys. Lett.*, 92:231103, 2008.

[154] K. K. Seet, V. Mizeikis, S. Matuso, S. Juodkazis, and H. Misawa. *Adv. Mater.*, 17:5, 2005.

[155] M. Hermatschweiler, A. Ledermann, G. A. Ozin, M. Wegner, and G. V. Freyman. *Adv. Func. Mater.*, 17:2273–2277, 2007.

[156] J. K. Gansel, M. Thiel, M. S. Rill, M. Decker, K. Bade, V. Saile, G. V. Freymann, S. Linden, and M. Wegener. *Science*, 325:1513–1515, 2009.

[157] S. Klien, A. Barsella, H. Leblond, H. Bulou, A. Fort, C. Andraud, G. Lemercier, J. C. Mulatier, and K. Dorkenoo. *Appl. Phys. Lett.*, 9:211118., 2005.

[158] R. Guo, S. Xio, X. Zhai, J. Li, A. Xia, and W. Huang. *Opt. Express.*, 14:810, 2006.

[159] Y. Lui and X. Zhang. *Chem. Rev. Soc. Rev.*, 40:2494–2507, 2011.

[160] J. P. Turpin, J. A. Bossard, K. L. Morgan, D. H. Wener, and P. L. Werner. *int. J. Antennas Propag.*, page 429837, 2014.

[161] A. Radke, T. Gissibl, T. T. Klotsbücher, P. V. Braun, and H. Giessen. *Adv. Mater.*, 23:3018–3021, 2011.

[162] X. Xion, Z-H. Xue, C. Meng, S-C. Jiang, Y-H. Hu, R-W. Peng, and M. Wang. *Phys. Rev. B.*, 88:115105, 2013.

[163] M. Suzuki, T. Sawa, Y. Terada, T. Takahashi, and S. Aoyagi. *Transducers 2015 Proceedings*, 15, 2015.

[164] B. Florijn, C. Coulais, and M. van Hecke. *Phys. Rev. Lett.*, 113:175503, 2014.

[165] Bückmann T., N. Stegner, M. Kadic, C. Kaschke, A. Frölich, C. Eberl, M. Thiel, and M. Wegener. *Adv. Mater.*, 22(24):2710–2714, 2012.

[166] D. Jang, L. R. Meza, F. Greer, and J. R. Greer. *Nature Mater.*, 12:893–898, 2013.

[167] G. Nelson, R. A. Kirian, U. Weierstall, N. A. Zatsepin, T. Fargó, T. Baubach, F. Wilde, F. B. P. Nielser, B. Zimmer, I. Ishigami, M. Mikita, S. Bajt, S-R. Yeh, D. L . Rousseau, J. C. H. Chapman, H. N. Spence, and M. Heymann. *Opt. Express*, 24:11515–11530, 2016.

[168] S. Tottori, L. Zhang, F. Qiu, K. K. Krawczyk, and Franco-Obregón. *Adv. Mater.*, 24(6):811–816, 2012.

[169] H. Lee, D. Hwang, S. M. Jo, D. Kim, and D. Y. Kim. *Appl. Mater. Interfaces*, 4:3308–3315, 2012.

[170] F. Klien, T. Striebel, J. Fischer, Z. Jiang, C. M. Franz, G. von Freymann, M. Wegener, and Bastmeyer. *Adv. Mater.*, 22(8):868–871, 2010.

[171] M. Röhrig, M. Thiel, M. Worgull, and Hölscher. *Small*, 10.1002, 2012.

[172] W. Bathlott, T. Schimmel, S. Wiersch, K. Koch, M. Brede, M. Bacrczweski, S. Walheim, A. Wies, A. Kaltenmaier, A. Leder, and H. F. Bohn. *Adv. Mater.*, 22(21):2325–2328, 2010.

[173] American Society for Testing and Materials. *http://rredc.nrel.gov/solar/spectra/am1.5/*, 2000.

[174] D. Dabirian and N. Taghavina. *Appl. Mater. Interfaces*, 7:14926–14932, 2015.

[175] J. M. Ball, S. D. Stranks, M. T. Höantner, S. Hüttner, W. Zhang, E. J. W. Crossland, I. Ramirez, M. Riede, M. B. Johnston, and H. J. Friend, F. H. an Snaith. *Energy. Environ. Sci.*, 8:602, 2015.

[176] I. Z. Kozma, P. Krok, and E. Riedle. *J. Opt. Soc. Am. B.*, 22:1479–1485, 2005.

[177] M. Moutzoris, S. C. Paramicheal, S. C. Betsis, I. Stavrakas, G. Hloupius, and D. Triantis. *Appl. Phys. B.*, 166:617–622, 2013.

[178] S. Ito, K. Takahashi, S-I. Masayuki S. Yusa, and T. Shigetomi. *Inter. J. Photoeng.*, 2013:501868, 2013.

[179] K. Tsuji, J. Injuk, and R. V. Grieken. *X-Ray Spectroscopy: Recent Technological Advances.* Wiley, 2004.

[180] Nanoscribe. *http://www.nanoscribe.de/en/products/photonic-professional-gt/.*

[181] Carl Zeiss. *https://www.zeiss.com/microscopy/int/products/light-microscopes/axio-observer-for-biology/definite-focus.html*, 2015.

[182] Nanoscribe. *http://www.nanoscribe.de/en/products/ip-photoresists/.*

[183] W. Jian, H. Liu, L. Yin, Y. Shi, and C. Bangdao. *J. Phys. Chem. C.*, 120:9678–9684, 2016.

[184] W. Jiang, H. Liu, L. Yin, Y. Shi, and B. Chen. *J. Phys. Chem. C.*, 120:9678–9684, 2016.

[185] Nanoscribe. *http://www.nanoscribe.de/en/products/software/.*

[186] J. Zhange, K. L. Tan, G. D. Hong, L. J. Yang, and H. Q. Gong. *J. Micromech. Microeng.*, 11(1):20, 2001.

[187] B. C. O'Regan, J. R. Durrant, P. M. Sommeling, and N. J. Bakker. *J. Phys. Chem. C.*, 111(37):14001–14010, 2007.

[188] Dyesol. *http://www.dyesol.com/products/dsc-materials/pastes/18nrt-transparent-titania-paste.html.*

[189] Sigma-Aldridge. *Ruthenium-based dyes for Dye-sensitized Solar Cells*, http://www.sigmaaldrich.com/technical-documents/articles/materials-science/organic-electronics/dye-solar-cells.html, 2017.

[190] C. Mange, M. Urien, and T. Paupoete. *RSC Advances*, 3(18):6315–6318, 2013.

[191] X. Mao, R. Zhou, S. Zhang, L. Ding, L. Wan, S. Qin, Z. Chen, J. Xu, and S. Miao. *Scientific Reports*, 6:19390, 2016.

[192] S. Wooh, H. Yoon, J-H. Jung, Y-G. Lee, J. H. Koh, B. Lee, Y. S. Kang, and K. Char. *Adv. Mater.*, 25:3111–3116, 2013.

[193] M. Abdelhamid. *J. Photovolt.*, 4(1):514–254, 2014.

[194] I. Kajari-Schöer and M. Köntges. *Energy Procedia*, 27:658–663, 2012.

[195] M Köntges, I. Kunze, X. Breitenmoser, and Bjorenklett .B. *Sol. Eng. Mater. Sol. Cells*, 95:1131–1137, 2011.

[196] J. I. Mölken, U. A. Yusufoglŭ, A. Saflei, H. Windgassen, R. Khandelwal, Pletzer T. M., and H. Kurz. *Energy Procedia*, 27:167–172, 2012.

[197] X. Wang, M. Xi, F. Zheng, B. Din, H. Fong, and Z. Zhu. *Nano Energy*, 12:794–800, 2015.

[198] M. S. Liang, Y. K. Fong, C. C. Khaw, C. C. Lui, and S. P. Chin. *J. Energ. Power Eng.*, 2:18–24, 2014.

[199] X. L. He, G. J. Yang, C. J. Mi, and S. Q. Fan. *J. Power Sources*, 280:182–189, 2015.

[200] W. M. Jin, C. Y. Cho, J. H. Kang, J. H. Park, and J. C. Moon. *ACS Appl. Mater. Interfaces*, 2(11):2970–2973, 2016.